Structural and Magnetic Properties of the Superconductors Mo_3Sb_7, Mo_3Al_2C and $K_xFe_{2-y}Se_2$ Under High Pressure

Terence Robert Giles

Royal Holloway and Bedford College
University of London

A dissertation submitted to the University of London for
the degree of Doctor of Philosophy

April 3, 2016

Declaration

This dissertation is the result of work carried out at the Department of Physics, Royal Holloway University of London, between September 2011 and April 2015. This dissertation is my own work and conatins nothing which is the outcome of work in collaboration with others, except as specified in the text and Acknowledgements. No part of this dissertation has been submitted for a degree, diploma or other qualification at this or any other university. The total length of this dissertation does not exceed one hundred thousand words.

Terence Robert Giles
April 2015

Abstract

This thesis is based on high pressure structural and superconducting phase diagrams of the three compounds Mo_3Sb_7, Mo_3Al_2C and $K_xFe_{2-y}Se_2$, which have all been reported to exhibit unconventional superconductivity. A new technique for measuring magnetic susceptibility at high pressure in a Bridgman type pressure cell has been developed which places counterwound detection and compensation coils within the high pressure sample space, which allows for improved signal-to-noise ratios compared to other methods. X-ray powder diffraction using diamond anvil cells was utilised to study the structural evolution of these compounds with increasing pressure.

The pressure-temperature phase diagram of Mo_3Sb_7 has been extended to higher pressures than reported previously and shows that the superconducting transition temperature increases. Structural measurements reveal that the cubic structure remains stable up to 13.6 GPa. Similar measurements on Mo_3Al_2C show a slight pressure dependence of T_c. A jump in the unit cell volume of Mo_3Al_2C indicates a structural transition occuring near 13.8 GPa. Finally high pressure X-ray powder diffraction measurements confirm a structural transition in both superconducting and insulating samples of $K_{0.8}Fe_{2-y}Se_2$ ($y = 0, 0.4$). Low temperature structural measurements have been carried out to build up the pressure-temperature phase diagram of superconducting $K_{0.8}Fe_2Se_2$. The strucutral transition occurs at a pressure between 13.2 and 15 GPa at low temperatures and appears to be strongly linked to the emergence of a second superconducting phase.

Acknowledgments

I would firstly like to thank my supervisors Dr. Philipp Niklowitz and Dr. Heribert Wilhelm at Diamond Light Source for giving me the opportunity to conduct my experiments and for their continuing supervision throughout the project. Secondly I must thank Chris Harrison for all his knowledge and guidance in the first few months and James for his help in the final year. Thanks must go to Dominik Daisenberger for all his advice and tireless efforts to make my diamond anvil cell experiments a success. Thanks also to Annette Kleppe and Allan Ross for their assistance at Diamond Light Source.

Next I must thank Dave for being an excellent housemate for two years and all my fellow PhD students Jim, Kris, Connor, George, Frankie, Dave, Rich, Rob, Manoj, Will, Frank, Ian, Toby, Tom, Pardis, Russel, Claire, Emily, Ben, David, Katie and Harriet. Thanks to Dan, Aya, Lev and Uthay. I would also like to thank Andy, Ian and Michele for their help around the department and also Francis and Harpal for the continuous supply of helium. Finally I would like to thank my parents and sister Fiona for all their support throughout my education, and my partner Emily for all her love and support and for always being there for me.

Contents

List of Figures

List of Tables

Chapter 1

Introduction

1.1 History of Superconductivity

The phenomenon of superconductivity, in which a substance exhibits exactly zero electrical resistance and the complete expulsion of a magnetic field, was first observed by Kamerlingh Onnes in 1911 in Hg below 4.1K [1]. Following on from here many other elements were found to also become superconducting at low temperatures of a few Kelvin. Superconductivity is based around the formation of bound pairs of electrons known as Cooper pairs which condense into a single ground state. The formation of Cooper pairs was described as a phonon-mediated pairing mechanism by Bardeen, Cooper and Schrieffer in 1957 and is known as the BCS theory [2]. During the following years many compounds were found to exhibit superconducitivity with a highest superconducting transition temperature of 23K found for Nb_3Ge in 1973 [3].

In 1986 a new class of superconductor known as the cuprates, based around layers of CuO, appeared with the discovery of superconductivity in $La_{2-x}Ba_xCuO_4$ at 38K [4]. Within a very short time many other cuprate superconductors had been discovered including the compound $YBa_2Cu_3O_7$ [5] which had the first transition temperature above 77K. About 20 years later came the first report of an Fe-based superconducting compound when LaOFeP was found to exhibit superconductivity at a temperature of about

$\sim$ 4K [6]. In 2008 focus shifted heavily towards this new class of Fe-based superconductor when superconductivity was seen in $LaFeAs(O_{1-x}F_x)$ at the high temperature of $\sim$ 26K [7]. This led to the synthesis of many more Fe-based superconducting compounds and transition temperatures above 50K were reported, making them the second highest only to the cuprates. These compounds are similar to the cuprates in that they are based around Fe layers. The phase diagram of the Fe-based superconductors, figure 1.1, reveals the appearance of multiple superconducting phases with doping, along with the possible coexistance of the superconductivity with an antiferromagnetic phase.

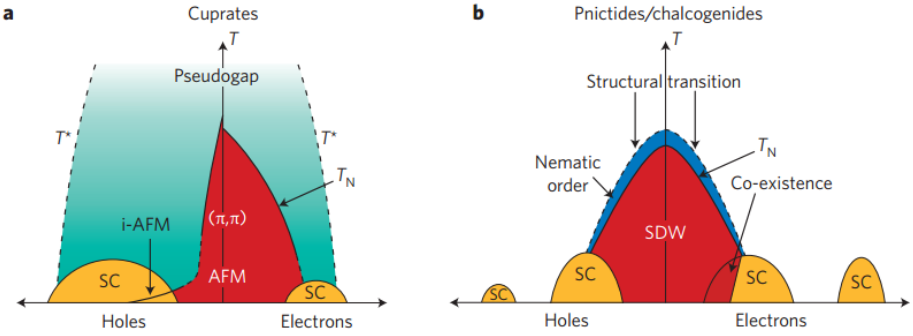

Figure 1.1: Schematic phase diagram of (a) the cuprates and (b) the Fe-based superconductors upon hole and electron doping. At relatively small dopings superconductivity and antiferromagnetism coexist. The superconductivity can also be initiated by pressure as well as doping [8]

Materials which exhibit superconductivity that can be described by the BCS theory, i.e. those in which the Cooper pairing is mediated by phonon interactions, are known as conventional superconductors. A material in which the Cooper pairing is mediated by other pairing mechanisms, such as spin fluctuations, are known unconventional superconductors.

1.2 Quantum Phase Transitions and Superconducitvity

A classical phase transition occurs between two different states at a finite temperature. If the transition is continuous then it is called second order. A second order phase transition that occurs at zero temperature is called a quantum phase transition (QPT). The system is driven through the quantum phase transition via a non-thermal parameter, for example pressure, chemical doping or magnetic field. The point at which the quantum phase transition occurs at zero temperature is called a quantum critical point (QCP). As a system is tuned toward a QCP interesting novel phases can emerge which are generally centred above where the QCP would exist. One of the most common of these novel phases is the emergence of superconductivity. In the cuprates and the Fe-based materials, superconductivity is often found near the point where an antiferromagentic phase ends as can be seen in Figure 1.1, pointing to magnetism as the underlying mechanism for electron pairing in unconventional superconductivity.

1.3 Pressure as a Tuning Mechanism

The application of pressure provides a very powerful method of tuning, in a very controllable manner, the volume of a sample. Thus, high pressure can induce structural, electronic and other phase transitions. The use of pressure is a very clean method of tuning a material, compared to for example chemical substitution which can cause disorder and shifts in the Fermi level and magnetic field. The first high pressure studies on a superconductor were carried in 1925 by Sizoo and Onnes [9] and revealed that for Sn and In the superconducting transition temperature, T_c, decreases with pressure. Since then the application of high pressure has been extremely valuable in the search for superconductors with higher values of T_c, and may hopefully one day help to find materials in which T_c surpasses room temperature. High pressure experiments can contribute to the field of superconductivity in diverse ways. Firstly, if a large magnitude

of dT_c/dP is found in a material it can be a good indication of whether a higher value of T_c could be found in that material with appropriate chemical substitution or other means. Secondly, some superconducting compounds can only be synthesised through the simultaneous combination of high pressure and high temperature [10]. Thirdly, many materials become superconducting under the application of high pressure.

Many different techniques have been developed in order to investigate superconducting, structural and other magnetic and thermodynamic properties under high pressure. Although the use of high pressure gives a very useful tuning parameter, many of the techniques have very complicated setups leading to fairly low rates of success or the need for complex substraction of background signals. The development of simpler designs is of great importance for both the sucess rates of experiments and for higher measurment accuracy. A new, simplier technique for measuring the superconducting transition temperature of materials under high pressure that places both the pickup and compensation coils, on the same electrical circuit, in the high pressure sample space of the pressure cell has been developed and is described in this thesis.

1.4 Superconductors Studied in this Thesis

1.4.1 Mo_3Sb_7: A Superconductor with a Simple Phase diagram

The compound Mo_3Sb_7 is an interesting exmaple of a d-electron superconductor which possesses a fairly simply phase diagram with is uncommon. Figure 1.2 shows the enhancement of the superconducting transition temperature with increasing pressure. An antiferromagnetic phase appears at about 0.5 GPa at temperature T_{SDW} before being slowly suppressed with increasing pressure. By extending the phase diagram to higher pressures the role that the magnetism play in the superconductivity can be explored.

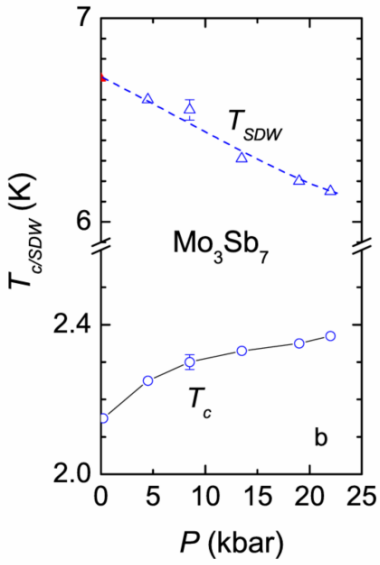

Figure 1.2: Pressure-dependence of the superconducting transition temperature, T_c, and antiferromagnetic transition, T_{SDW} of Mo_3Sb_7.

1.4.2 Mo_3Al_2C: A noncentrosysmmetric d-electron Superconductor

The compound Mo_3Al_2C is a d-electron superconductor with the interesting property of lacking a centre of inversion symmetry as can be seen in figure 1.3. It gives an opportunity to study the evolution of structural and electronic properties of a d-electron noncentrosymmetric superconductor with a relatively high T_c under high pressure.

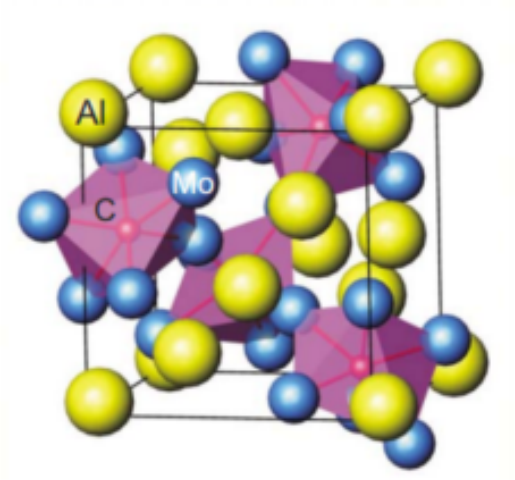

Figure 1.3: Unit cell ($P4_132$) of Mo_3Al_2C emphazising the non-centrosymmetry. Mo, Al and C atoms are indicated in blue, yellow and purple respectively [11].

1.4.3 $K_{0.8}Fe_2Se_2$: Re-emergent Superconductivity

$K_{0.8}Fe_2Se_2$ is an Fe based superconductor in which the superconductivity is suppressed with increasing pressure, see figure 6.18. A more intriguing feature of this material is that with further increase of pressure a second superconducting phase emerges with a higher superconducting transition temperature. By studying the structural properties of the system the interplay of a structural transition and the superconductivity can be established.

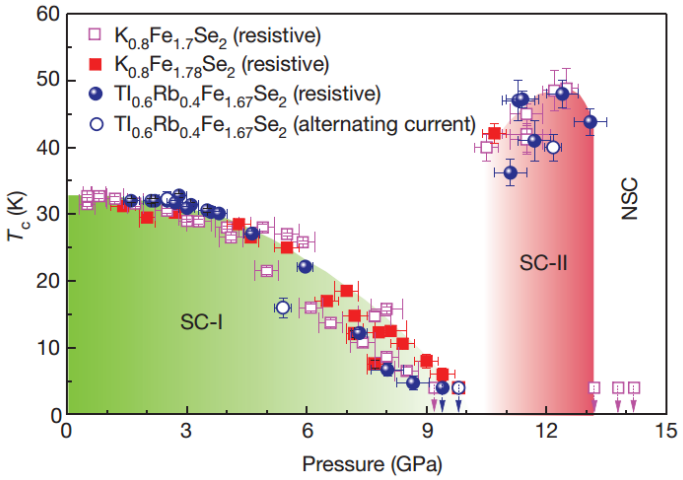

Figure 1.4: Pressure dependence of T_c for $K_{0.8}Fe_{1.7}Se_2$ and $K_{0.8}Fe_{1.78}Se_2$. All samples show suppression of T_c at a critical pressure before a second superconducting phase appears at higher pressures. [12].

1.5 Overview of this Thesis

In this thesis the three compounds Mo_3Sb_7, Mo_3Al_2C and $K_{0.8}Fe_2Se_2$ where studied under pressure. The phase diagram of Mo_3Sb_7 will be extended to higher pressure to explore the role of the superconductivity. Mo_3Al_2C under pressure gives an opportunity to study the phase diagram of d-electron noncentrosymmetric superconductor. By studying the structure of $K_{0.8}Fe_2Se_2$ at low temperatures the critical pressure of the structural transition can be found. In chapter 2 the physical concepts are discussed in more detail. Chapter 3 contains a summary of the different experimental methods used to obtain the results in this thesis including standard techniques as well as the

progess made on newly developed techniques for high pressure powder diffraction at low temperature and high pressure magnetic susceptibility measurements. High pressure x-ray powder diffraction and magnetic susceptibility measurements of Mo_3Sb_7 and Mo_3Al_2C are presented in chapter 4. The results of high pressure x-ray powder diffraction measurements of $K_{0.8}Fe_2Se_2$ are shown in chapter 5 along with the final phase digram showing the behaviour of the structural transition. Finally a short conclusion of all the work carried in this thesis is presented in chapter 6.

Chapter 2

Background Information

2.1 Pressure Response of a Solid

The compressibility of a compound can be defined through relationships between the volume and applied external pressure. These relationships are known as equations of state, and also define how properties change in response to compression. An equation of state is termed '*isothermal*' for the influence of pressure on volume at a fixed temperature. There are many types of equation of state and those used in this thesis are described in the following sections [13].

2.1.1 Murnaghan Type EoS

The simpliest equation of state providing the relationship between pressure and volume is to assume that the bulk modulus of a compound, K, is constant and therefore the volume decreases linearly with increasing pressure. The elastic properties of a solid however change on compression and so the simple linear assumption is not valid. The Murnaghan equation of state was first dervied [14] from the assumption that the bulk modulus, K, is a linear function of pressure given by

$$K = K_0 + PK_0' \tag{2.1}$$

where K_0 is the bulk modulus at zero pressure and K_0' is its pressure derivative, which results in a relationship between P and V given by

$$P(V) = \frac{K_0}{K_0'}\left[\left(\frac{V_0}{V}\right)^{K_0'} - 1\right] \tag{2.2}$$

or as

$$V(P) = V_0\left[1 + \frac{K_0' P}{K_0}\right]^{\frac{-1}{K_0'}} \tag{2.3}$$

The fact that the Murnaghan type equation of state is 'invertible' makes it very attractive for use. It does however have the downfall that it is only accurate for compressions of up to about 10%, or $V/V_0 \sim 0.9$. For compressions above this it fails due having $K_0'' = 0$ where experimental data shows a small negative value for K_0'', [15]. This could be overcome by adding an addition term to the bulk modulus, i.e. $K = K_0 + K_0' P + K_0'' P^2/2$, but this results in a complex and impractical $V(P)$ function, [16]. Instead a different type of equation of state, the Birch-Murnaghan, can be used for compressions above 10%.

2.1.2 Birch-Murnaghan EoS

The Birch-Murnaghan, or "finite strain", equation of state is based on the assumption that the strain of a soild under compression can be expressed as a Taylor series in the finite Eulerian strain, given by

$$f_E = \frac{1}{2}\left[\left(\frac{V_0}{V}\right)^{\frac{2}{3}} - 1\right] \tag{2.4}$$

Expansion of the strain to 4th order gives us the following equation of state

$$P = 3K_0 f_E (1 + 2f_E)^{\frac{5}{2}}\left[1 + \frac{3}{2}(K' - 4) f_E + \frac{3}{2}\left(K_0 K_0'' + (K_0' - 4)(K_0' - 3) + \frac{35}{9}\right) f_E^2\right]$$

The 4th order equation of state can be truncated to 2nd order by fixing K_0' to a value of 4, resulting in the coefficient of f_E being exactly zero. The 3rd order Birch-Murnaghan equation of state is the most commonly used. It requires that the f_E^2 coefficient becomes zero and yields a three-parameter equation of state, with V_0, K_0' and K_0'', and has an implied definition for K_0'' given by

$$K'' = \frac{-1}{K_0}\left[(3 - K_0')(4 - K_0') + \frac{35}{9}\right] \tag{2.5}$$

resulting in

$$P = 3K_0 f_E (1 + 2f_E)^{\frac{5}{2}}\left[1 + \frac{3}{2}(K' - 4) f_E\right] \tag{2.6}$$

Therefore for the 3rd order equation of state expressions for the bulk modulus, K_0, and it's pressure derivative, K_0', at pressure P can be defined as [13]

$$K_P = K_0((1_2 f_E)^{\frac{5}{2}}\left(1 + (3K_0' - 5) f_E + \frac{27}{1}(K_0' - 4) f_E^2\right) \tag{2.7}$$

and

$$K_P' = \frac{K_0}{K_P}(1 - f_E)^{\frac{5}{2}}\left(K_0' + \left(16K_0' - \frac{143}{3}\right) f_E \frac{81}{2}(K_0' - 4) f_E^2\right) \tag{2.8}$$

2.2 Phase Transitions and Quantum Criticality

Phase transitions are characterised by a temperature dependence where a physical property shows a clear difference above and below a critical temperature. For each phase an order parameter can be defined with is zero for temperatures outside the phase and non-zero inside the phase. An example could be the case of ferromagnetism, where the order parameter is simply the magnetisation. There are two phase transition depending on how the order parameter changes during the transition. A first order phase

transition is one which has a discontinuity in the order parameter, while a second order transition is one which has a discontinuity in the first derivative of the order parameter.

The Landau theory of ferromagnetism is a mean field theory that simply produces a phase transition arising from some very general considerations. The free energy of a ferromagnet with magnetisation M can be written as a power series in M, and is given by the following expression.

$$F(M) = F_0 + a(T)M^2 + bM^4 \tag{2.9}$$

where F_0 and Bb are constants (it is assumed that $b > 0$) and $a(T)$ is temperature dependant. If $a(T)$ is allowed to change sign at the transition temperature T_c then it can be shown that the above system yields an appropriate phase transition. Therefore in the region of interest, i.e. near the phase transition, $a(T) = a_0(T - T_c)$, where a_0 is a positive constant. The ground state of the system can be found by minimising the free energy and therefore

$$2M[a_0(T - T_c) + 2bM^2] = 0 \tag{2.10}$$

and therefore

$$M = 0 \text{ or } M = \pm \left[\frac{a_0(T_c - T)}{2b}\right]^{\frac{1}{2}} \tag{2.11}$$

These conditions mean that the magnetisation follows the curve shown below in figure 2.1; it is zero for all temperatures above T_c and non-zero and proportional to $(T_c - T)^{1/2}$ below T_c.

In a real system it is found that the magnetisation does behave as $(T_c - T)^{\beta}$ close to the transition, however the exponent β, does not necessarily equal $\frac{1}{2}$, and thus gives us important information about the phase transition. A mumber of exponents, known as

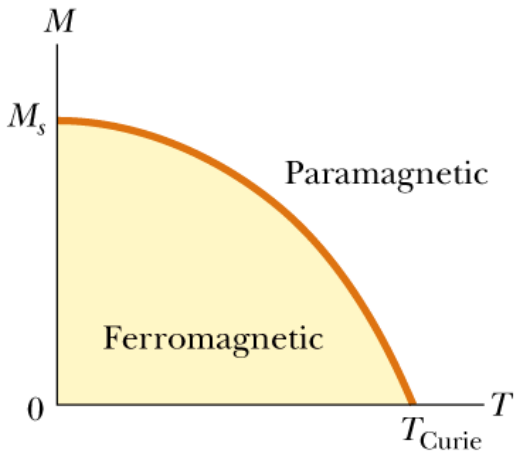

Figure 2.1: Magnetisation of a ferromagnet as a function of temperature

critical exponents, can be defined and experiments have shown that the following is found near the transition

$$\begin{aligned} \chi &\propto (T - T_c)^{-\gamma} && T > T_c \\ M &\propto (T_c - T)^{\beta} && T < T_c \\ M &\propto H^{1/\delta} && T = T_c \end{aligned} \tag{2.12}$$

where β, γ and δ are critical exponents, values of which can be found in table 2.1 for various models.

Model	Mean-field	Ising	Heisenberg
D	any	1	3
d	any	2	3
β	$\frac{1}{2}$	0.326	0.367
γ	1	1.2378(6)	1.388(3)
δ	3	4.78	4.78

Table 2.1: Crtical exponents for various models. D is the dimensionality of the spins and d is that of the lattice of spins

2.2.1 Quantum Phase Transitions and Quantum Criticality

A phase transition that occurs between two states at a finite temperature is known as a classical phase transition. If a transition is driven by a variable other than temperature, for example pressure or magnetic field, then it can in principle occur at zero temperature. If the zero temperature phase transition is second order then it is called a quantum phase transition and the point at which it occurs is called a quantum critical point (QCP).

For a classical phase transition at a finite temperature the correlation length and correlation time diverge as the transition is approached. Therefore the order parameter fluctuates more slowly over an increasing distance as the phase transition is approached. There is some frequency, ω^*, associated with the thermal fluctuations which tend to zero at the transitions temperature. If $k_B T \gg \hbar\omega^*$ close to the transition the critical fluctuations will behave classically. This means that for a quantum phase transition, where $T_c = 0$, quantum flucatuations cannot be ignored and the system can no longer be described classically.

One model that describes the physical properties of a metal at a quantum phase transition is the spin fluctuation model. Although the model defines the system at 0K, for temperatures significantly close to the quantum phase transition the behaviour of the system can still be described by quantum criticality [17]. This treatment follows the "The Magnetic Electron" by G.G. Lonzarich [18]. To simplify the model only fluctuations with frequency $\omega < \omega_c$ and wavevector $q < q_c$, where ω_c and q_c are assumed to be small compared to the Fermi energy and Brillouin zone. These relatively slow large amplitude fluctuations give rise to the singular properties of the quasiparticles. The model begins with a Ginzburg-Landau postulate of the field equation and considers an applied spacially varying but static magnetic field, $H(\mathbf{r})$, of the form

$$H(\mathbf{r}) = H[M(\mathbf{r}] = aM(\mathbf{r}) + bM^3(\mathbf{r}) - c\nabla^2 M(\mathbf{r}) \tag{2.13}$$

Here $a = a_0 - \lambda$ is the inverse of the enhanced susceptibility, χ, of the form $a^{-1} = \chi_0/(1 - \lambda\chi_0)$, and c is a measure of the resistance of the system to spatial varitaions in $M(\mathbf{r})$. For ferromagnets c must be positive. For the following it is useful to introduce an effective field

$$H_{eff} = H - H[M] \tag{2.14}$$

where H is the applied field and $H[M]$ is the right hand side of equation 2.13. In the paramagnetic state M is expected to relax towards equilibrium given by $H_{eff} = 0$. For small H_{eff} and slow variations

$$\dot{M} = \gamma(\mathbf{r}) * H_{eff} \tag{2.15}$$

where $*$ denotes a spatial convolution and $\gamma(\mathbf{r})$ is a relaxation function. Taking the Fourier transforms of the above equation leads to a set expressions that defines the system,

$$H_{\mathbf{q},\omega} = \chi^{-1}_{\mathbf{q},\omega} M_{\mathbf{q},\omega} \tag{2.16}$$

where

$$\chi^{-1}_{\mathbf{q},\omega} = \chi^{-1}_{\mathbf{q}} \left(1 - i\frac{\omega}{\Gamma_{\mathbf{q}}}\right) \tag{2.17}$$

$$\chi^{-1}_{\mathbf{q}} = \chi^{-1} + c\mathbf{q}^2 \tag{2.18}$$

$$\Gamma_{\mathbf{q}} = \gamma_{\mathbf{q}} \chi^{-1}_{\mathbf{q},\omega} \tag{2.19}$$

where $\Gamma_{\mathbf{q}}$ is the relaxation spectrum and can be interpreted as the rate at which a component of $M_{\mathbf{q}}(t)$ will relax to the equalibrium $H = 0$. $\chi^{-1}_{\mathbf{q},\omega}$ is the generalised linear susceptibility defined as $M_{\mathbf{q},\omega}/H_{\mathbf{q},\omega}$. This reduces to $\chi^{-1}_{\mathbf{q}}$ as $\omega \to 0$, the static wavevector dependant susceptibility which goes to χ^{-1} as $\mathbf{q} \to 0$. It is assumed that $\gamma_{\mathbf{q}} = \gamma q^{-1}$ for low $\mathbf{q}$ where n=1 for ferromagnetics and paramagnets and n=0 for systems with large $\mathbf{Q}$.

2.3 Concepts of Superconductivity

Superconductivity is an electronic state of matter than exhibits exactly zero resistance and perfect diamagnetism. When a superconductor is cooled below a critical temperature, T_c, quasiparticles form pairs, known as Cooper pairs, caused by a net attraction in the effective interaction potential. The paired particles become boson-like which allows them to condense into a single ground state below the critical temperature. The critical temperature of the conventional metallic superconductors is typically a few K, however for the unconventional superconductors this can increase by about an order of magnitude.

The most understood mechanism for superconductivity is BCS (Bardeen, Cooper and Schreiffer) theory [2] in which pairing of electrons is mediated via the electron-phonon interaction, refered to as the “conventional” superconductivity mentioned eariler. Electrons near the Fermi surface pair with opposite spin and cystall momentum to form a spin singlet s-wave state. The order parameter for s-wave is homogenous in momentum space and is shown in figure 2.2.

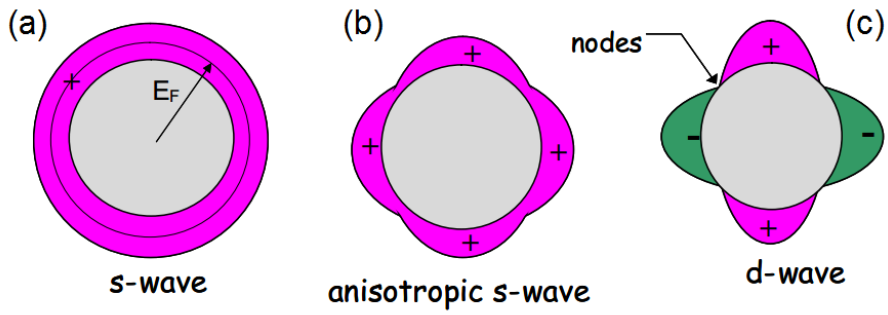

Figure 2.2: Three examples of possible order parameter symmetries. (a) and (b) are known as s-wave and extended or anositropic s-wave, and are both considered to be "conventional". (c) is known as d-wave and are considered to be "unconventional" as they exhibits nodes in the energy gap and a change of sign of the order parameter around the Fermi surface [19].

2.3.1 BCS Superconductivity

As stated above superconductivity occurs due to the formation of Cooper pairs. Removing two electrons from the Fermi sea and linking them by a small attractive interaction is energetically favourable. For the case where there is a Cooper pair plus the Fermi sea there will be two electrons with opposite spin and opposite momentum (for the conventional case). There will be an attractive interaction between the electrons of the Cooper pair which cause scattering after which the total momentum and spin will cancel. There will be an interaction of the Cooper pair with the Fermi-sea via the Pauli exclusion principle only.

The general form for the spatial part of the Cooper pair wavefunction is given by

$$\psi_{cp}(\vec{r}_1, \vec{r}_2) = \sum_{k' > k_F} g_{\vec{k}'} e^{i\vec{K}'\cdot\vec{r}_1} e^{-i\vec{k}'\cdot\vec{r}_2} \tag{2.20}$$

where $g_{\vec{k}'}$ is related to the probablity that the electrons of the Cooper pair have momenta $\vec{k}'$ and $-\vec{k}'$. The energy eigenvalue of the Cooper pair wavefunction is given by the Schrodinger equation

$$\frac{-\hbar^2}{2m}(\nabla_1^2 + \nabla_2^2)\psi_{cp} + V(\vec{r})\psi cp = E\psi cp \tag{2.21}$$

where the interaction potential $V(\vec{r})$ depends on the relative position $\vec{r} = \vec{r}_1 - \vec{r}_2$ of the cooper pair electrons. The energy solution of equation 2.21 is given by

$$E \approx 2E_F - 2\hbar\omega_c e^{-2/N(0)V} \tag{2.22}$$

2.3.2 Unconventional Superconductivity

The BCS theory only predicts a maximum critical temperature of around 40K and therefore a different model is needed to describe the "unconventional" superconductors. All non-s-wave superconductors are considered unconventional which can have nodes and changes in sign of the order parameter around the Fermi surface. Spin fluctuations have been put forward as a candidate for the pairing mechanism responsible for superconductivity in the unconventional superconductors, however there is still much debate over the actual mechanism.

Chapter 3

Experimental Techniques

The techniques required to carry out the high pressure measurements in this thesis are described in this chapter. High pressure for x-ray powder diffraction is created using a diamond anvil cell. The principles of a diamond anvil cell are described including information on preparing and loading a diamond anvil cell, the various pressure transmitting media available and how pressure in the cell is determined. A different type of pressure cell, the Bridgman cell, is used for high pressure magnetic susceptibility measurements. Commissioning of a pulse tube cryostat for x-ray powder diffraction measuring has been performed and low temperature physical property measurements are described.

3.1 High Pressure Techniques

3.1.1 Diamond Anvil Cells (DACs)

A diamond anvil cell (DAC) is a device which allows compression of small samples (tens of microns) to extreme pressures. The principle of the DAC is based around a pair of opposing diamond anvils which squeeze a metallic gasket with a hole in which is placed a pressure transmitting medium, figure 3.1. Maximum pressures of up to 600 GPa [20] have been achieved. The use of diamond for the anvil has the advantages of having very

high strength and is transparent over a very wide spectral range, including infra-red, visible, ultra-violet and x-ray wavelengths, making it a very versatile device that can be used for many different experiments. The diamond anvil cell consists of three main parts; a mechanism for anvil alignment, a sliding mechanism and a mechanism to apply a load. The diamond anvil cells used for measurements here were equipped with anvil with 300μm culet diameter to cover a suitable large pressure range.

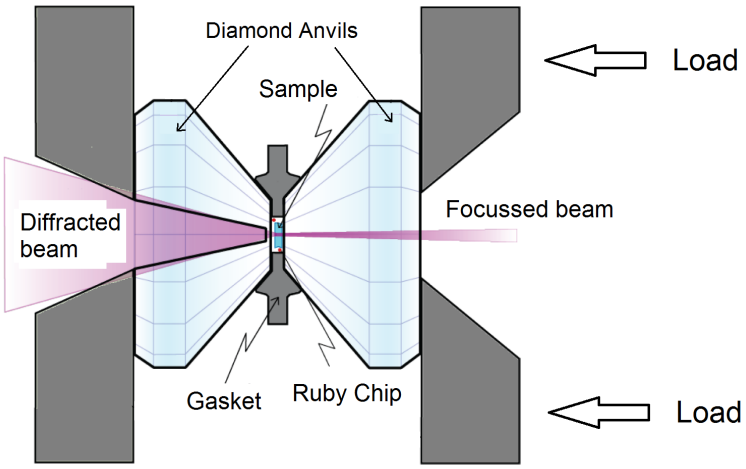

Figure 3.1: Schematic of a diamond anvil cell. Pressure is created in the cell by squeezing the gasket between the two opposing diamond anvil culets by applying a load to one of the anvils. X-ray radiation can pass through the cell to perform powder diffraction measurements.

Force is generated in a Holzapfel-Syassen diamond anvil cell, figure 3.2a, by a lever arm mechanism that pushes a piston into the cell body. Two counter-wound coupled threads (3) are attached to the lower end of the lever arms (2). Turning the threads moves the lower ends of the arms together and pulls the piston (1) further into the cylinder of the cell body. The lower anvil in the cell body is mounted on a backing plate placed at the bottom of the cylinder which is secured in place by four grub screws that are used to align the anvil across the cell. The upper anvil is mounted on a rocking hemisphere which is secured into the piston of the diamond anvil cell. The hemisphere can be tilted in all directions by four screws which push on it through the top of the piston and allow for the two anvil culets to be aligned parallel to each other. The long piston and cylinder ensure that the anvils remain perfectly aligned with each other.

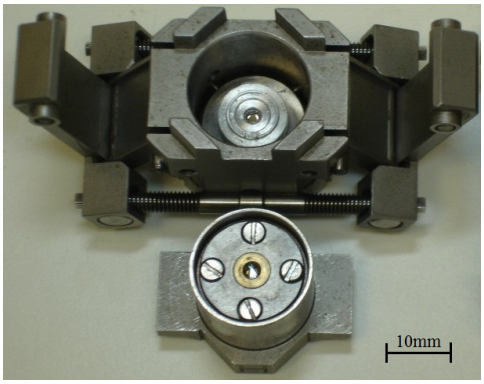

(a)

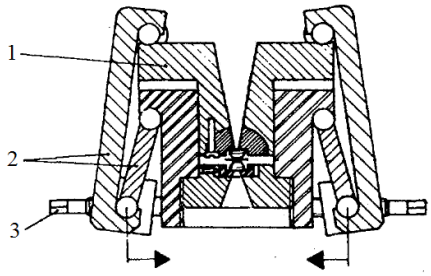

(b)

Figure 3.2: Image and schematic of the Holzapfel-Syassen type DAC used for high pressure x-ray diffraction measurements. (a) Main body and piston of a Holzapfel-Syassen cell. (b) Holzapfel-Syassen cell. 1. Sliding piston, 2. Lever arm assembly, 3. Thread [21].

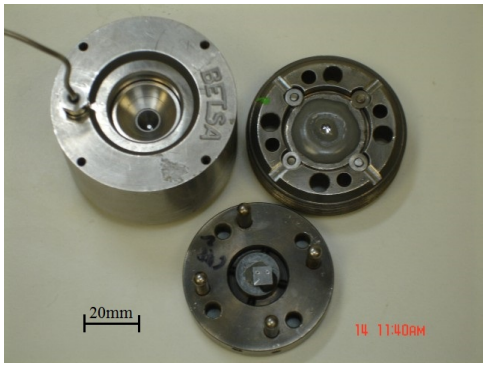

(a)

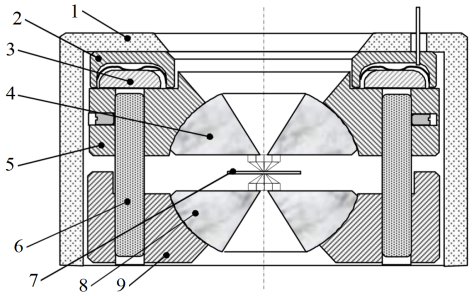

(b)

Figure 3.3: Image and schematic of the Membrane type DAC used for high pressure x-ray diffraction measurements. (a) Upper and lower parts of the membrane type cell with membrane pressurising cover. (b) Membrane cell. 1. Cover, 2. Membrane, 3. Washer, 4. Upper hemisphere, 5. Piston, 6. Guidance post, 7. Gasket, 8. Lower seat, 9. Cylinder [21].

A second type of diamond anvil cell is the membrane type cell. The anvils are each mounted on backing plates as for the Holzapfel-Syassen cell. The main difference is how the top and bottom parts of the cell are aligned and held together. The top part of the cell, which contains the rocking hemisphere backing plate, slides onto four equally spaced posts attached to the bottom part of the cell, in which the other backing plate is mounted. There are two methods of applying a load to the membrane cell to push the anvils together. The first simply uses four screws to hold the two parts of the cell together which can be tightened to increase the load. Several spring washers are

used on each screw to allow for very fine adjustment of the load. The membrane cell can be screwed into a cover which is used for the second method of pressurisation. A thin stainless steel gas membrane is placed between the cell and the cover which when pressurised will expand pushing the sliding part of the cell into the bottom part held in place by the cover. The pressure in the gas membrane can be very slowly increased via a pressure drive giving very fine and smooth control of the load applied to the membrane cell.

3.1.2 DAC Preparation and Loading

The choice of gasket material for a diamond anvil cell is important as it must be strong enough to provide a sufficiently thick layer of material between the anvils under the highest pressures required. The gasket must also provide lateral support to the diamond anvils and therefore only non-brittle materials can be used. Stainless steel is commonly used as a gasket material. Rhenium is also good for very high pressure experiments as although it is initially rather soft it strengthens very much under plastic deformation. Before a hole can be drilled in the gasket to form the sample chamber the gasket must be pre-indented to avoid large deformation and instability under pressurisation. A gasket typically has an initial thickness of ~ 0.2mm which is pre-indented to $\sim 50\mu$m. The gasket is fixed on to one of the anvils in such a way that it can be placed back later in the same place. The correct thickness of the indent is achieved by pressurising the diamond anvil cell to a pre-determined pressure found by placing a ruby chip between the anvil and gasket and using the ruby fluorescence method, see Section 3.1.3. The gasket is removed from the cell and the hole drilled in the centre of the indent using either a mechanical or laser drill or by spark erosion. The gasket hole has a diameter of about $150 - 200\mu$m depending on the the culet size, maximum pressure required and pressure transmitting medium to be used. Any small burrs must be removed from the hole using a small needle before the gasket is cleaned using acetone and a ultrasonic bath. The gasket is placed back on the anvil and is smoothed out and centred by

assembling the cell and applying a very small load.

The diamond anvil cell can then be loaded with a sample, pressure calibrant and pressure transmitting medium. A photo of a loaded sample chamber of a closed diamond anvil cell is shown in figure 3.4. Samples are prepared by grinding the bulk material into a fine powder. The powder is squeezed between two glass slides and then cut into suitable sized pieces under a microscope. The sample is placed in the gasket hole using a fine needle. The thickness of the sample must be thin enough so that it does not get crushed by direct contact with the anvils even at the very highest pressure of an experiment.

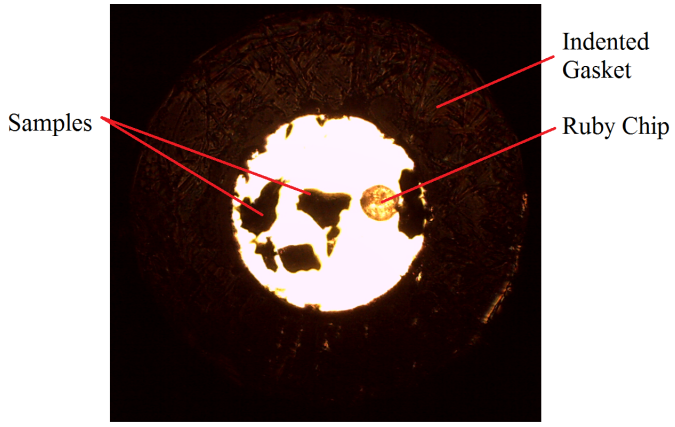

Figure 3.4: Sample chamber loaded with several samples and a ruby chip for pressure determination

3.1.3 Pressure Determination

The easiest method is the ruby fluorescence technique. A small ruby chip is placed in the gasket hole which is illuminated with a visible laser and its fluorescence measured using a spectrometer. The spectrum of the fluorescence of the ruby contains two very distinct peaks, known as the R1 and R2 lines, whose positions shift to higher wavelengths with increasing pressure.

The behaviour of the R1 line on application of pressure has been very well defined and the ruby scale was first introduced by Piermarini [22] [23] when it was calibrated against the Decker equation of state of NaCl up to 19.5 GPa [23]. Since then further work has been performed to increase the range of the ruby scale to higher pressures. The pressure in the cell is calculated by the following equation [24]

$$P = \frac{1904}{B}\left[\left(\frac{\lambda}{\lambda_0}\right)^B - 1\right] \tag{3.1}$$

where P is the pressure in GPa, λ is the shifted position of the wavelength of the R1 line in nm and λ_0 is the wavelength of the R1 line at zero pressure. The parameter B is equal to 5 for hydrostatic and 7.665 for non-hydrostatic conditions. Fully hydrostatic conditions are taken to be only for the use of a gaseous pressure medium. All other media, including even the best liquid media are taken to be non-hydrostatic. The standard value for λ_0 is 694.24nm. A precise value for λ_0 must be used for accurate pressure measurements which is obtained from measuring the wavelength of the R1 line of a ruby chip placed on a glass slide at ambient pressure.

This equation has been used for pressure determination in this thesis. A ruby fluorescence spectrum in a helium pressure medium around 10 GPa is shown in figure 3.5 compared to the same pressure in silicon oil. The much narrower, more defined R1 and R2 peaks in the helium spectrum indicate a much more hydrostatic pressure environment.

In some situations there will be no optical access to the diamond anvil cell, for example during low temperature experiments, and therefore the ruby fluorescence technique cannot be used. An alternative is to use the equation of state of an internal x-ray calibrant. A diffraction pattern of the calibrant is obtained in addition to the sample for each pressure. The lattice parameters of the calibrant obtained from the pattern

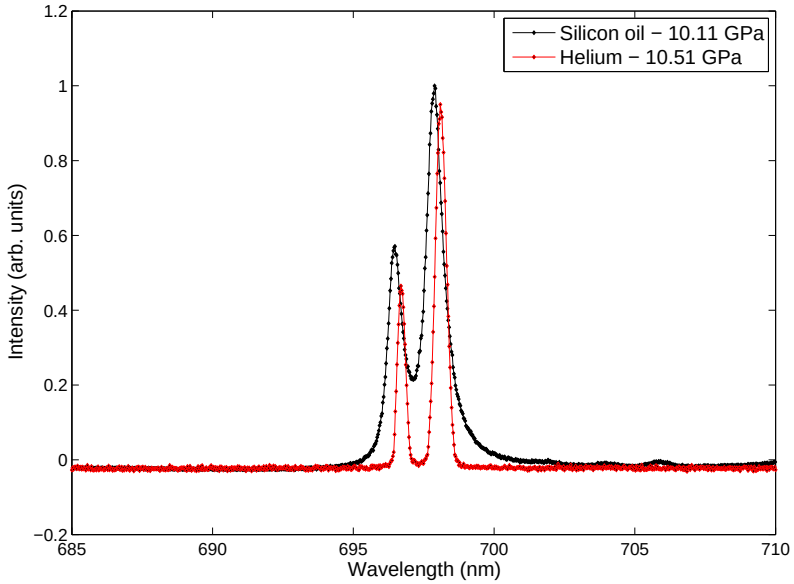

Figure 3.5: Comparison of ruby fluorescence spectra in silicon oil and helium pressure media for similar pressures. The helium pressure medium provides a much more hydrostatic pressure environment indicated by the narrow R1 and R2 lines in the ruby fluorescence spectrum compared to the silicon oil.

can be used with it's equation of state to obtain a pressure. A copper calibrant was used for pressure determination during some experiments in this thesis. The equation of state of copper at room temperature is given by

$$P(V) = \frac{140}{4}\left[\left(\frac{V}{47.24}\right)^{-\frac{1}{4}} - 1\right] \tag{3.2}$$

where $P(V)$ is in GPa and V is the unit cell volume of copper. For measurements at low temperature a low temperature equation of state can be used to determine the pressure. Due to the solid pressure medium required for low temperature measurements here, all conditions have been taken to be non-hydrostatic.

3.1.4 Pressure Transmitting Media

A pressure transmitting medium in the gasket hole provides a "hydrostatic" pressure to the sample from the uniaxial force that is applied to the diamond anvils. As the load on the cell increases the volume of the sample chamber decreases as the gasket hole

becomes thinner increasing the pressure. Solid, liquid or gaseous pressure transmitting media can be used in a diamond anvil cell.

A solid pressure medium is probably the easiest to use. Before the cell is closed the gasket hole is filled will a few small pieces of the solid medium, for example NaCl, and then pressed with the other anvil to completely fill the hole. The top anvil is then removed and the excess pressure medium is removed. The sample and pressure calibrant can be placed on to the pressure medium and the cell can be closed. Alternatively, two solid discs of medium can be placed in the gasket hole sandwiching the sample and calibrant. The solid pressure transmitting medium must be chosen considering the maximum pressure required in the experiment.

A more hydrostatic pressure environment within the sample chamber can be achieved by using a liquid pressure transmitting medium, which are probably the most commonly used. The selection of an appropriate liquid medium for an experiment can be difficult as there are many different options available. In 1973 Piermarini *et al.* [25] discovered that a 4:1 methanol-ethanol mixture remains truly hydrostatic up to almost 10 GPa, above which a glass transition occurs. The simplicity and reasonably high pressure region of this medium makes it one of the most popular. Further to this Piermarini *et al.* [26] found that that addition of water to make a 16:3:1 methanol-ethanol-water mixture remains hydrostatic up to 14.5 GPa. More recently a comparative study of the solidification of several different liquid pressure transmitting media was carried out by S. Klotz [27]. The highest hydrostatic pressures of several liquid pressure transmitting media from this study along with several others are summarised in table 3.1. Although a liquid medium has the advantage over a solid one in that it produces a hydrostatic pressure to higher pressures they do have several disadvantages. Some liquids can dissolve or react with a sample, causing the experiment to be unsuccessful. Another problem is that there is a high possibility that the sample can be displaced or even

entirely washed away during the filling of the gasket hole, resulting in the need for several loadings. Finally, a liquid such as methanol-ethanol will evaporate very quickly when using the small quantities required to load the diamond anvil cell. This can mean the gasket hole could be closed with no pressure medium causing it to close up, requiring the preparation of a new gasket.

Pressure Medium	Glass Transition	Reference
4:1 Methanol-ethanol	10.5 GPa	[27]
16:3:1 Methanol-ethanol-water	14.4 GPa	[27]
1:1 Pentane-isopentane	7.4 GPa	[27]
Isopropyl alcohol	4.3 GPa	[22]
Petroleum ether	$\sim$6 GPa	[28]
Daphne oil	3.7 GPa	[27]

Table 3.1: Glass transitions of various liquid pressure transmitting media below which the the pressure is considered hydrostatic.

By far the best hydrostatic conditions are created by using a gaseous pressure transmitting medium, particularly helium. Even up to 60 GPa the distribution of pressure across a helium sample has been observed to be less than 1% [29]. The maximum hydrostatic pressure of other rare gases were measured by Bell and Mao [30] and are summarised in table 3.2. Judging by the splitting ruby fluorescence lines xenon can be considered hydrostatic up to 55 GPa [31] and even up to 100 GPa pressure gradients across the xenon sample achieve 1.0 GPa μm^{-1} [32].

Pressure Media	Maximum Pressure	Reference
Helium	70 GPa	[21]
Argon	9 GPa	[30]
Neon	15 GPa	[27]
Xenon	55 GPa	[31]
Nitrogen	10 GPa	[27]

Table 3.2: Several gaseous pressure transmitting media and their maximum hydrostatic pressures.

One way to load a diamond anvil cell with a helium pressure transmitting medium is to load it as a cryogenic liquid, however this can be difficult due to the need to use

a cryostat. A more superior method, invented by Pinceaux in 1979 [33], is to load a compressed gas at room temperature.

The process requires both a compressor and a high pressure vessel known as the "bomb". A photo of a commercially available gas loading system is shown in figure 3.6. The slightly open diamond anvil cell is placed in the bomb which is then pressurised to $\sim$ 1500 bar. If loading a membrane cell the gas membrane is pressurised to the same pressure as the bomb. The cell can then be closed trapping the high pressure medium in the gasket hole. The Holzapfel-Syassen type cell is closed using a motor that enters the bomb to turn the screws on the lever arms. To ensure that the cell is completely closed the screws are turned a number of times determined from previous trial loadings. Once the cell is closed the pressure in the bomb can be lowered to atmospheric pressure leaving the cell loaded at 1500 bar. The membrane cell is closed by applying an additional pressure, δP to the gas membrane to push the cell together. A sapphire window in the bottom of the bomb allows the gasket hole to be monitored on closing to determine when the cell is fully closed. After the cell has been closed the pressure in the bomb is released whilst maintaining the δP with the membrane. Loading the cell with a compressed gas rather than cryogenic liquid has several advantages; it traps a high density of gas in the gasket hole, the sample and calibrant remain in exactly the same position, the pressure medium is very pure and the loading time is much shorter. A typical gas loading can be completed in about an hour. An important consideration when using a gaseous pressure medium is that gases are very compressible at low pressures and therefore the initial gasket hole must be large enough to allow for it to shrink on closing the cell.

3.1.5 Bridgman Cells

Apart from the diamond anvil cell there are several other types of pressure cell available one of which is the Bridgman type cell [34]. Although the highest pressures achievable

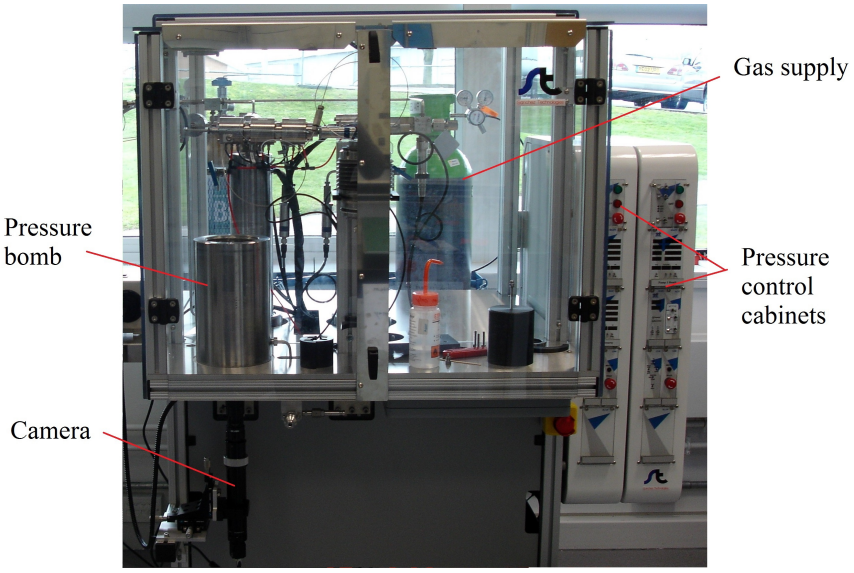

Figure 3.6: Photo of the gas loading system used for loading diamond anvil cells with gaseous pressure transmitting media. The high pressure bomb is inside the safety shielding on the left side.

are much lower than for a diamond anvil cell the Bridgman cell has the advantage of a much larger sample space which allows for the complex electrical transport or magnetic measurements. Pressure is achieved in the Bridgman cell by squeezing the gasket between a pair of opposing tungsten carbide or sintered diamond anvils. The anvil used in the Bridgman cells for this thesis were tungsten carbide with a 3.5mm culet which produce a maximum pressure of about 10 GPa. Figures 3.7b and 3.22a show a diagram of the anvil mounted in the cell and an exploded view of the cell components respectively.

All components of the pressure cell are made from heat treated beryllium-copper. The lower anvil is mounted in a screw which holds it in place in the bottom of a cylinder. The cylinder has four windows which to allow wiring to enter the cell. The upper anvil is mounted in a piston that slides into the cylinder and rests on top of the gasket. A plate is placed in the cylinder on top of the piston and secured in place with a lock nut that screws into the top of the cylinder. A hydraulic ram is used to apply pressure to the cell via a piston which passes through a hole in the lock nut which pushed on the piston. The pressure is held by tightening the lock nut once the load has been applied.

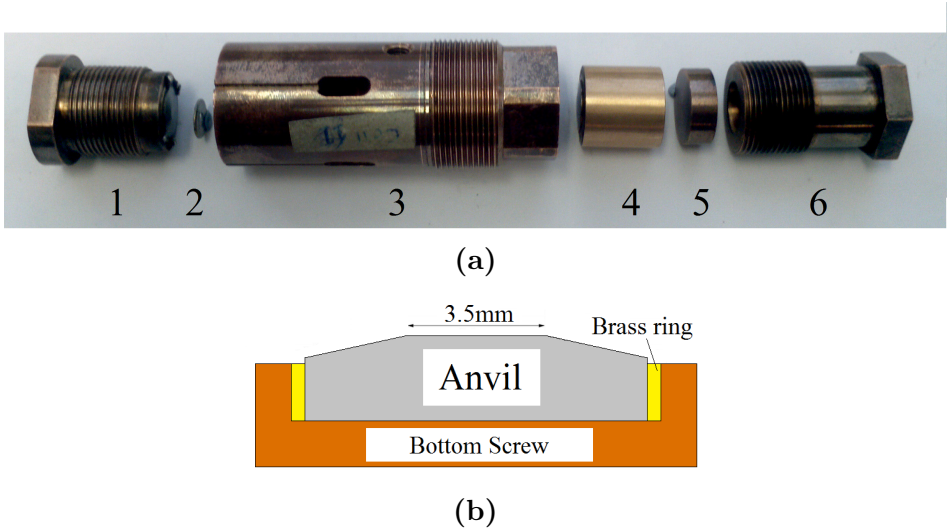

Figure 3.7: (a) Exploded view of the components of a BeCu Bridgman type pressure cell fitted with tungsten carbide anvils. 1. Bottom screw and anvil, 2. stainless steel gasket, 3. cylinder, 4. piston and top anvil, 5. plate, 6. locking screw. (b) Diagram of the lower anvil mounted in the bottom screw of the Bridgman cell.

A grub screw is screwed into the side of the cylinder which locates with a groove down the side of the piston to prevent the piston from rotating in the cylinder and damaging the setup as the lock nut is tightened. An exploded view of the Bridgman cell, including the anvils, can be seen in figure 3.22a. Wires for all electrical connections are solder to copper contact pads placed on the bottom screw around the outside of the anvil.

There are several gasket materials available for use in the Bridgman type pressure cell. One of the most common materials, often used for high pressure electrical resistivity measurements, is pyrophyllite, however this is not well suited to a liquid pressure medium. These problems can be overcome by using a stainless steel gasket. If using stainless steel the gasket first needs to be pre-indented to avoid the hole collapsing or deforming on initial pressurisation. A stainless steel disc with an initial thickness of $\sim$0.5mm is placed on the culet of the lower anvil glued in place with a thin layer of diluted GE varnish. The cell is then assembled and a load of about 1.5 tons applied to cell using the hydraulic ram to indent the gasket to about 200μm. The cell is taken apart and the indented gasket removed from the lower anvil to have a hole drilled in the centre for the sample chamber. A mechanical drill is used to drill a 2mm hole in the

centre of the indent. Any burrs are removed by hand using a larger drill. The prepared gasket is placed back on the lower anvil and secured in place with either a thin layer of GE varnish or a few small spots of epoxy around the edge.

There are two different types of pressure transmitting media that can be used in the Bridgman cell; a solid or liquid medium. Solid pressure media are generally used with a pyrophyllite gasket. Not only will the solid medium produce less hydrostatic conditions in the sample chamber compared to a liquid medium it is also undesirable as it can destroy delicate experimental setups. Attempts have been made to use a liquid pressure with a pyrophyllite gasket and a method which involves sealing the inside wall of the gasket with epoxy was initially developed by Jaccard et al. [35]. However, it is very difficult to fill the gasket hole without any liquid coming into direct contact with the pyrothylite which causes the gasket to become unstable and collapse on pressurisation. The use of a stainless steel gasket removes all of the problems as it can simply be flooded with the liquid pressure medium before closing the cell. Information on the pressure transmitting media can be found in section 3.1.4. Attempts to use pentane-isopentane as a pressure transmitting medium was unsuccessful as it would always evaporate before the cell could be closed. The use of methanol-ethanol as a pressure transmitting medium dissolved parts of experimental setups and therefore could not be used. Daphne oil 7373 was finally chosen for all Bridgman cell measurements in this thesis as although it solidifies at a relatively low pressure of 3.7 GPa [27] it does not react with any samples or the experimental setups, and does not evaporate.

Unlike the diamond anvil cell the Bridgman cell has no optical access to sample chamber and so the ruby fluorescence method explained in section 3.1.1 cannot be used to determine the pressure. Instead a superconductive pressure gauge is used. The pressure dependence of the superconducting transition temperature of In, Pb and Sn is well defined [36] [37] and therefore can be converted into a pressure inside the cell. The

superconducting transition is observed as either a drop in electrical resisitivity or discontinuity in magnetic susceptibility. A Pb calibrant was chosen for a pressure calibrant for measurements here. The pressure, P, is related to T_c by [38]

$$P = a + bT_C + cT_C^2 \tag{3.3}$$

where $a = 3.506GPa$, $b = -0.769$ GPaK^{-1} and $c = 0.04$ GPaK^{-2} and P is in GPa. Even at pressures as high as 30 GPa a Pb pressure calibrant can be used as the drop in T_c can still easily be measured. The pressure dependence of T_c of Pb has been directly calibrated by ruby fluorescence measurements at low temperatures [39].

3.2 X-ray Powder Diffraction

3.2.1 Generation of X-rays

X-ray powder diffraction measurements in this thesis were all performed using radiation produced from the Diamond Light Source synchrotron. A synchrotron uses guiding magnetic fields to guide electrons in a circular orbit to emit electromagnetic radiation in the x-ray spectral range. A schematic of the main parts of the synchrotron is shown in figure 3.8.

The electrons that are accelerated by the Diamond synchrotron are produced by an electron gun which uses a high voltage cathode that produces electrons via a process called thermionic emission. An electric field in the electron gun is used to produce a stream of electrons with an initial energy of 90 keV. The stream of electrons enters a linear accelerator, or linac, which accelerates the electrons further in a linear trajectory to 100 MeV through a series of alternating electric fields. The 100 MeV electrons are then injected from the linac into a booster synchrotron where they are accelerated in an oval trajectory to a final energy of 3 GeV. The electrons are accelerated in the

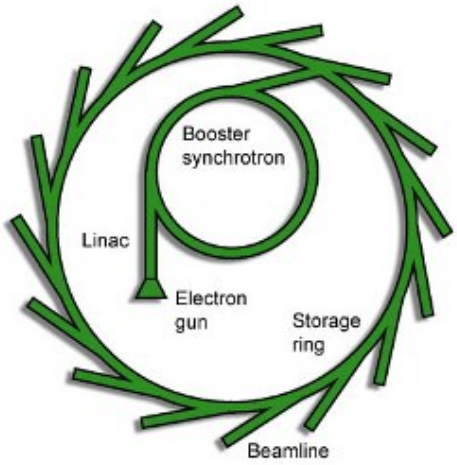

Figure 3.8: Diagram of the major components of the synchrotron [40].

booster synchrotron in the straight sections by a radio frequency voltage source and the curvature around the bend maintained by magnetic fields of up to 0.8T produced by a series of dipole magnets. The electrons finally enter a storage ring in which they create x-ray radiation due to their radial acceleration. The storage ring consists of twenty four straight sections which are arranged to create a closed loop. The electron beam is curved between the straight section by large dipole, or bending, magnets.

There are several beamlines located around the storage ring which use the x-ray radiation. Each beamline is made up from four sections; 1. an insertion device which generates the x-ray radiation from the electron beam, 2. an optics hutch where the light is conditioned, 3. an experimental hutch which houses all experimental equipment and 4. a control cabin for controlling the experiments. Experiments in this thesis were performed on the I15 Extreme Conditions beamline at Diamond Light Source. Figure 3.9 shows a diagram of the beamline. The I15 beamline uses an insertion device called a wiggler to generate x-rays from the storage ring. The x-ray radiation from the wiggler is conditioned using a set of instruments in the optics hutch. The beam is first collimated by a set of slits before it enters A cryo-cooled Si(111) double crystal monochromator (DCM) to select the energy of the radiation required for an experiment. The energy is selected by rotating both crystals to vary the Bragg angle whilst keeping the crystals

parallel to each other. Following the DCM there is a vertical focusing mirror (VFM) and a horizontal focusing mirror (HFM) to focus the beam to 70μm at the sample position. The beam passes through from the optics hutch into the experimental hutch via a main shutter. The final beam size required at the sample position is produced by the passing the beam through a pinhole. The pinhole is a short length of tungsten bar with a very narrow hole, 20-70μm drilled in the centre along its length.

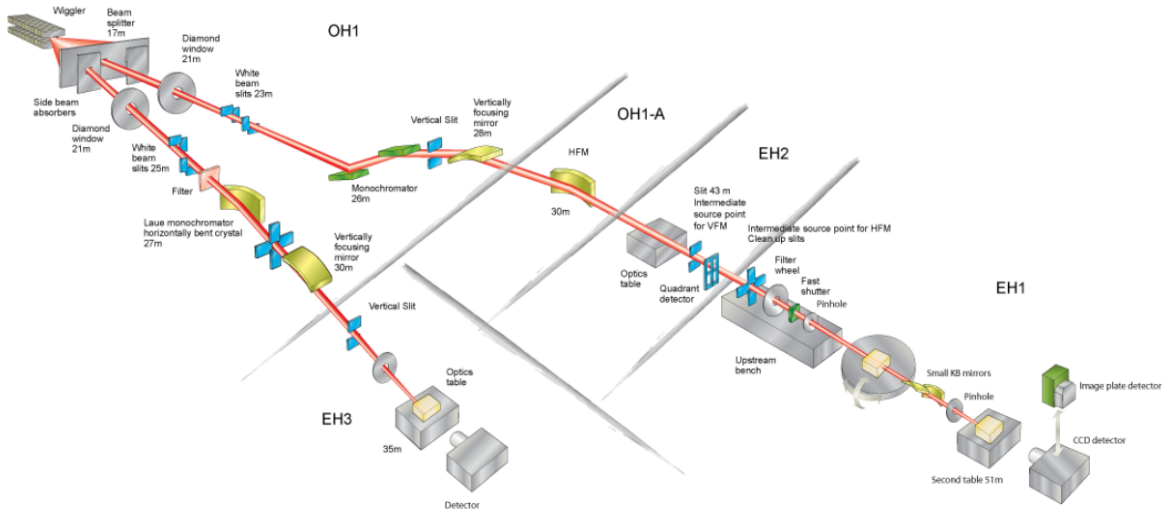

Figure 3.9: Diagram of the I15 Extreme Conditions beamline [41].

3.2.2 X-ray Powder Diffraction Measurements

The sample is mounted on a kinematic mount which allows it to always be placed on the sample stage of the diffractometer in a reproducible position. The sample stage can be moved in all translational directions and rotated in the horizontal plane relative to the beam. The sample is scanned across the beam in both perpendicular directions to align the centre of the sample in the centre of the beam and on the centre of rotation of the sample stage. A second diode, positioned in the beam just after the sample, measures the beam intensity as the sample is moved and traces out the sample shape due to the differing absorption from the sample, gasket, pressure cell, etc. For low temperature experiments the cryostat is mounted on the diffractometer on a stage which can also be moved in all translational directional relative to the beam. The sample is aligned by

scanning the entire cryostat across the beam so that the edges of the window upstream of the sample are found to obtain a rough position of the cell. A finer set of scans near this position are used to find the exact position of the sample.

A beam stop is aligned in the beam in front of the detector by scanning it in both directions perpendicular to the beam and measuring the intensity of the x-rays downstream from it using a diode. The transmitted intensity will drop to zero as the beam stop moves into the beam path and increase again when it moves out of the beam. The midpoint of these two positions give the position where the beam stop should be positioned. A Pb shield is placed over the detector throughout the beam stop alignment to avoid damage from the intense beam. An x-ray powder diffraction pattern is taken of a standard sample, usually silicon or cerium dioxide, to calibrate the sample-to-detector distance and calculate the beam centre and tilt of the detector. The standard sample is loaded into a gasket hole and mounted on a dummy pressure cell or a glass capillary. The collected pattern of the standard is loaded into a software program called Fit2d [42] or DAWN for calibration. The program uses the known positions of diffraction rings in each standard sample and uses them with the beam energy to calculate the distance, beam centre and tilt of the detector.

Diffraction patterns are collected using one of two avaliable area detectors. The Mar345 image plate detector has a round plate diameter of 345mm and pixel size of 100μm. The Perkin Elmer is a square flat panel detector with a size of 2048×2048 pixels and pixel size of 200μm. The Mar345 is generally used for energies below 30 keV and the Perkin Elmer energies above 40 keV. Although the resolution of the Perkin Elmer is lower it is sometimes more useful due to its short cycle time for obtaining and outputting images, making it more suitable for experiments where many diffraction patterns need to be acquired. Exposure times are generally between about 30 and 300 seconds depending on the scattering power of the sample. In an experiment the sample is rotated, or rocked, a few degrees during the exposure to improve the powder averaging in the final

image.

The powdered samples used for measurements will contain tens of thousands of tiny, randomly oriented crystallites. Some of these crystallites will be oriented such that they diffract the incoming beam to produce a Debye-Scherrer cone with half angle $2\theta_{hkl}$ according to Bragg's law, equation 3.4 for a particular hkl plane.

$$n\lambda = 2d\sin(2\theta) \tag{3.4}$$

There will also be some crystallites oriented such that they satisfy the Bragg equation for other hkl planes each producing a cone with a different 2θ angle. The detector intersects the Debye-Scherrer cones perpendicular to the beam to collect the series of diffraction rings, as in figure 3.10. For an "ideal" powder the diffraction image contains very fine unbroken rings due to the very larger number of crystallites, however in reality the powder will not be ideal and will contain a smaller number of crystallites with a mixture of different grain sizes. This means that the Debye-Scherrer cones will appear grainy, made up of many different sized spots. The nature of the sample or sample preparation can sometimes lead to a preferential orientation of the crystallites. This could occur if a single crystal powdered to form long thin crystallites which when pressed into a pellet will have a tendency to align along their length. Preferential orientation is seen in an image as long intense arcs in the Debye-Scherrer rings. High pressure images will usually contain fairly large intense spots from single crystal reflections from the diamond anvils.

The Debye-Scherrer rings which have been recorded by the area detector need to integrated to produce an equivalent intenisty vs. 2θ diffraction patterns which can be used to obtain structural information of the sample. Integration of patterns is performed using the Fit2d program [42]. The calibration parameters for the detector obtained from the standard sample are used to translate the intensity at each detector pixel to

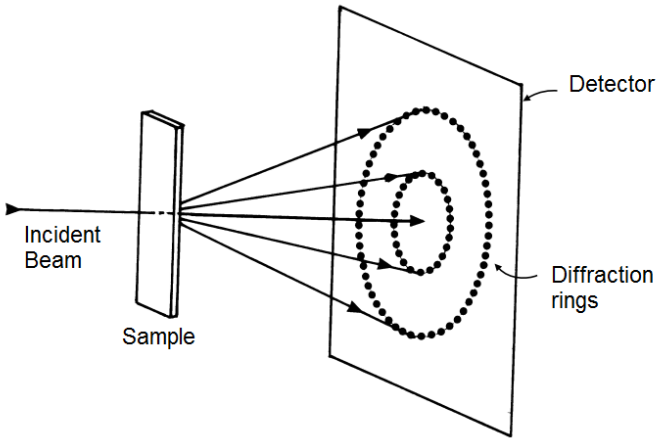

Figure 3.10: Diagram of the diffraction of x-rays from a powder or polycrystalline sample. Each rings consist of reflections from many crystallites orientated to satisfy Bragg's law for a particular hkl plane [43]

its corresponding 2θ angle. All intensities at the same angle are summed to produce the intensity vs. 2θ pattern. Each ring of the detector image will produce a peak in the pattern at it's 2θ angle. A detector of a silicon standard sample and its integrated diffraction pattern are shown in figure 3.11. The Fit2d program allows parts of the detector images to be masked and excluded from the integrated pattern so that the intensity does not appear in the diffraction pattern. The masking can be used to exclude over exposed detector pixels or single crystal diamond peaks that would show up as large unwanted features in the intensity patterns.

Structural information about the sample is obtained by performing a refinement of the powder diffraction pattern. A refinement takes a structural model calculated from an initial set of lattice parameters and other peak and profile parameters and updates them to minimise the difference between the model and the observed data. Powder diffraction patterns were analysed using Le Bail type refinements in order to extract lattice parameters. The space group and rough initial values for lattice parameters are required to perform the Le Bail refinement. Before the structural phase is calculated the background is determined which takes the form of an n-order polynomial. A theoretical pattern is calculated from the initial lattice parameters, added to the calculated

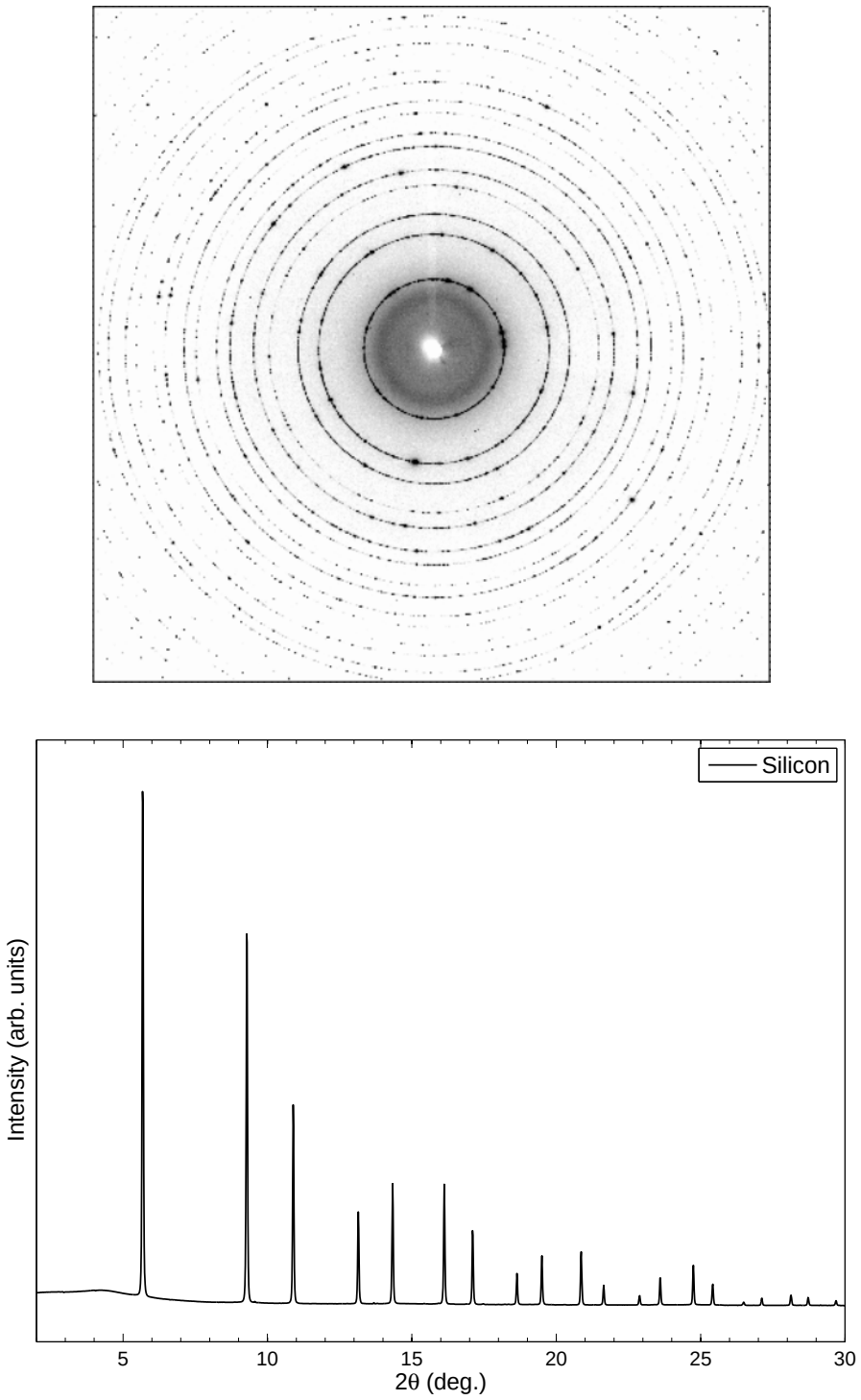

Figure 3.11: *Top*: X-ray powder diffraction detector image of the a silicon standard obtained using 40 keV x-rays and a sample-to-detector distance of 427.8mm. *Bottom*: Integrated intensity vs. 2θ pattern of the above detector image.

background and the difference to the observed data is analysed. The lattice parameters of the model are updated and a new model calculated. If the difference between the model and data is smaller then the new values are taken. The process is repeated until

the difference is minimised. A pseudo-Voigt peak function, $PV_{UA}(x)$, was found to describe the peak shape of diffraction patterns and was used for all refinements which is defined by

$$PV_{UA}(x) = \eta L_{UA}(x) + (1-\eta)G_{UA}(x) \tag{3.5}$$

where $G_{UA}(x)$ and $L_{UA}(x)$ are Gaussian and Lorentzian components defined as the following

$$G_{UA}(x) = \left(\frac{2\sqrt{(ln(2)/\pi)}}{fwhm}\right) \exp\left(\frac{-4ln(2)x^2}{fwhm^2}\right) \tag{3.6}$$

$$L_{UA}(x) = \left(\frac{2/\pi}{fwhm}\right) \Big/ \left(\frac{1+4x^2}{fwhm^2}\right) \tag{3.7}$$

where $fwhm$ is the full-width at half maximum of the peak. The refinement process aims to minimise the quantity

$$S_y = \sum_i w_i(y_i - y_{ci})^2 \tag{3.8}$$

where w_i is a weighting factor equal to $1/y_i$ and y_i and y_{ci} are the intensities of the observed and calculated patterns at the $i-th$ 2θ value. An indication of the goodness of fit of the theoretical pattern to the data is given by calculating the weighted profile factor R_{wp} given by the following

$$R_{wp} = \left(\frac{\sum_i w_i(y_i - y_{ci})^2}{\sum_i w_i(y_i)^2}\right)^{\frac{1}{2}} \tag{3.9}$$

A perfect fit of the model to the data would have an R_{wp} equal to zero. Some times for diffraction patterns in pressure cells equation 3.8 is not the most useful indication of fit quality as the larger background can significantly reduce the R_{wp} values calculated.

Here it is more useful to a usa a quantity called the Bragg R-factor which gives a measure of the agreement between the reflection intensities calculated from the model and those from the model. The Bragg R-factor is given by

$$R_{Bragg} = \frac{\sum_i |I^i_{obs} - I^i_{calc}|}{\sum_i |I^i_{obs}|} \tag{3.10}$$

where I^i_{obs} and I^i_{calc} are the 2θ positions of the $i-th$ peak of the observed and calculated patterns. In the refinement R_{Bragg} is useful as it only depends on the fit of the structural parameters not the profile parameters.

3.3 Low Temperature Measurements

3.3.1 Pulse-Tube cryocooler at I15

The pulse tube cryo-cooler is a VeriCold VT-4 cryogen free cryostat used for x-ray powder diffraction measurements at low temperatures. The cryostat covers a temperature range of around 6 to 300K reaching a base from room temperature in about 6 hours at the maximum cooling rate. The temperature can be swept much more slowly with a minimum rate of around 0.001K/min. A photo of the cryostat mounted on the diffractometer of the beamline and a schematic of the cross-section of the cryostat are shown in figures 3.12a and 3.13 respectively.

The operation of the cryostat is based on a closed loop helium expansion cycle. The system consists of two major components; a room temperature compressor and an expansion chamber attached to a cold head inside the cryostat [44]. Helium gas is compressed in the compressor at room temperature and then sent to the cold head where it is expanded to produce cooling. The compressed gas is cooled by a high capacity regenerator before it enters the cryostat. The cryostat is cooled as the gas expands and leaves the cold head. There are no moving parts inside the cryostat in

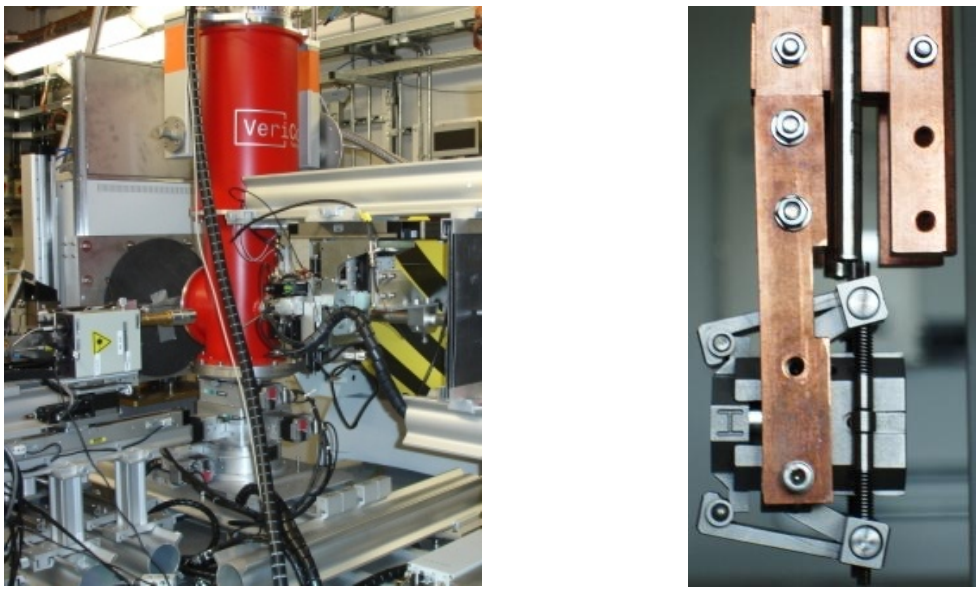

(a) (b)

Figure 3.12: (a) Pulse tube cryostat mounted on diffractometer. (b) DAC mounted on the probe of the pulse tube cryostat.

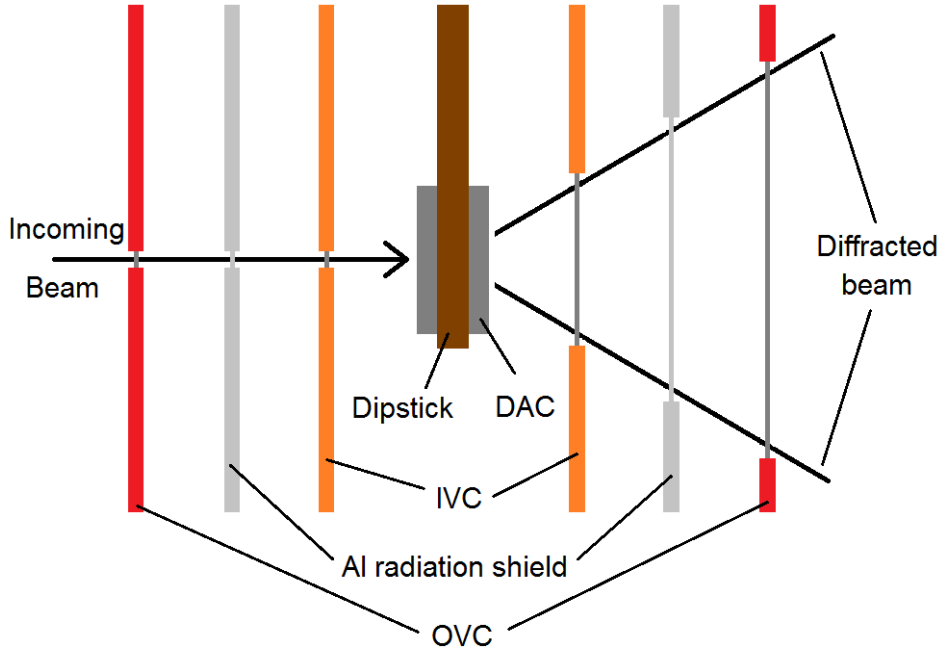

Figure 3.13: Schematic of a DAC mounted on the probe of the pulse tube cryostat showing the path of the x-ray beam through the different components. *DAC*: diamond anvil cell, *IVC*: inner vacuum can, *OVC*: outer vacuum can. OVC and IVC include beryllium windows to allow transmission of x-rays.

the pulse tube system which avoids vibrations. The cold head has two cooling stages which are attached to 70K and 4K stages of the cryostat in an outer vacuum chamber (OVC). Thermal conductivity to a dipstick inserted into an inner vacuum can (IVC), or sample chamber, is achieved by direct thermal couplings to the cryostat. An aluminium radiation shield is placed between the OVC and IVC to minimise heating in the sample chamber from radiation.

Temperatures in the cryostat and dipstick are monitored by several thermometers. A platinum resistance thermometer is mounted on each of the 70K stages of the cryostat and dipstick. Temperatures of the 4K stage is measured using a Cernox temperature sensor. A 100Ω resistor is mounted on the 4K stage of the dipstick insert as a heater for temperature sweeps and stabilisation. All wiring for the cryostat thermometry is connected through a serial socket in the top of the OVC. A 24-pin socket in the break-out box on the top of the dipstick is used for all thermometer and heater wiring on the dipstick.

3.3.2 Commissioning of Cryostat with X-rays

Extensive work has been performed to introduce the possibility of carrying out low temperature - high pressure x-ray powder diffraction on the I15 beamline for both measurements in this thesis and any future beamline users. This work has included both modifications to the cryostat to optimise low temperature performance and characterisation measurements fully understand the background of low temperature powder diffraction patterns due to the various cryostat components. A Holzapfel-Syassen type diamond anvil cell can be mounted on the bottom of the dipstick using a specially made mount that bolts on to the bottom of the 4K stage. A small amount of thermal grease is used between the cell and the mount to increase thermal conductivity. A second 24-pin connector in the break-out box of the dipstick provides all electrical connections for the pressure cell and additional thermometer. An important modification was the

addition of a second Cernox temperature sensor mounted on the diamond anvil cell mount positioned very close to the pressure cell to obtain a more accurate temperature at the sample position. A heater, a 100ω resistor, was added close to the sample and many cooling cycles performed to optimise PID parameters to reach a temperature set point as fast as possibly.

To allow x-rays to be transmitted through the cryostat and sample for powder diffraction measurements the OVC and IVC are fitted with thin beryllium windows. During measurements diffraction will occur from these windows and the aluminium radiation shield as well as from the sample producing additional peaks in the diffraction patterns. The background diffraction pattern from the cryostat was characterised to identify the origin of each of the peaks. The cryostat was placed on the beamline with the radiation shield and all beryllium windows removed. A distance of 381.47mm from the position of the sample in the sample chamber and the detector was determined using a CeO_2 standard. Each of the components downstream from the sample were individually fitted to the cryostat and 30 keV x-rays were used to record their diffraction pattern. This was repeated for the two downstream beryllium windows and downstream aluminium radiation shield. The components upstream of the sample were not measured as any diffraction from them during measurements will be blocked by the IVC and the pressure cell in the sample chamber. Each of the detector images was integrated using the distance to the sample position. The diffraction of the individual components can be seen in figure 3.14. Finally a diffraction patterns of the entire assembled cryostat, including the upstream components was recorded, and again integrated using the distance to the sample. Comparison between the entire cryostat an individual component patterns allowed the origin of each peak to be identified. A diffraction pattern of the fully assembled cryostat with no sample loaded into the sample chamber is shown in figure 3.15 with each peak labelled with their corresponding component. As there was no sample there are a small number of unlabelled peaks from diffraction from upstream

components. The CeO_2 standard was loaded into the fully assembled cryostat and the diffraction pattern was recorded. The additional peaks in the integrated pattern compared to the empty cryostat pattern in figure 3.15 can easily be identified as from the sample. A refinement of the pattern, figure 3.16, only fits the peaks from the CeO_2. Measurements were taken of standard samples loaded in DACs using different pressure transmitting media to identify any issues. with each. It was found that the small sample required when using a helium pressure transmitting medium did not produce a signal that could be seen above the cryostat background. Even when using a liquid pressure medium the large still did not produce a good signal. This means that a low temperature measurements must be performed using a solid pressure transmitting medium, or even no pressure medium, in order to maximise the sample signal in final diffraction patterns. If a solid medium can be used it has the advantage of that it can be used as an internal x-ray calibrant. Different approaches to buliding up the pressure-temperature phase were investigated. Initially it had been planned to use mechanical drive rods in the cryostat dipstick to increase pressure at low temperature. However, the drive rods were found to fail, possibly due to thermal contraction locking the cell together, and therefore could not be used to increase the pressure. The drives rods could not be strenghtened as this would have significantly increased the heat leak to sample space impacting thermal performance. This approach to measurements would have also meant that multiple cell loadings would need to performed during experiments. A second approach to thebuild up the pressure-temperature phase diagram was to only use one sample loading and start several cool downs from different starting pressures. Multiple measurements can then be taken at different temperatures throughout the cool down to take a cut throught the phase diagram. The system is then warmed to rrom temperature and the pressure increased. All the work carried out on the cryostat not only allowed sucessful measurements to be carried out for this thesis but also means that all future beamline users can make efficient use of any beamtime to aquire quality data.

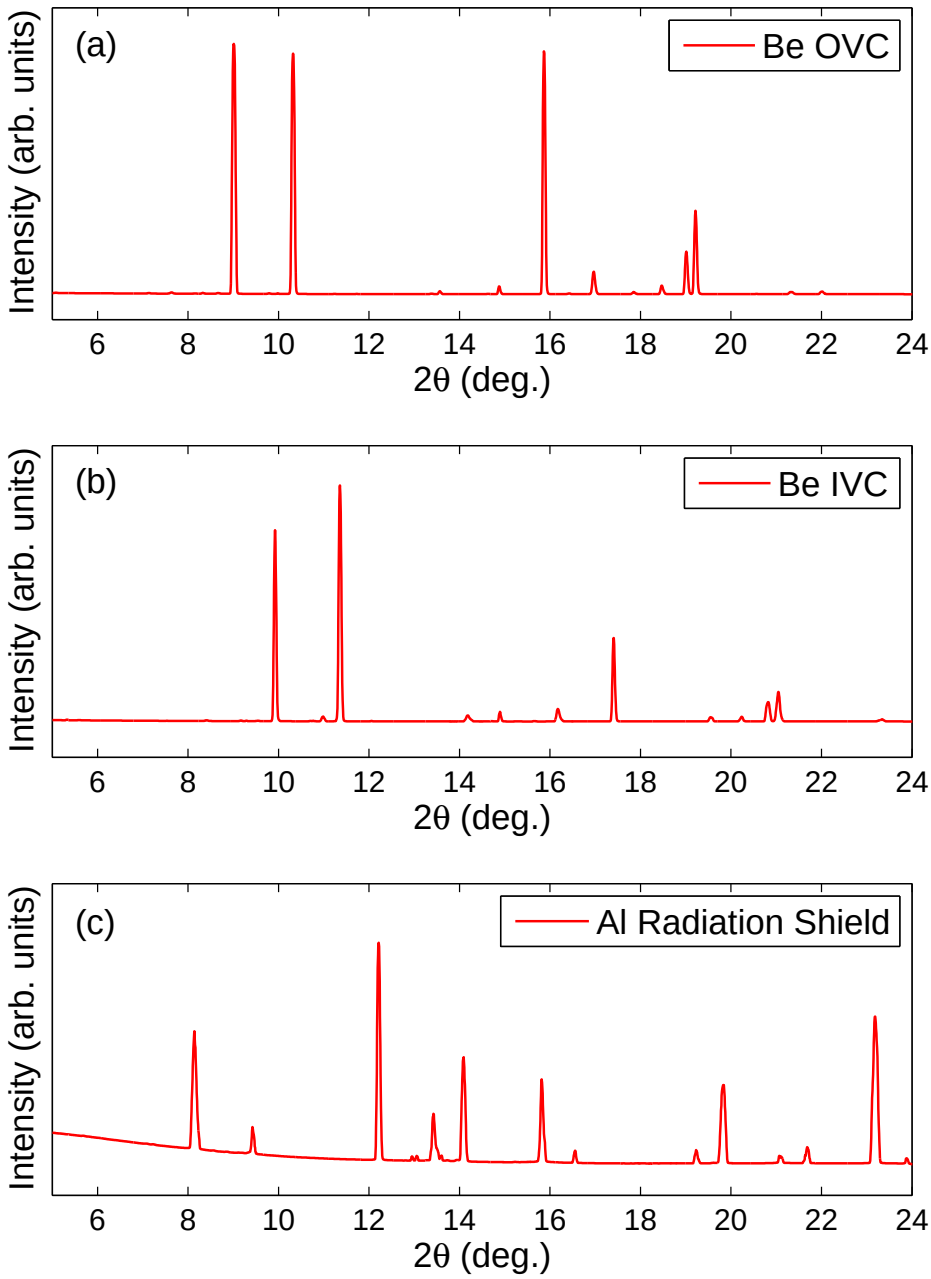

Figure 3.14: X-ray powder diffraction patterns of the beryllium windows and aluminium radiation shield downstream from the sample/cell with a beam energy of 30 KeV. Upstream components will be similar with shifted 2θ values however are not shown here as they will be blocked by a the cell loaded into the cryostat.

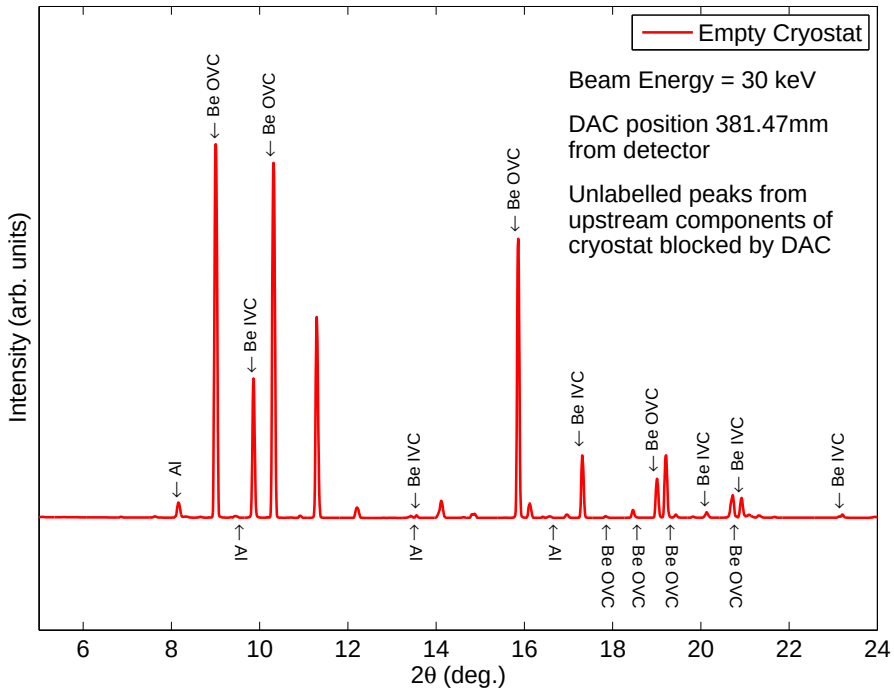

Figure 3.15: Background powder diffraction pattern of cryostat with no cell loaded using a beam energy of 30 KeV. Peaks are labelled with their corresponding cryostat component. Any unlabelled peaks are from upstream components and will not be present in low temperature measurements.

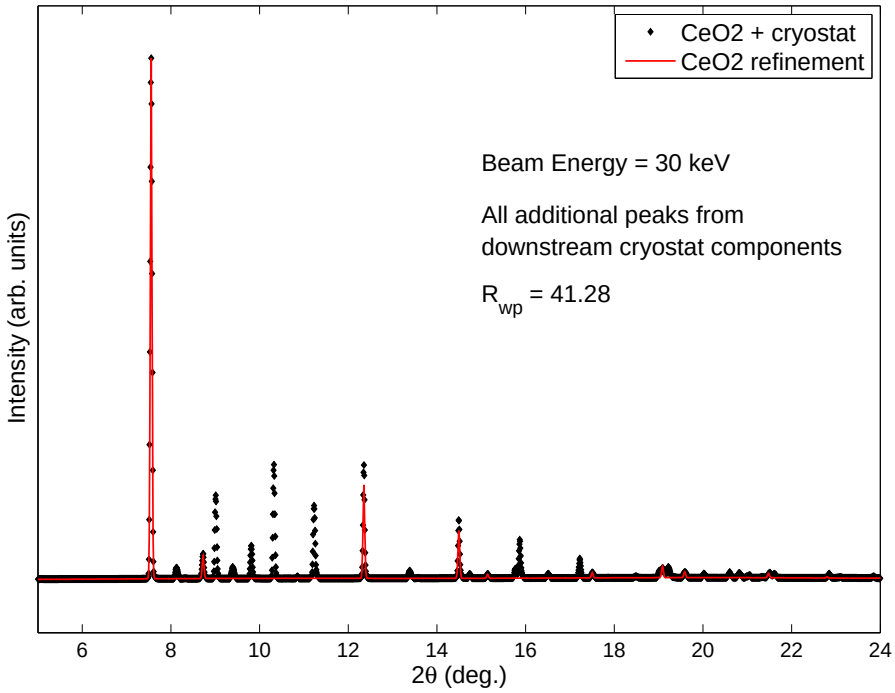

Figure 3.16: Refinement of a 30 keV powder diffraction pattern of a CeO_2 standard placed in the cryostat. The unfitted peaks are from the cryostat background. The large R_{wp} factor is due to the unfitted peaks of the cryostat no being included in the refinement.

3.4 Electrical Resistivity and Magnetic Susceptibility Measurements at Low Temperature

3.4.1 Physical Properties Measurement System (PPMS)

The Quantum Design Physical Properties Measurement System (PPMS) is an automated cryostat designed to study the physical properties of a sample in a precisely controlled temperature environment. Several standard PPMS options allow for measurement of magnetic, electro-transport, specific heat and thermo-electric properties. The PPMS can also be used for non-standard measurements such as high pressure resistivity or magnetic susceptibility. The temperature can be varied at a rate between 0.01 and 12K/min over a wide range 1.9 to 400K with an accuracy of ±0.5%. A superconducting magnet is incorporated into the PPMS which allows measurements to be carried out in magnetic fields of up to ±9T. The magnet is composed of copper embedded with a niobium-titanium alloy which is constantly immersed in the helium bath. All electrical connections for experiments are made via a sample puck which locates in a 12-pin connector feedthrough at the base of the sample chamber. A diagram of a PPMS sample puck is shown in figure 3.17. The pucks can also be used to provide connections for any custom experiments.

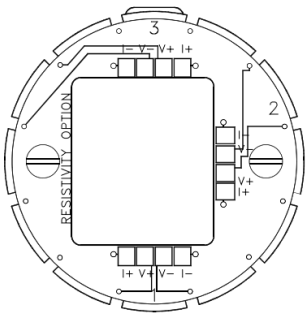

Figure 3.17: Diagram of a PPMS sample puck.

The PPMS three main components; the dewar, the probe, a control cabinet which contains all electronics, a vacuum pump and valves for pumping. The dewar contains a liquid helium bath in which the probe is immersed. The dewar also contains a nitrogen

jacket to reduce helium consumption. The probe of the PPMS incorporates the sample chamber, basic temperature control hardware, a helium level meter, gas lines and the sample puck connector. The superconducting magnet is also mounted on the probe. Figure 3.18 shows a labelled diagram of the PPMS probe.

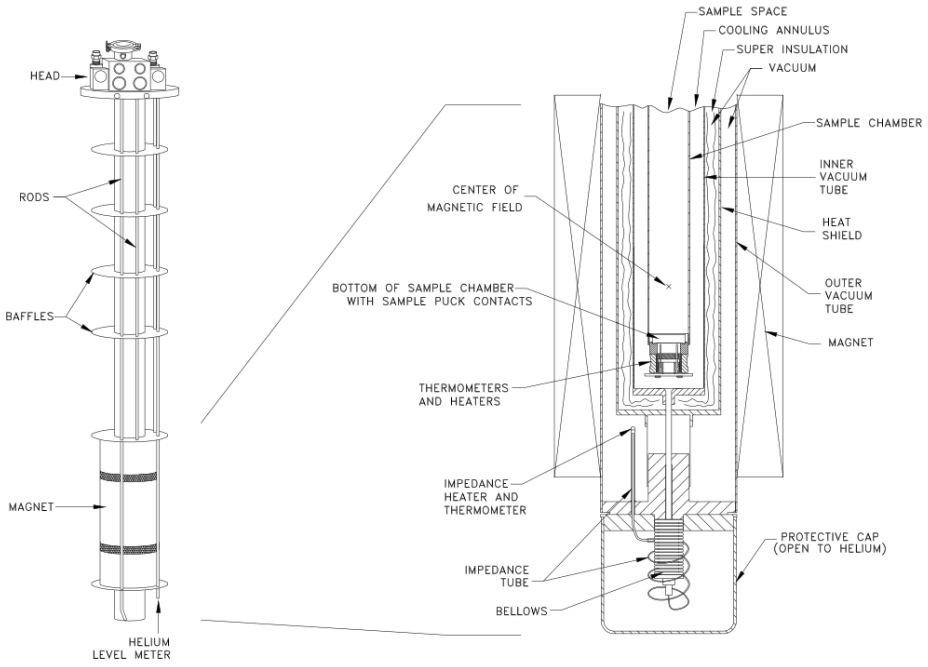

Figure 3.18: *Left*: Schematic of the PPMS probe. *Right*: Cross section of the lower part of the PPMS probe showing the sample space, cooling annulus and impedance assembly [45].

The theory of operation of the PPMS is taken from the Quantum Design PPMS hardware manual [45]. Temperature control is achieved by drawing cold helium vapour through a cooling annulus which surrounds the sample chamber. The helium vapour enters the cooling annulus through an impedance assembly at the bottom of the probe. For temperatures above 4.2K a block heater at the base of the sample chamber heats the sample and warms the helium vapour in the cooling annulus to uniformly warm the sample chamber. For temperatures below 4.2K the PPMS offers two different operating regimes; pot-fill mode and continuously low temperature control. When using pot-fill mode as the temperature reaches about 4.2K liquid helium is drawn through the main impedance to fill the cooling annulus. The boiling point of this helium is

then manipulated by pumping on the liquid controlled by the impedance flow control valve. Although this cooling method provides very accurate temperature stability below 4.2K it has the disadvantage that temperature control is lost when transitioning through 4.2K. The second method removes this problem and the temperature transitions smoothly through 4.2K, making it much more desirable for temperature sweep measurements. It involves completely turning off the main impedance and drawing helium vapour through a second carefully tuned flow impedance that greatly restricts the gas flow. The heater at the base of the sample chamber is used to heat the sample and helium vapour directly. Thermal conductivity to the sample in the PPMS is achieved through direct coupling of the sample puck to the base of the sample chamber and a few mbar of helium exchange gas in the sample chamber. The bottom of the sample chamber is isolated from radiation from the probe head by a baffle assembly that is placed into the sample chamber.

Sample temperature is constantly monitored by two thermometers mounted at the base of the sample chamber directly underneath the sample puck connector. A platinum resistance thermometer is used for temperatures in the range of approximately 80 to 400K. Lower temperatures, approximately 1.9 to 100K are read using a Cernox thermometer. The temperature in the crossover region between 80 and 100K uses a weighted average of the two different thermometers. There is a second Cernox sensor mounted on the neck of the of the sample chamber just above the sample region to monitor temperature gradients and aid temperature control.

Ambient pressure characterisation of both the resistivity and magnetic susceptibility of a sample are performed using the PPMS. Resistivity measurements are carried out using a four-point-probe technique. Four 25μm gold or platinum wires are attached across the sample, either by spot welding or using a conductive epoxy, which are then attached to a resistivity sample puck as shown in figure 3.19. An AC current is passed

through the sample via the two outside wires and the potential difference across the sample measured via the two inner contacts. The resistance of the sample can be obtained simply by using Ohm's law. The dimensions of the sample and voltage lead separation are measured before the measurement to be able to convert the resistance to resistivity. A small current is used to minimise sample heating. The voltage leads in the four-point-probe technique draw very little, and ideally zero, current through the sample and so the voltage drop across the sample can be measured very accurately as contact resistance is virtually eliminated. A current frequency away from multiples of mains frequency is chosen to minimise electrical noise. Resistivity pucks for the PPMS contain connections for multiple four-point measurements so that multiple samples can be measured simultaneously.

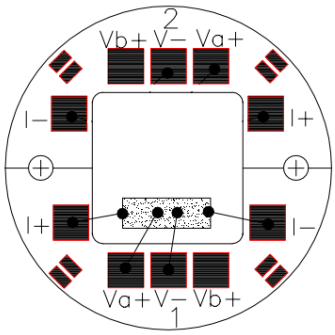

Figure 3.19: Schematic of a PPMS resistivity puck with a sample mounted for a four-point measurement on the lower channel [46]

Magnetic susceptibility measurements of samples can be performed in the PPMS by using an additional insert, figure 3.20, that fits directly into the sample chamber which houses a coilset of driving and detection coils, a thermometer and all electrical connections. The sample is mounted on the end of a thin rigid rod that holds it within the coilset and can be translated longitudinally by a servo motor mounted on top of the sample chamber. Before a measurement the sample must be located in the centre of the detection coilset so that it can be correctly positioned in the detection coils. During a measurement the sample is held stationary in the centre of a detection coil whilst a small alternating magnetic field is applied by the driving coil to induce a magnetic

moment. A driving field of the order 10^{-4} T is used to excite the sample. The magnetic response of the sample to the driving field is measured as a current induced in the detection coil. A schematic of the measurement circuits can be seen in figure 3.21. The top and bottom detection coils are counter-wound in series which eliminates the driving field from the detected signal. Five readings are taken for each measurement. The first reading measures the response of the sample located in the centre of the lower detection coil, then the second with the sample located in the upper detection coil. The sample is returned to the centre of the lower coil and the response measured again for the third reading. The final two readings are calibration readings which are both taken with the sample centered between the two detection coils.

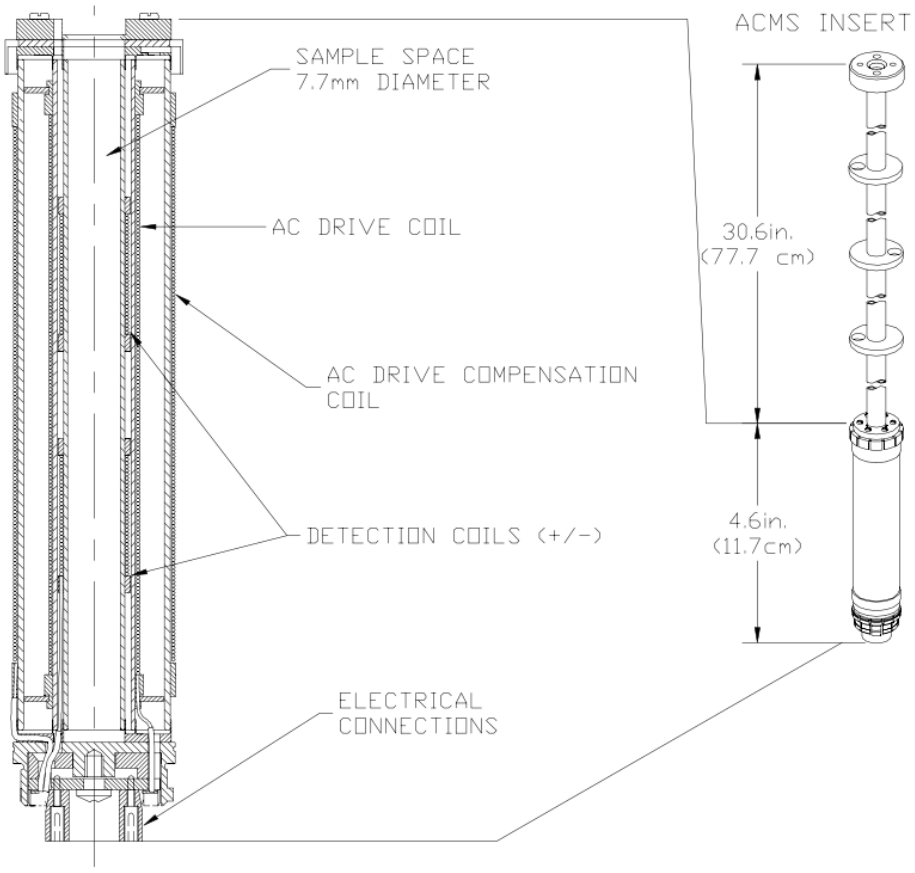

Figure 3.20: ACMS insert and coil set [47].

In addition to the PPMS measurement pucks for standard measurement options there are also blank pucks avaliable on which custom experiments can be assembled. The

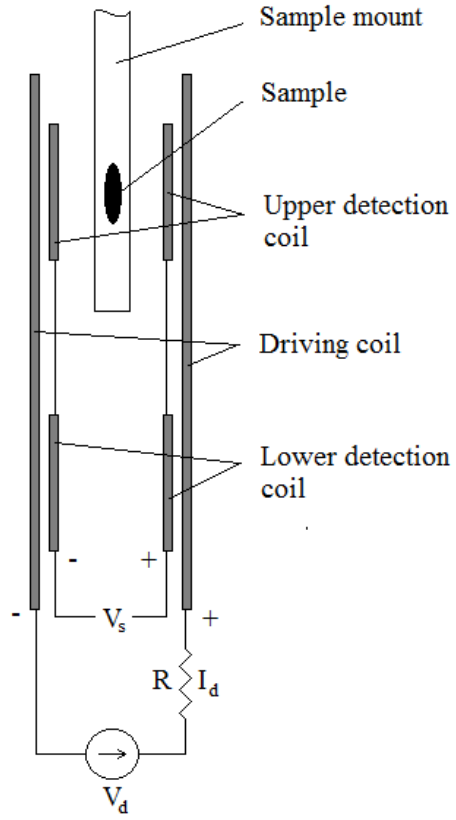

Figure 3.21: Schematic of the AC Susceptibility insert for the PPMS. V_d and V_s are the voltages in the driving and detection coil circuits. R is a resistor placed in the driving circuit to produce the driving current I_d. The sample is positioned in the centre of the upper detection coil.

Bridgman pressure cell is mounted on one of these blank pucks to provide all electrical connections and thermal conductivity to the bottom of the PPMS sample chamber. A screw is secured attached to the top of the blank puck to which the bottom screw of the pressure cell can be screwed on to. A thin layer of thermal grease between the puck and screw is used to improve thermal conductivity. Wires from the pressure cell are soldered to small copper contact pads that are glued to the puck around the edge of the screw.

3.4.2 Development of High Pressure Susceptibility Measurements

The magnetic susceptibility of a sample can be measured at high pressure by compacting down the size of technique explained above to fit with the sample chamber of a pressure cell. As mentions in previous sections, a crucial point in high pressure experiments is the pressure conditions in the sample space of the pressure cell which ideally should be as hydrostatic as possible to produce the best possible results. This obviously means that is is desirable to use a gaseous or liquid pressure transmitting medium. Several techniques for these types of measurement have been developed using diamond anvil and other types of pressure cell [48] [49] [35]. Methods have involved the placement of the detection coil both inside and outside of the gasket hole. The use of a diamond anvil cell seems like an obvious choice to produce the best hydrostatic conditions for the measurements. However, due to the small size of the sample chamber a compensation coil, for subtracting the driving field, has to be placed away from the gasket with an auxillary driving coil. The Bridgman cell offers a significantly larger sample chamber volume and transport measurements are often performed in them utilising a pyrophyllite gasket with a solid pressure transmitting medium. This not only comes with the disadvantage of the less hydrostatic pressure environment it is also undesirable as the solid pressure medium can easily destroy delicate detection coil setups in the sample chamber. This has led to the development of a new type of high pressure susceptometer based on initial work by Chris Harrison [50] that can be used to measure the superconducting transition temperature of a sample. The method involves placing both the detection and compensation coils inside the sample chamber of the pressure cell and makes use of a stainless steel gasket so that a liquid pressure medium can be used. The new approach of the Bridgman cell with the liquid pressure medium allows for much more accurate measurements, especially at higher pressures that would ordinarily be very non-uniform in traditional measurements using solid pressure media. A further important advantage of this new method is that by placing both the sample and

compensation micro-coil inside the sample space it allows them to be placed as close together as possible therefore minimising any difference in the background measured in each. It also simplifies the experimental setup by only requiring one driving coil and eliminating the need for a second driving coil for the compensation micro-coil if it were positioned outside the sample space.

The stainless steel gasket is prepared as described in section 3.1.5. In addition to the usual indent two grooves are added to the gasket to allow two wires for the detection coils to enter the sample space. The grooves are made by pressing a small length of tungsten wire into the gasket using about 25 bar of pressure from the hydraulic ram. The experimental setup is built directly in the gasket hole and around the outside of the lower anvil. A pair of counter-wound micro-coils, to act as detection and compensation coils, are placed in the gasket hole and the wires to them placed in the gasket grooves. The detection coils are formed by winding 35μm insulated copper wire around a 0.5mm diameter piece on tungsten wire. Each coil is made up of eight turns. The 35μm wire can be easily broken when the cell is pressurised, however the use of thicker wire greatly reduces the number turns that can fit in the sample chamber. The two coils are wound in opposite directions in series using the same length of copper wire on the former before being removed and turned up parallel to each other. Stycast 2850FT saturated with alumina powder is used to fill the gasket grooves and hold the detection coils in place. The Stycast-alumina powder mixture used to fill the grooves is almost entirely alumina powder. During preparating alumina powder is continually added to the Stycast until it becomes saturated and not more can be mixed in. This is because it is only alumina that is required to seal the sample chamber and insulate the wires when pressure is applied, and the Stycast only really acts to hold the alumnia powder together before pressurisation. The Stycast-alumina mixture is pressed flush with the top of the gasket to ensure a good seal on closing the cell by gentle heating to allow it to partially cure before being pressed with the upper anvil with a pressure of about 50 bar. Grooves

made with tungsten wire with a diameter 55μm were not large enough to ensure the wires were fully insulated from the gasket during pressurisation. Larger grooves greatly improved the insulation of the wires however the gasket under the grooves was too thin and caused the gasket to fail at low pressures. The use of 100μm tungsten wire to make the grooves reduced the success rate of the cells however ensured that the gasket survived to high pressures. After pressing the entire setup is heated for an appropriate time to allow the Stycast to fully cure. The two ends of the detection coils are soldered to two of the contact pads around the edge of the lower anvil. A driving coil is formed by winding 150 turns of insulated 50μm copper wire around an 8mm tungsten bar. The driving coil is secured in place using a small amount is GE varnish and the ends soldered to two more of the copper contact pads. Wires are added to each of the contact pads to provide electrical connections to the outside of the cell through the windows in the cylinder of the Bridgman cell. A twisted pair comprised of two 100μV insulated copper wires is used for each of the driving and detection coil circuits. The sample is placed in one of the detection coils and a piece of Pb placed in the other to be used as a pressure calibrant. The cylinder of the pressure cell is screwed on to the bottom screw and the twisted pair put through the windows. A small drop of pressure transmitting medium is added to the gasket hole using a small syringe and the cell can be closed and pressurised. The pressure cell is then screwed on to the PPMS sample puck and wires attached.

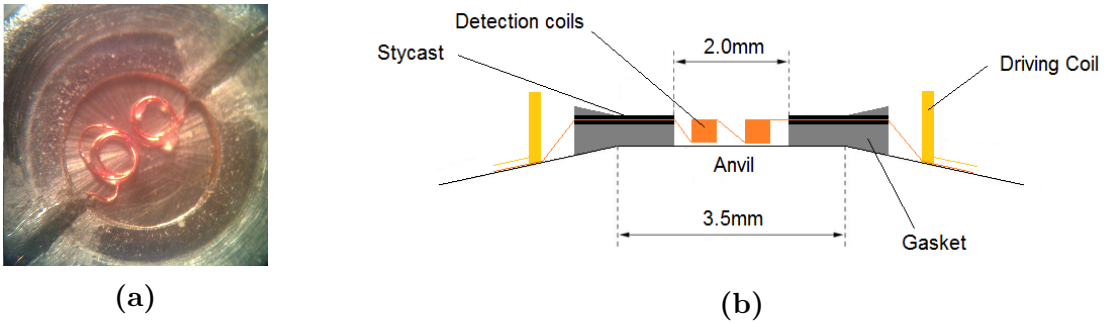

Figure 3.22: (a) Photo of the high pressure susceptibility cell setup built directly on top of the bottom anvil of the Bridgman pressure cell. (b) Schematic of the experimental setup showing the driving coils and pickup coils.

The measurement works in a similar way to that described for ambient pressure characterisation of magnetic susceptibility. An output of a lock-in amplifier is used to pass a current through the driving coil to produce a driving field and induce a magnetic moment in the sample. The magnetic response of both the sample and Pb pressure calibrant will induce a voltage in each of the detection coils which is read by the lock-in amplifier. As the voltages detected will be very small, or the order of nm, the use of a lock-in amplifier for this means that only voltage signals of the same frequency as the driving field are detected and noise is mostly eliminated from the measurement. The driving field will be approximately removed from the measured as the detection coils will produce equal and opposite voltages which cancel each other. As a sample goes through a superconducting transition a fraction of the magnetic flux will be driven outside of the detection coil and therefore a jump or discontinuity will be observed in the measured voltage. The corresponding change in the induced voltage in one of the detection coils can be estimated as

$$\Delta V = \frac{4\pi f \mu_0 N n I_e V}{D_e D_p} \tag{3.11}$$

where f is the frequency of the driving coil, μ_0 the permeability of free space N and n are the number of turns in the driving and detection coils and I_e is the current in the driving coil. The volume of the sample inside the coil is given by V and D_e and D_p are the diameters of the driving and detection coils [21]. Typical values of $f = 5029Hz$ and $I_e = 0.2mA$ are chosen such that δV exceeds any noise in the measurement to give a reasonable signal-to-noise ratio while still giving a good signal resolution. It is also important that the excitation field used produces a driving field that is below the critical field of the superconductor and does not significantly affect the superconducting transition temperature. The width of the superconducting transitions, obtained from the difference between the lower and upper onsets of the transitions, are used to estimate any uncertainty in T_c and the pressure. An example of a full high pressure magnetic susceptibility measurement is shown below in figure 3.23.

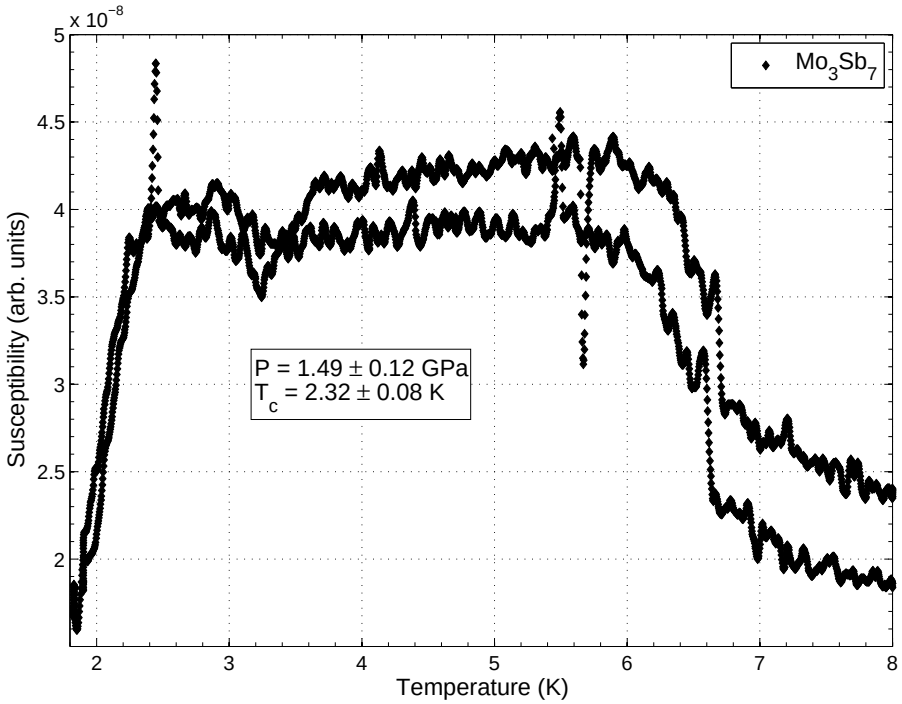

Figure 3.23: Magnetic susceptibility measurement of Mo_3Sb_7. The transition on the left is the superconducting transition of the Mo_3Sb_7 sample. The one on the right is the superconducting transition of the Pb manometer used to determine the pressure. The two different lines show the up and down temperature sweeps.

Chapter 4

Mo_3Sb_7

Few transition metal compounds with simple phase diagrams exhibit superconductivity. The two Mo-based compounds Mo_3Sb_7 and Mo_3Al_2C are interesting as recent studies have indicated that they show enhanced correlations and the possibility for unconventional superconductivity. Mo_3Sb_7 gives an opportunity to study a compound with a simple pressure-temperature phase diagram. An unconventional pairing mechanism is expected in Mo_3Al_2C due to its non-centrosymmetric structure. High pressure tuning of these compounds can help to uncover any interplay between structural, magnetic and superconducting properties which may help to understand the underlying mechanisms responsible for the unconventional superconductivity.

4.1 Introduction

Previous powder diffraction measurements performed on Mo_3Sb_7 [51] show that it crystallises in the cubic Ir_3Ge_7-type structure (space group: $Im\bar{3}m$) with lattice parameter $a = 9.571(5)$ Å. Figures 4.1a and 4.1c show the schematic view of the unit cell and the Mo octahedra chain at room temperature. The structure consists of corner sharing Mo octahedra forming Mo 'dumbbells' along the main three crystal directions. Mo_3Sb_7 is also reported to undergo a symmetry lowering structural transition from the cubic to a tetragonal lattice (space group: *I4/mmm*) with lattice parameters of $a = 9.555$ Å

and $c = 9.536$ Å at $T_s = 50$K, indicated by a sudden change in the lattice parameters below the phase transition temperature [52] as seen in Figure 4.2. The low temperature tetragonal crystal structure is shown in 4.1b. Modified bond lengths between Mo atoms for the tetragonal structure at 4K are shown along the c axis in figure 4.1d. Crystallographic information for the high and low temperature structures are summrised in table 4.1.

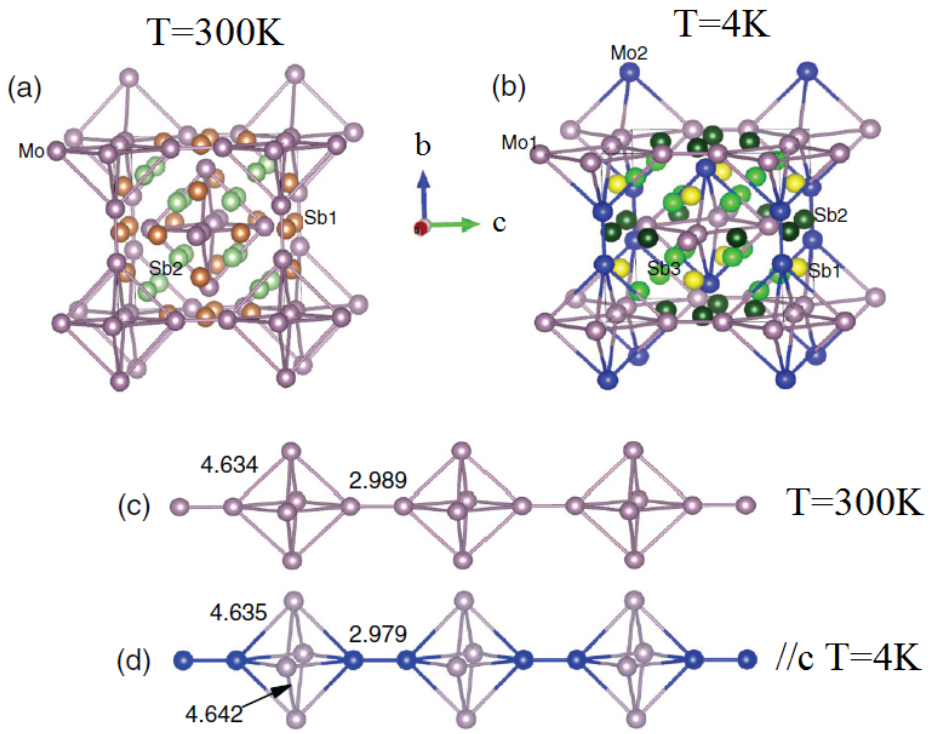

Figure 4.1: Crystal structure of Mo_3Sb_7 at (a) room temperature (cubic) and (b) 4K (tetragonal). The Mo octahedra are shown for (c) room temperature, (d) 4K along the c axis. Blue atoms show the second Mo site. Selected bond lengths are shown [53].

The structural phase transition is associated with the opening of spin gap induced by a partial Mo-Mo dimerisation along the z-axis, as indicated by a pronounced anomaly at the transition temperature in the heat capacity, and by a slight drop in magnetic susceptibility. A complete study of the physical properties of Mo_3Sb_7 was performed by Okabe *et al.* [52] and a superconducting transition temperature of $\sim$ 2.3K was found. Resistivity, magnetic susceptibility and heat capacity measurements are shown in Figure 4.3.

	Atom	Site	x	y	z
Im-3m	Mo1	12e	0.3441(3)	0	0
$a = 9.571(5)$ Å	Sb1	12d	0.250	0	0.5
	Sb2	16f	0.1627(1)	0.1627(1)	0.1627(1)
I4/mmm	Mo1	8i	0.3440(6)	0	0
$a = 9.555(8)$ Å	Mo2	4e	0	0	0.348(1)
$c = 9.536(8)$ Å	Sb1	4d	0	0.5	0.25
	Sb2	8j	0.2463(7)	0.5	0
	Sb3	16m	0.1627(2)	0.1627(2)	0.1625(4)

Table 4.1: Structural parameters of Mo_3Sb_7 for both the cubic and low temperature tetragonal units cells at ambient pressure.

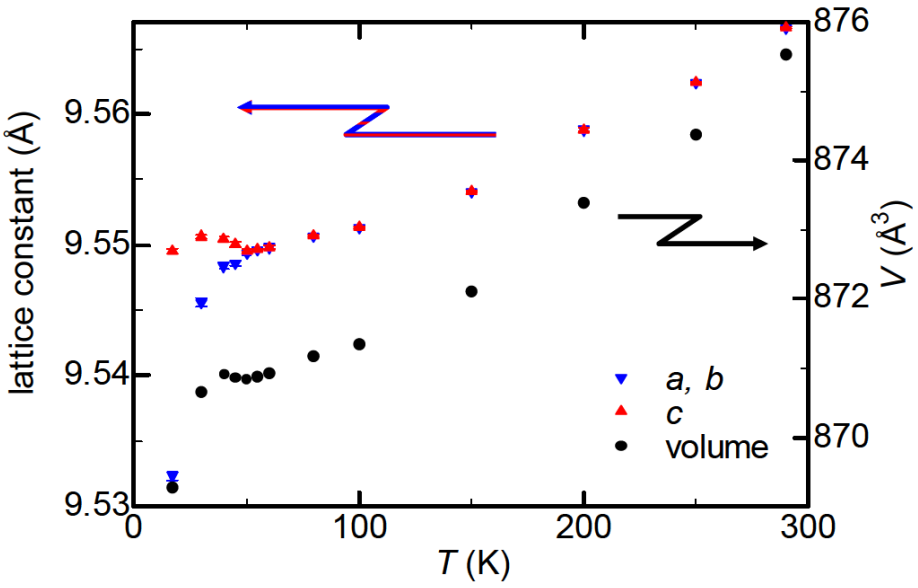

Figure 4.2: Lattice parameters of Mo_3Sb_7 as a function of temperature obtained from x-ray powder diffraction measurements [52].

High pressure resistivity measurements were performed by Tran *et. al.* up to 2.2 GPa [54]. At temperatures above around 7K Mo_3Sb_7 was found to exhibit a metallic behaviour without any significant changes with increasing pressure. The superconducting transition temperature was found to increase with pressure to a maximum of $T_c = 2.37$K at the maximum pressure in this study, as can be seen earlier in figure 1.2. Perhaps more importantly though a new phase transition was observed as seen by a sharp jump

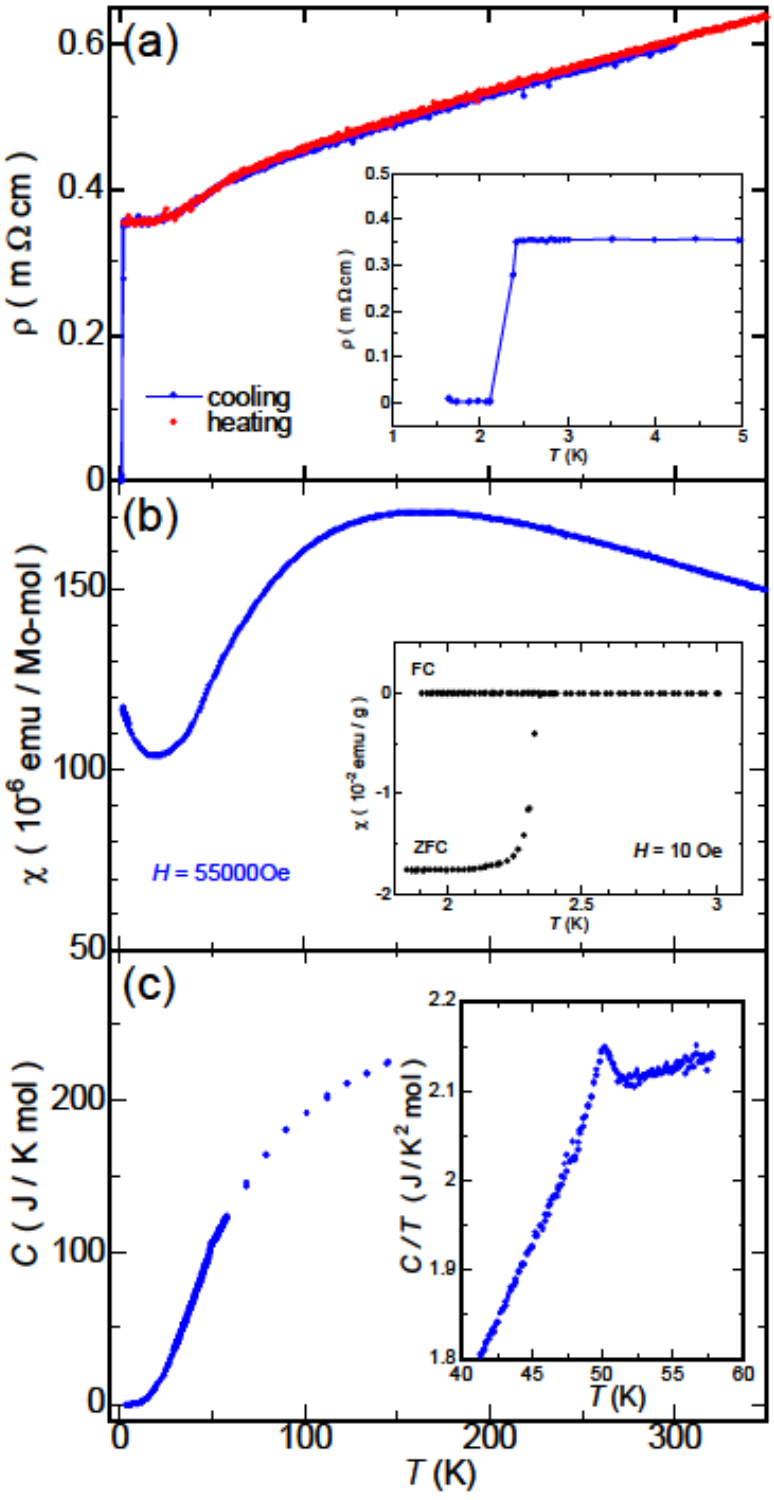

Figure 4.3: Temperature dependance of the resistivity (a), magnetic susceptibility (b) and (c) specific heat of Mo_3Sb_7 [52]. The superconducting transition is shown as insets in the resistivity and magetic suscepibility plots show the superconducting transition at 2.3K. The inset in the specific heat shows an anomaly at 50K from the structural transition.

in the resistivity at 0.45 GPa at $T_{SDW} = 6.6$K, as can be seen in figure 4.4. This upturn in the resistivity has been ascribed to the onset of a spin-density-wave (SDW) and has been attributed to the opening of an energy gap at points of the Fermi surface. Magnetisation of Mo_3Sb_7 was also measured by Tran *et. al.* [54] up to 0.02T at a pressure of 0.7 GPa to confirm the magnetic origin of the transition at T_{SDW}. The increasing field was found to suppress T_{SDW} as is typical with antiferromagnetic systems.

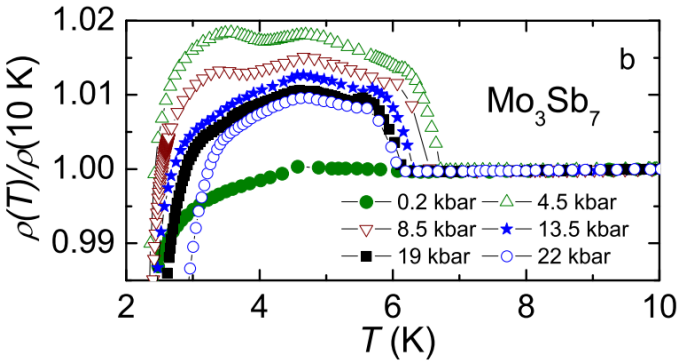

Figure 4.4: High pressure resistivity data for Mo_3Sb_7 normalised at 10K. The superconducting transition is seen as a down turn in resisitvity on the left and the SDW transition as the sudden upturen near 7K on the right.

4.2 Sample Characterisation

Polycrystalline samples of Mo_3Sb_7 were prepared by V. H. Tran *et. al.* from high purity Mo and Sb powders by solid state reaction [51]. The crystal structure of samples used here was checked by x-ray powder diffraction, figure 4.5. Refinement of this pattern using the cubic structure yielded a lattice parameter of $a = 9.572 \pm 0.001$ Å and unit cell volume $V = 877.02 \pm 0.05$ Å which is in good agreement with those from literature [52] [55].

Figure 4.6a shows a measurement of the zero pressure resistivity of Mo_3Sb_7 indicating an onset of superconductivity at a temperature of $T_c = 2.25$K which agrees well with

values obtained by previous measurements [52]. The residual resistivity $\rho_0 = 130\mu\Omega$-cm obtained from this measurement is higher than values reported in literature [51] [55]. An uncertainty in the size of the sample measured could account for this difference. Magnetic susceptibility measurements confirm the superconducting transition at the same temperature as obtained from the resistivity measurements (Figure 4.6b).

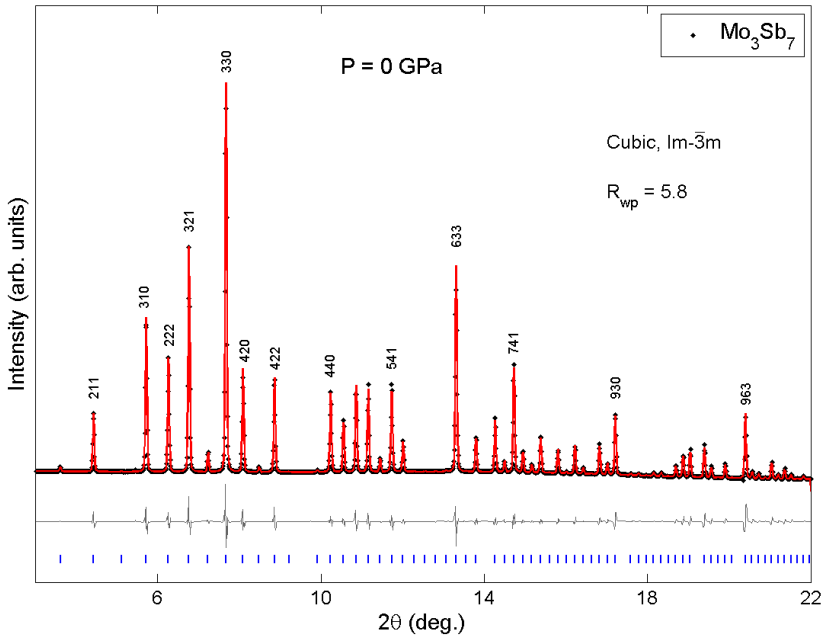

Figure 4.5: Le Bail refinement of the ambient pressure powder diffraction pattern, 41 keV, of Mo_3Sb_7 comfirming the cubic Im-$\bar{3}$m structure.

4.3 High Pressure X-ray Powder Diffraction of Mo_3Sb_7

It was interesting to test whether the apparent simple magnetic pressure-temperature phase diagram of Mo_3Sb_7 is complicated by any structural transitions. A Holzapfel-Syassen cell was loaded with a small $\sim$50μm piece of polycrystalline sample and methanol-ethanol used as a pressure transmitting medium. Pressure in the cell was measured via the ruby fluorescence technique. Refinement of the diffraction pattern for the first pressure, $P = 0.23$ GPa, produced a lattice parameters of $a = 9.751$ Å for

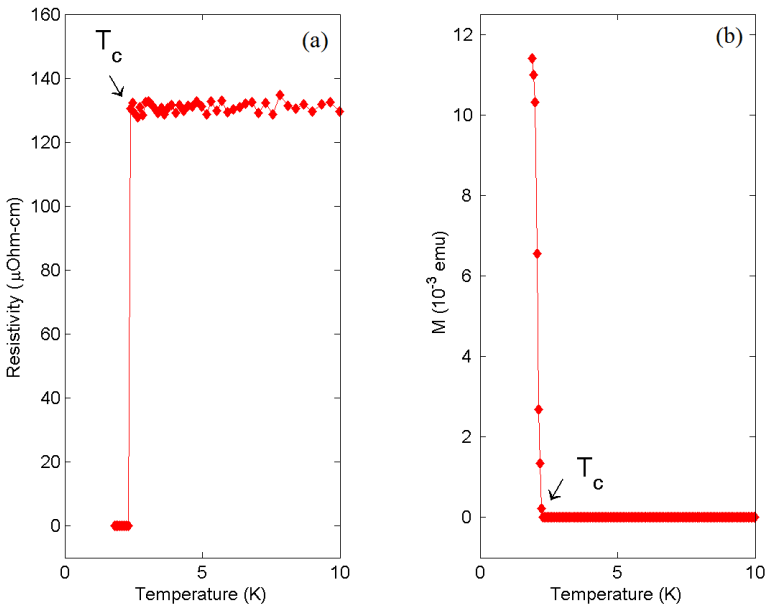

Figure 4.6: Resistivity and magnetic susceptibility data of Mo_3Sb_7 at ambient pressure. A superconducting transition temperature of $T_c = 2.25$K is found. No feature from the spin density wave is seen in the resistivity at zero pressure.

Mo_3Sb_7. As this value is larger than that obtained for the ambient pressure measurement it was concluded that the sample was not positioned in the same place as the silicon standard and therefore the sample to distance was incorrect. A new detector distance was obtained by estimating the lattice parameter for Mo_3Sb_7 for $P = 0.23$ GPa using the initial data obtained using the incorrect sample to detector distance. The detector distance was then modified such that the 2θ position of the strongest peak (330) in the integrated pattern of the $P = 0.23$ GPa pattern agreed with the calculated position.

Diffraction patterns were collected up to a maximum pressure of 13.6 GPa, where the gasket hole became unstable and started to increase in size, thus risking the gasket collapsing and damaging the anvils. Each diffraction pattern shown in figure 4.7 has been normalised to the (330) peak. Above about 10 GPa the peaks of the powder diffraction patterns start to become broader. Some of this broadening could be due to a drop in the hydrostaticity of the methanol-ethanol pressure transmitting medium

as it solidifies above 10.5 GPa [22]. A further possible reason for the broadening is from the sample bridging the diamond anvils as the gasket became thinner throughout the experiment. Differing peak intensities between patterns may arise from less than perfect powder averaging throughout the polycrystalline sample. The sample was not rocked throughout the data collection as the sample was not placed at the centre of rotation. Peak positions are shifted to higher values in 2θ with increasing pressure as the lattice parameters decreases.

X-ray powder diffraction patterns with increasing pressure are shown in figure 4.7. In addition to refining the data with the cubic structure all data were refined in the low temperature tetragonal structure as well. The Le bail refinement of the $P = 0.23$ GPa pattern using both the cubic and tetragonal structures are shown in figure 4.8. Refinements of the $P = 5.69$ GPa and $P = 13.59$ GPa patterns using the cubic structure are shown in figure 4.9. The peak splitting of the [330] peak from a transition from cubic to tetragonal structure was estimated to be a little as 0.03° which would be very hard to observe with the resolution of patterns obtained. Therefore no peak splitting was seen in the diffraction patterns in Figures 4.8 and 4.9 as would be expected for a tetragonal structure. However, the pressure-volume data for Mo_3Sb_7, shown later in figure 4.13, shows no significant deviation from a fitted Birch-Murnaghan equation of state and it is therefore concluded that Mo_3Sb_7 remains stable in the zero pressure cubic Im-3m structure under pressure. As the measurements have a large background a better indication of the quality of fit of the refinements is given by R_{Bragg}, equation 3.10, which are lower for the cubic fits supporting the result that Mo_3Sb_7 remains in the cubic structure.

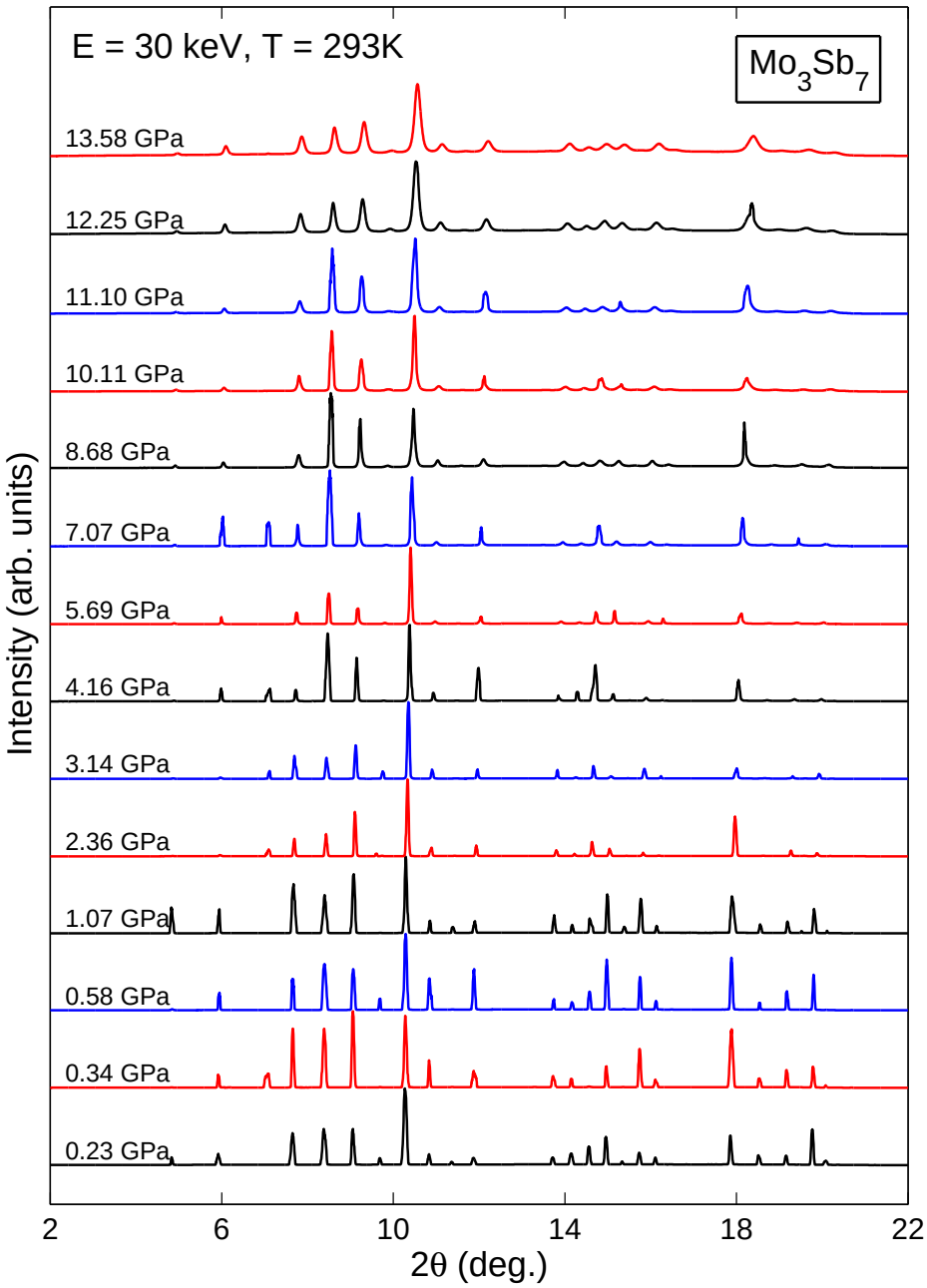

Figure 4.7: X-ray powder diffraction patterns of Mo_3Sb_7 with increasing pressure at 300K. The structure is found to be stable up to the highest pressure obtained. Significant broadening is observed above about 10 GPa due to both anvils coming into contact with the sample.

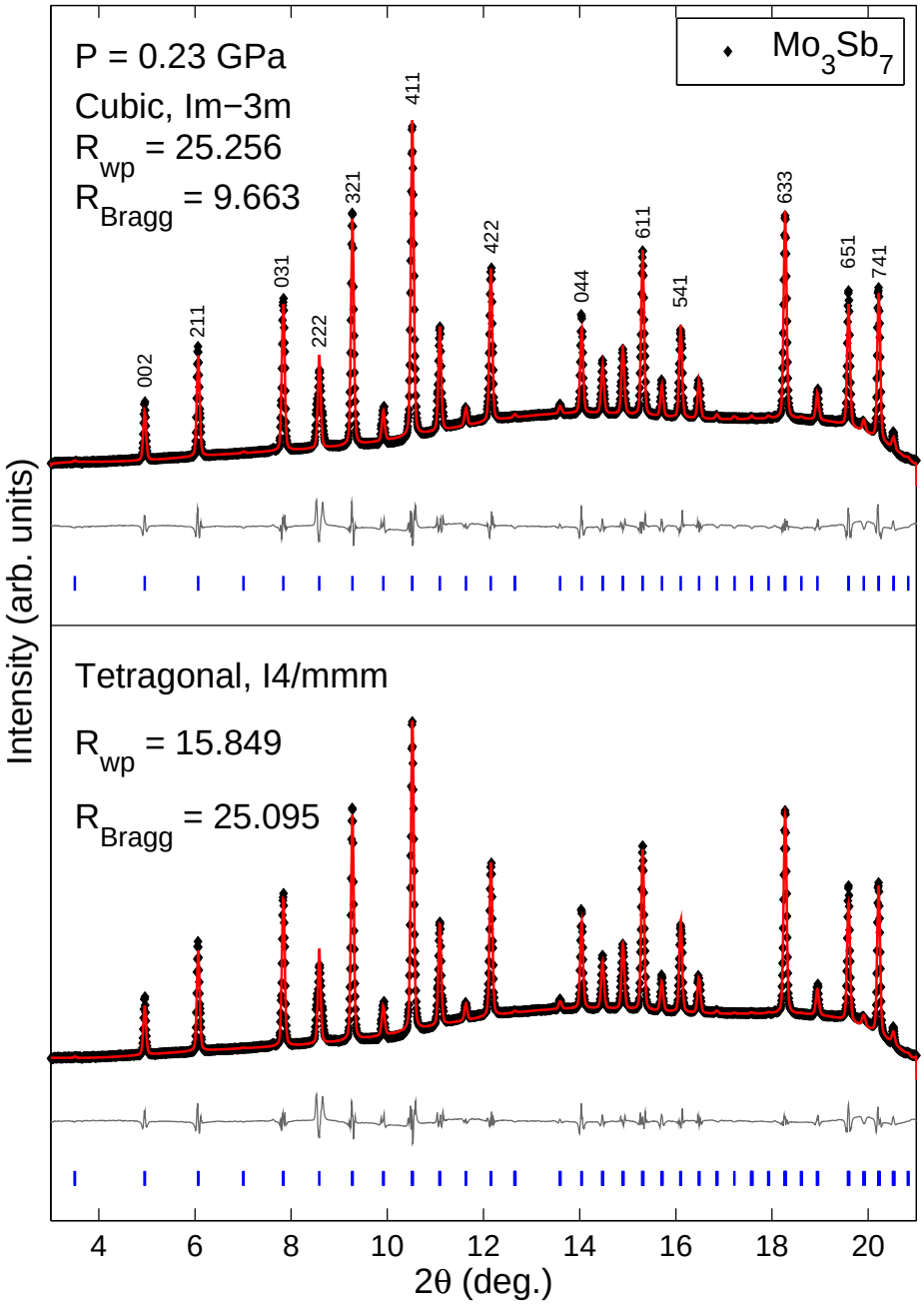

Figure 4.8: Le Bail refinements of the x-ray diffraction pattern of Mo_3Sb_7 at 0.23 GPa using both the room temperature cubic structure (top) and the low temperature tetragonal (bottom) structure. The much lower value for R_{Bragg} for the cubic refinement indicates the correct structure.

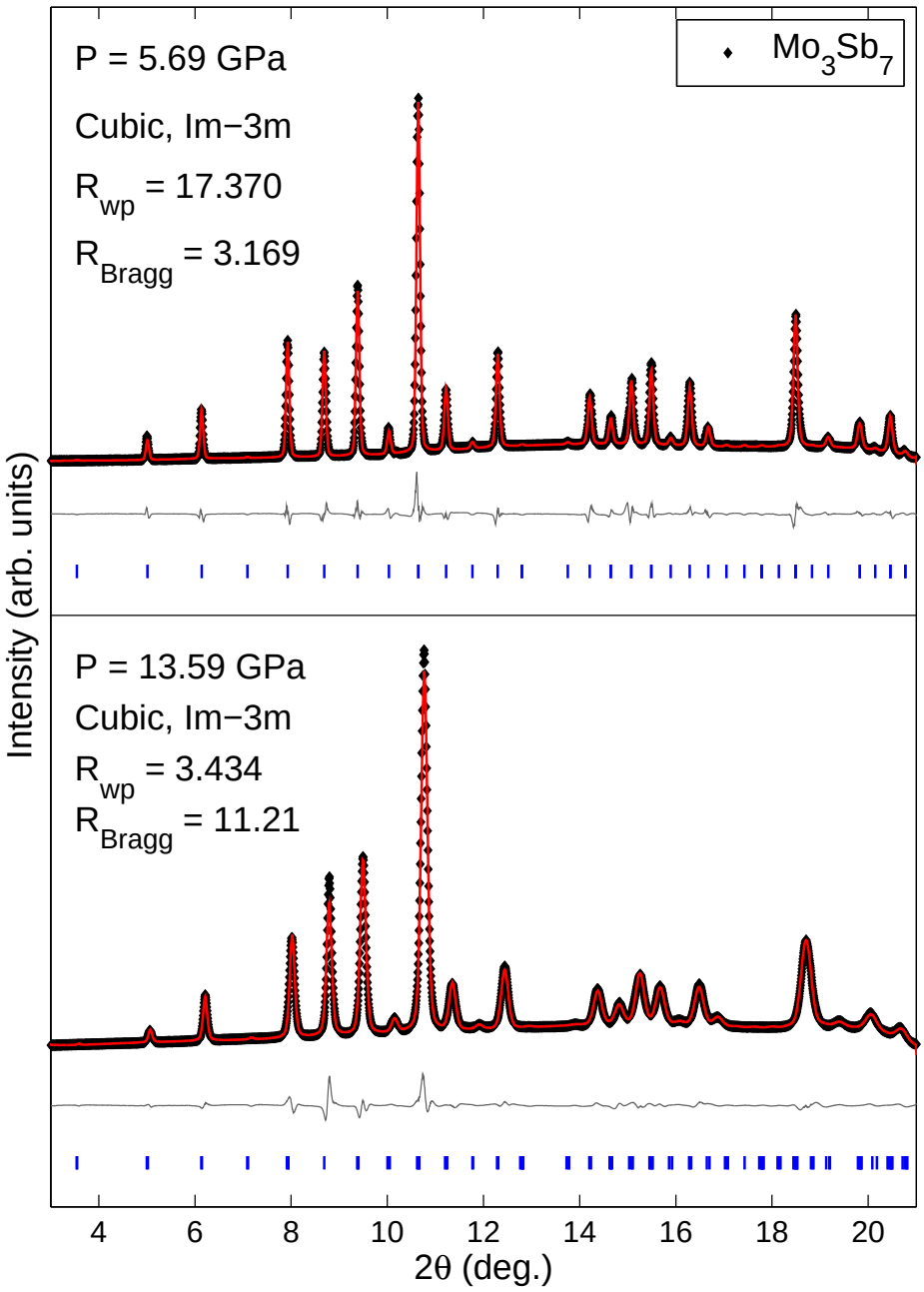

Figure 4.9: Le Bail refinements of Mo_3Sb_7 at a pressure of 5.69 GPa (top) and 13.50 GPa (bottom) using the cubic structure.

4.4 Pressure Dependence of T_c in Mo_3Sb_7

The superconducting transition temperature was taken to be the onset of the transition. The onset T_c was determined by taking the intercept of two straight lines fitted against the data before and during the transition (Figure 4.10). Measurements of the magnetic susceptibility of Mo_3Sb_7 were taken up to a maximum pressure of 6.2 GPa, figure 4.11. The cell failed after attempting to increase the pressure further. The filling factors of the Pb manometer and sample micro-coils was estimated to be about 40% and 90% respectively. From the magnitudes of the signals and the filling factors it appears that Mo_3Sb_7 has a failry high superconducting fraction. The onset transition temperatures are indicated by the arrows in figure 4.11. The superconducting transition of Mo_3Sb_7 was found to increase with increasing pressure.

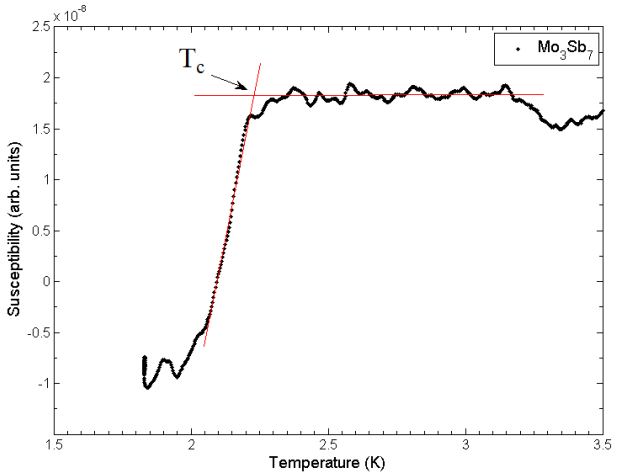

Figure 4.10: Plot of a magnetic susceptibility measurement of Mo_3Sb_7 at $P = 2.6$ GPa showing how the superconcuding transition temperature is determined. T_c is taken to be the intersect of the two lines fitted to the data during and up to the transition.

4.5 Discussion

The pressure-temperature phase diagram, figure 4.12, shows that the superconducting transition temperature of Mo_3Sb_7 is enhanced on the application of pressure at a rate of about 0.075 K/GPa up to a maximum of 2.63K at 6.21 GPa. Previous measurements

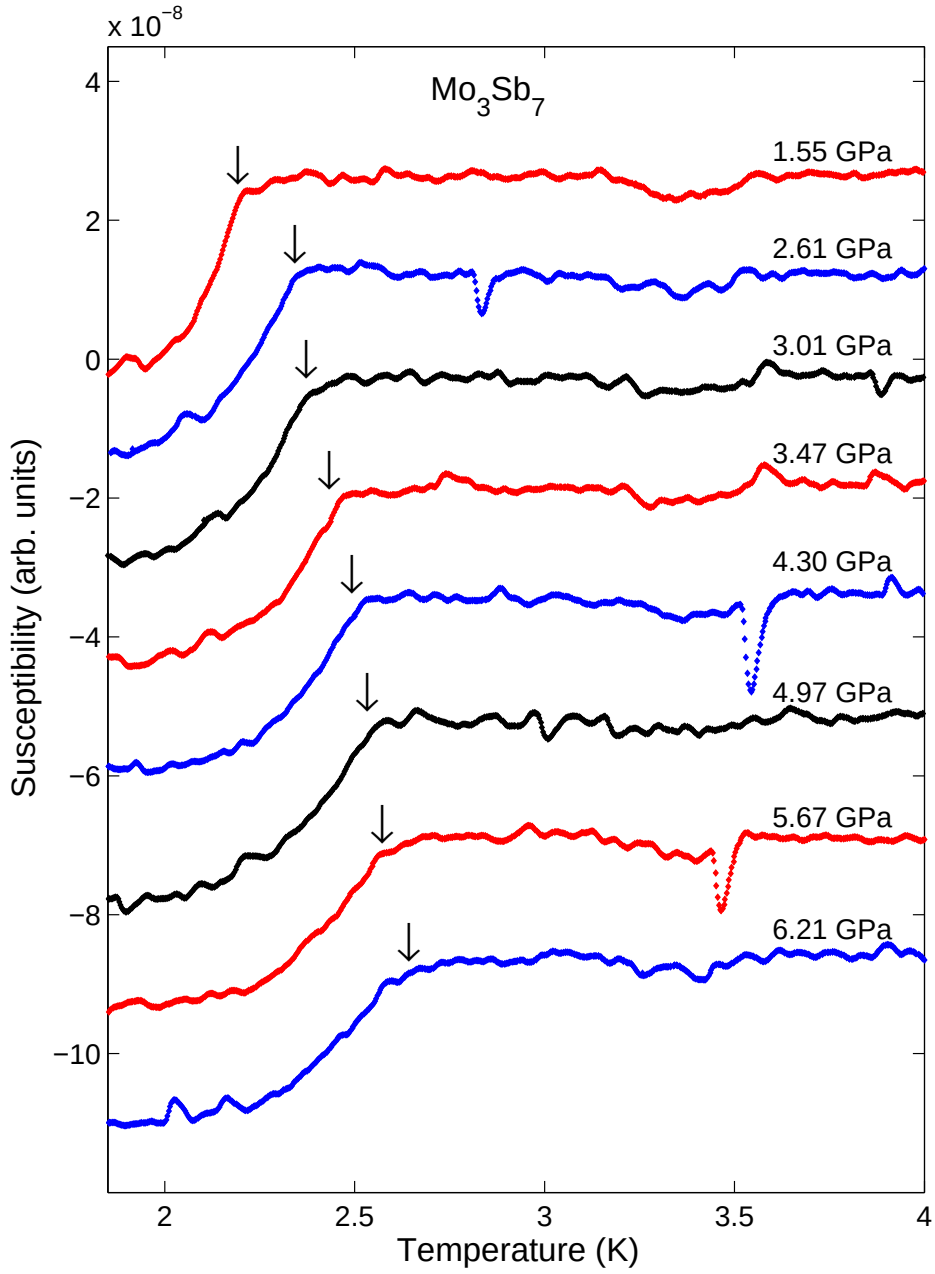

Figure 4.11: Magnetic susceptibility measurements showing the onset of superconductivity in Mo_3Sb_7 with increasing pressure. The original data has been smoothed to remove any sharp noise features. T_c is seen to increase with pressure. The sharp spikes in some of the data are noise from self made solder contacts and vibrations.

performed by Tran *et. al.* [54] are also shown on the phase diagram and agree fairly well with the data measured here. There is a small difference of about 0.1K in the value of T_c at zero pressure of the sample measured here and that measured previously by Tran *et al.*. This difference could be due a slight difference in the homogeneity throughout the sample, to which unconventional superconductors respond very sensitively to. The

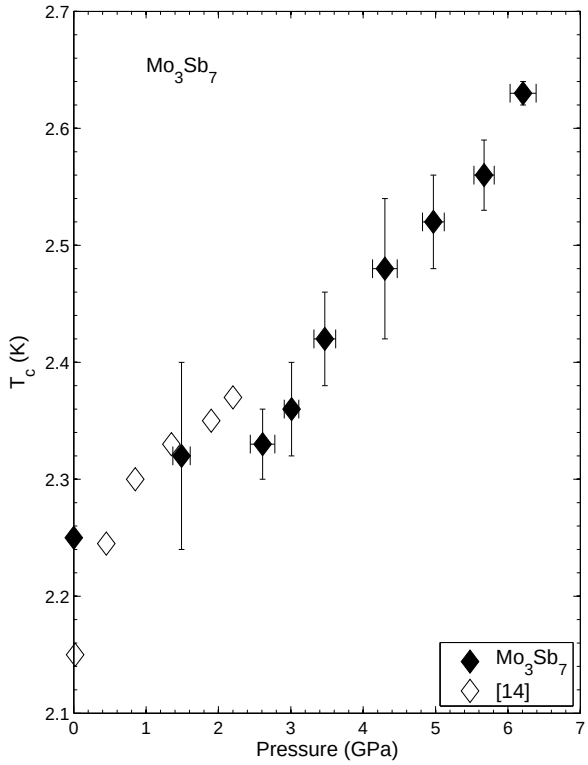

Figure 4.12: Superconducting phase diagram of Mo_3Sb_7 under applied pressure. Solid diamonds showing data collected in this work and open diamonds represent data from literature [54].

difference in the initial slopes of the data measured by Tran and here is probably due to the different measurements used, resistivity and magnetic susceptibility. It is also not knwon how T_C was estimated in the previous measurements performed by Tran which may also account for the discrepancy between the published data and the result here. The enhancement of superconductivity could be due to an increase of density of states at the Fermi surface and increased phonon frequency as the lattice parameter reduces. The decreasing T_{SDW} with increasing pressure along with the increasing T_c also puts Mo_3Sb_7 as a candidate for magnetically mediated superconductivity. If the behaviour of the magnetism and superconductivity remains linear with increasing pressure a maximum value for T_c of about 3.1K at around 13 GPa can be estimated.

The lattice parameters obtained from refinement of the Mo_3Sb_7 x-ray powder diffraction data were both plotted against pressure and each fitted with a Birch-Murnaghan type

equation of state to obtain a zero pressure volume, bulk modulus and its pressure derivative. The values obtained can be found in table 4.2. Values for the zero pressure unit cell volume, bulk modulus and it's pressure derivative were obtained for the cubic structure refinement data and is shown in table 4.2. The cubic structure of Mo_3Sb_7 was found to be stable up to around 14 GPa, the highest pressure reached in this work. The lack of a structural transition at room temperature means that the slope of the low temperature structural transition with increasing pressure will be negative. A speculative pressure-temperature phase diagram for Mo_3Sb_7 is shown in Figure 4.14. It appears that the pressure induced spin-density-wave phase is due to the structural transition. The sudden change in slope of T_c with increasing pressure could also be explained by the structural transition.

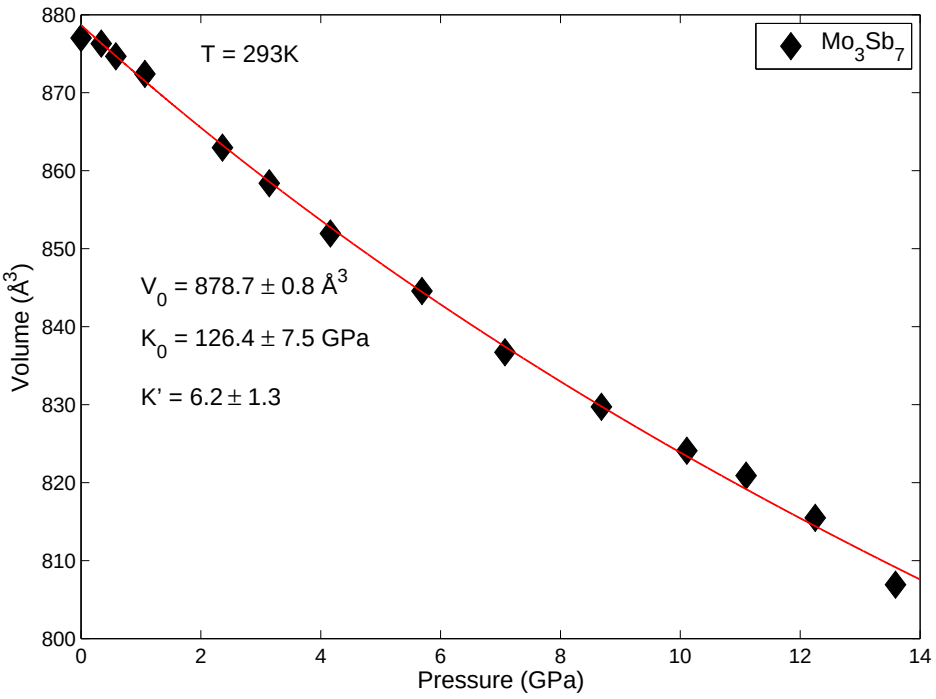

Figure 4.13: Evolution of the structural parameters of Mo_3Sb_7 with increasing pressure obtained from Le Bail refinements for both cubic, solid diamonds, and tetragonal, open diamonds, structures. The P-V data obtained from the cubic structure has been fitted with a Birch-Murnaghan type equation of state, red line, yielding values for the bulk modulus and pressure derivative of $K_0 = 126.4 \pm 7.5$ GPa and $K_0' = 6.2 \pm 1.3$.

Mo_3Sb_7	
V_0 (Å^3)	878.7 ± 0.8
K_0 (GPa)	126.4 ± 7.5
K_0'	6.2 ± 1.3

Table 4.2: Zero pressure volume, bulk modulus and pressure derivative values from Birch-Murnaghan equation of state fit to the P-V data for Mo_3Sb_7

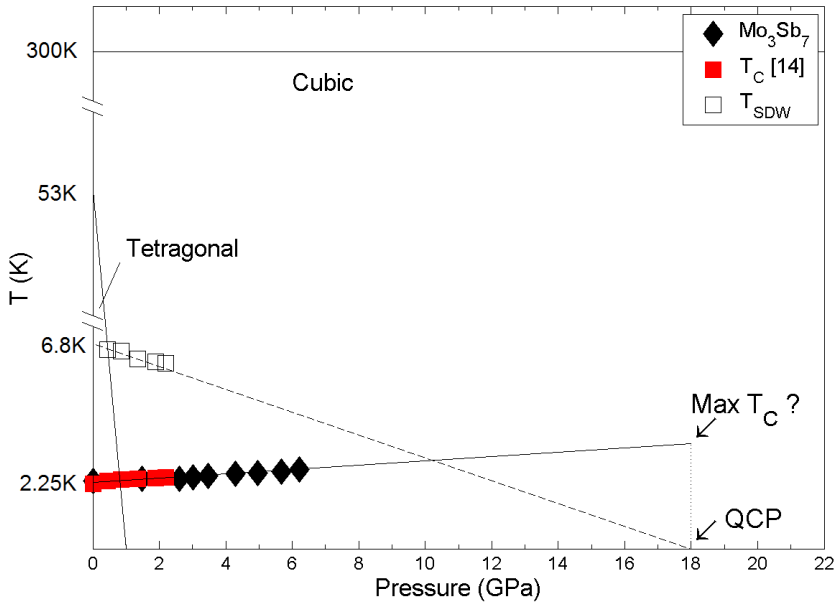

Figure 4.14: Speculative pressure-temperature phase diagram of Mo_3Sb_7.

Chapter 5

Mo_3Al_2C

5.1 Introduction

Studies of metal carbide superconductors have shown fairly high superconducting transition temperatures. Some of these compounds, including Mo_3Al_2C, lack a centre of inversion symmetry in their crystal structures. The noncentrosymmetric structure leads to a coupling of the electron momentum and spin due to the Rashba effect. The antisymmetric spin orbit coupling splits the Fermi surface and removes the spin degeneracy of the electrons initiating a mixture of spin-singlets and spin-triplets in the superconducting condensate. Studies of the pairing in this type of system originated with the discovery of superconductivity in the heavy-fermion $CePt_3Si$ [56]. Mo_3Al_2C gives an interesting example to study a noncentrosymmteric superconductor under pressure.

Mo_3Al_2C adopts the cubic non-centrosymmetric type structure (space group: $P4_132$) and has a lattice parameter of $a = 6.683$ Å [57]. A schematic of the unit cell can be found in the introduction in figure 1.3. Further structural information can be found in table 5.1. A superconducting transition temperature of $T_c = 9$K is found in Mo_3Al_2C [57], see figure 5.1. Resistivity under pressure has been previously performed up to 25 kbar by Bauer *et. al.* from which they found an increase in T_c which tended to saturate at the higher pressures (Figure 5.1). They also found that the application of pressure

did not change the normal-state region of the resistivity and thus the enhancement in T_c was concluded to be due to a slight increase in the density of states at E_F [11].

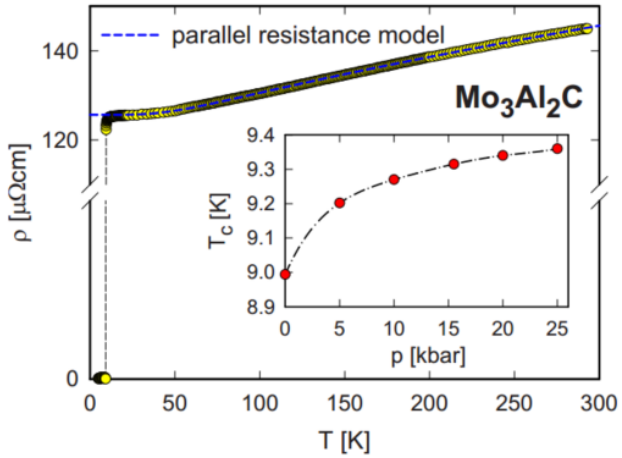

Figure 5.1: Resistivity of polycrystalline Mo_3Al_2C up to around 300K showing a superconducting transition temperature of 9K. *Inset*: Evolution of T_c with pressure up to 25kbar [11].

Mo_3Al_2C				
Temperature:	Room Temperature			
Space group:	$P4_132$			
a (Å)	6.863			
Atom	Site	x	y	z
Mo	12d	0.1250	0.2025(2)	0.4525(2)
Al	8c	0.068(1)	0.068(1)	0.068(1)
C	4a	0.3750	0.3750	0.3750

Table 5.1: Structural parameters for the Mo_3Al_2C at ambient pressure and room temperature.

5.2 Sample Characterisation

Polycrystalline Mo_3Al_2C samples were prepared from an elemental powder mixture that was compacted before being reacted for 24 hours at 1500° in a high vacuum furnace, including an intermediate grinding and compacting step [11]. The material was ground for a final time before being pressed into pellets. A zero pressure powder diffraction pattern was obtained. Refinement of this zero pressure powder diffraction pattern of

Mo_3Al_2C, figure 5.2 gives a lattice parameter of $a = 6.863 \pm 0.001$Å which agrees with literature values within calculated errors. [11]. Zero pressure resistivity and magnetic susceptibility measurements, figure 5.3, show a T_c for Mo_3Al_2C of 9K, as was obtained by Bauer [11].

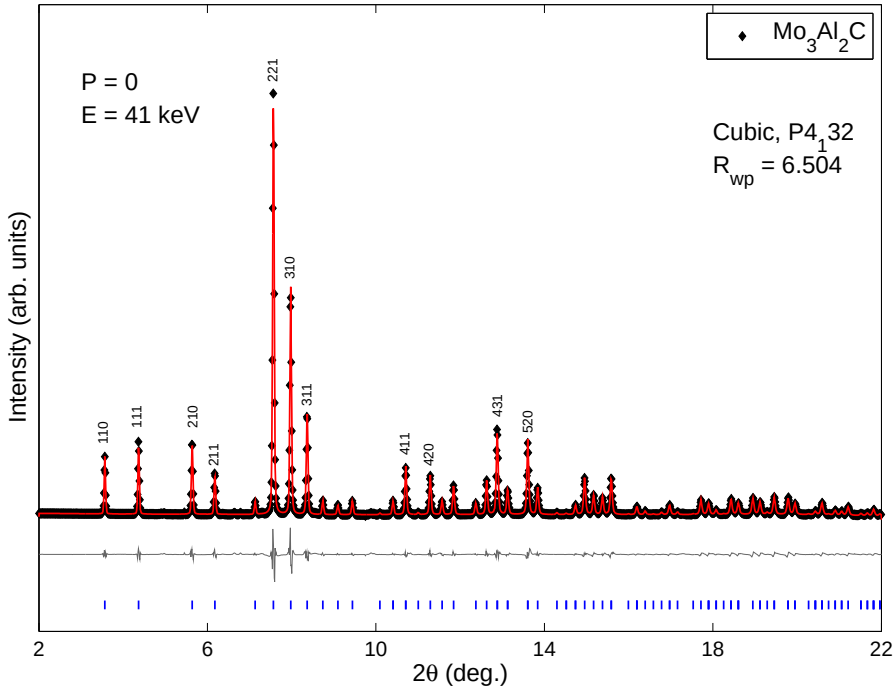

Figure 5.2: Le Bail refinement of the powder diffraction pattern, energy 41 keV, of Mo_3Al_2C at ambient pressure confirming the cubic $P4_132$ structure. The refinement yields a lattice parameter $a = 6.863$Å in good agreement with previous studies [11].

5.3 High Pressure X-ray powder Diffraction of Mo_3Al_2C

Three separate high pressure x-ray powder diffraction measurements of Mo_3Al_2C were carried using a different pressure transmitting medium for each loading. Experimental information for each pressure medium is summarised below in table 5.2. Measurements of sample 2 where performed using a new set of micro-focusing mirrors on a new previously unused stage of the I15 beamline. The pressure in each cell loading was

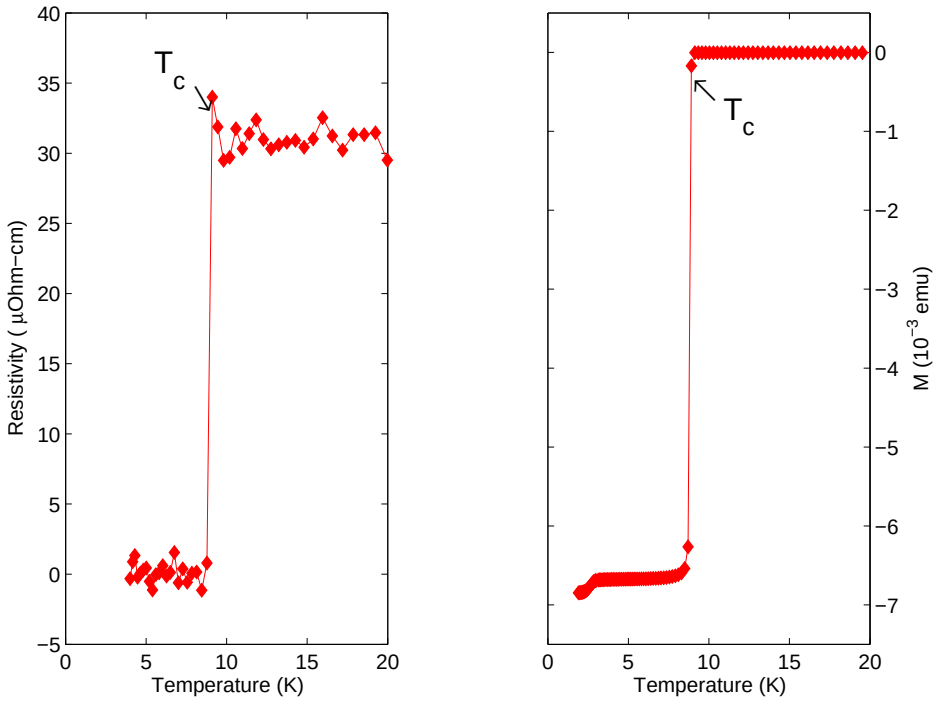

Figure 5.3: Resistivity and magnetic susceptibility measurements at ambient pressure of Mo_3Al_2C showing a superconducting transition temperature of $T_c = 9.0$K

determined via the ruby fluorescence technique.

	Beam Energy	Beam Diameter	Pressure Medium	P_{Max} of DAC
Sample 1	36.7/40 keV	50μm	Silicon Oil	8.5 GPa
Sample 2	41.8 keV	$\sim 7\mu$m	Methanol-ethanol	30.2 GPa
Sample 3	30 keV	20μm	Helium	14.6 GPa

Table 5.2: Experimental parameters for x-ray powder diffraction for the three different high pressure runs.

X-ray powder diffraction measurements of sample 1 were taken up to a maximum pressure of 8.5 GPa in first run using silicon oil as a pressure transmitting medium. The first three patterns were collected using an energy of $E = 36.7$ keV. The remaining patterns were collected using 40 keV. All the data is shown in figures 5.4. All patterns have been normalised to the [221] peak. Very little peak broadening is seen in the higher pressure patterns indicating a good hydrostatic pressure environment in the sample chamber. Le Bail refinements for both low and high pressure measurements

taken from the first run, figures 5.5 and 5.6, confirm that the structure remains stable to the maximum pressure reached.

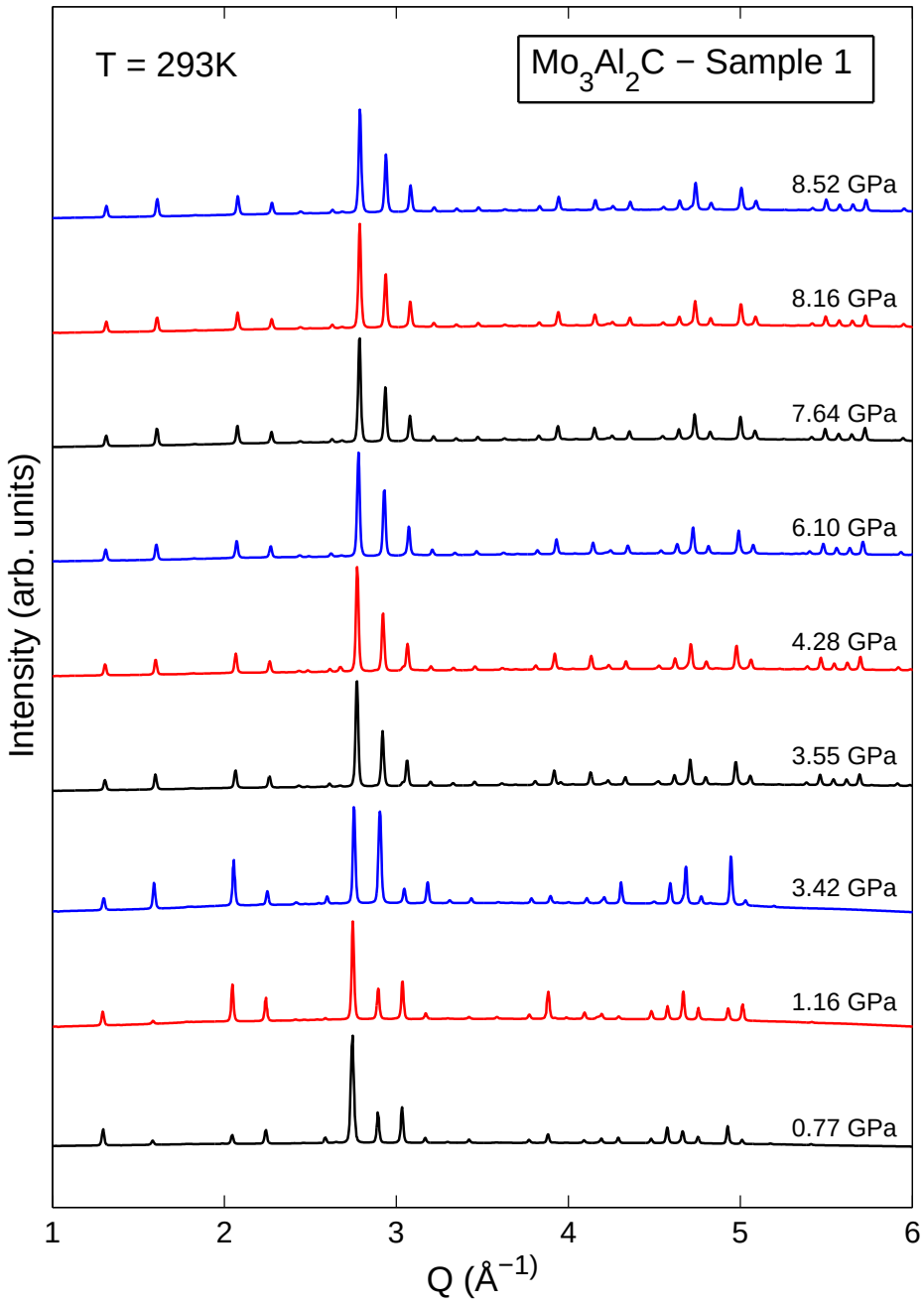

Figure 5.4: Powder diffraction patterns of Mo_3Al_2C with increasing pressure. Data were taken in a silicon oil pressure transmitting medium. All data has been normalised to the [221] peak.

X-ray powder diffraction patterns of sample 2, loaded with the methanol-ethanol pressure medium, were obtained up to a maximum pressure of 30.17 GPa and are shown in

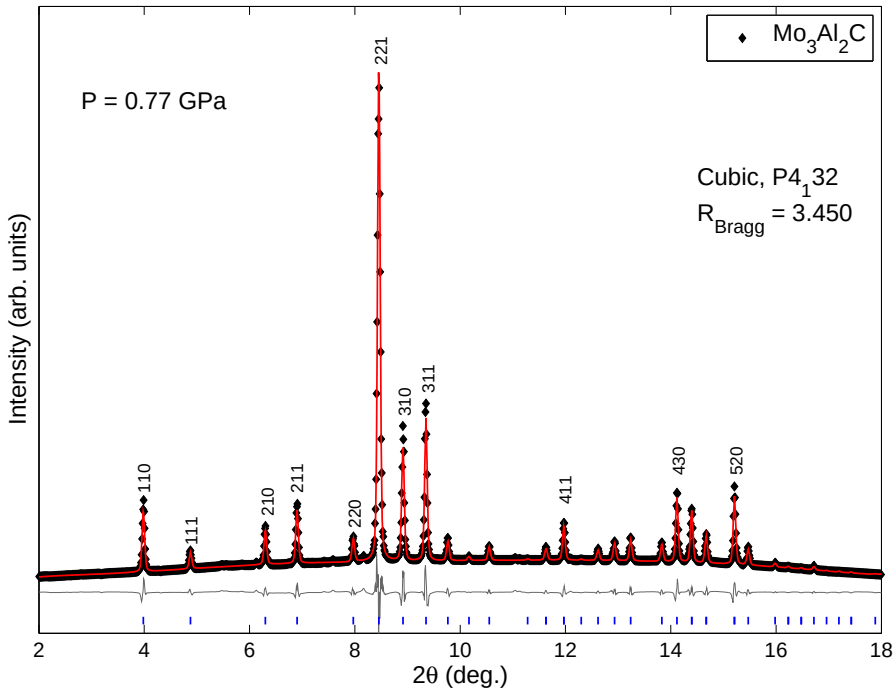

Figure 5.5: Le Bail refinement to the Mo_3Al_2C data collected at 0.77 GPa using 36.7 keV x-rays. The pressure medium used was silicon oil. The low value $R_{Bragg} = 3.450$ indicates a good fit to the data confirming the $P4_132$ structure.

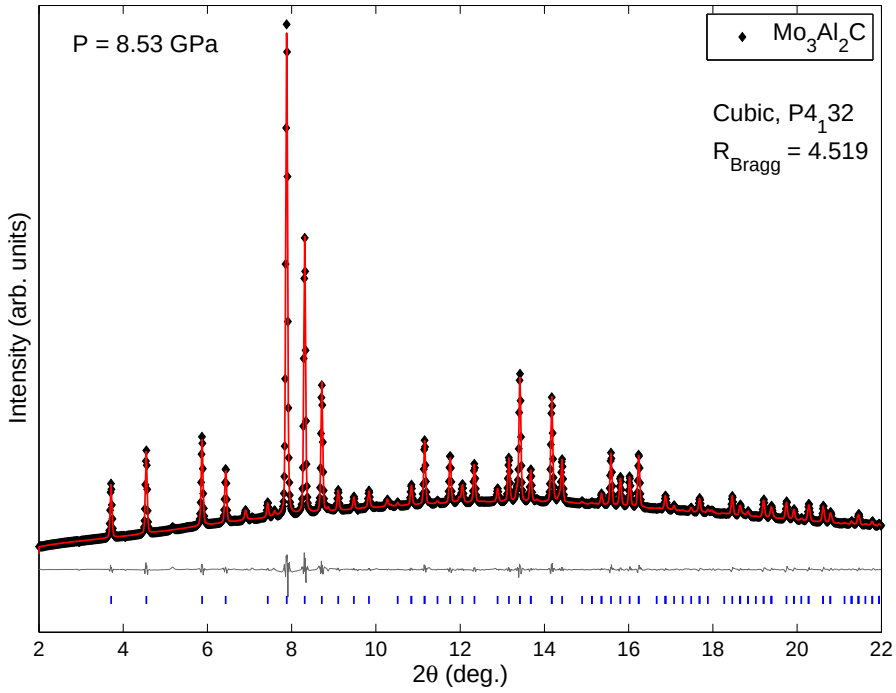

Figure 5.6: Le Bail refinement of the high pressure Mo_3Al_2C data, $P = 8.53$ GPa, measured in the silicon oil pressure medium, using 40 keV x-rays. The initial structure remains stable up to this pressure.

figures 5.7 and 5.8. All the patterns have been normalised to the (221) peak and

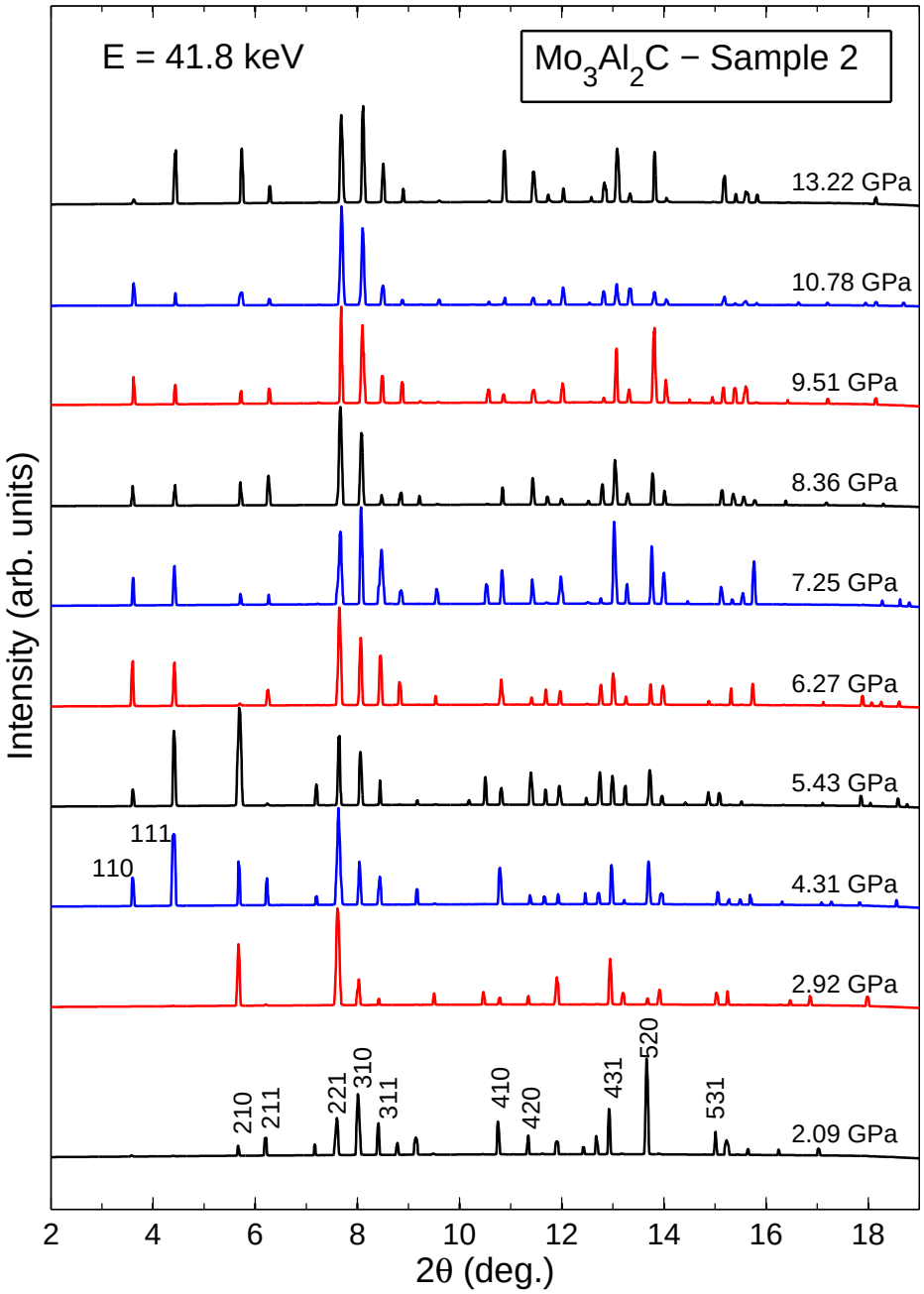

Figure 5.7: X-ray powder diffraction patterns of Mo_3Al_2C, using a beam energy of 41.8 keV, with increasing pressure up to 13.2 GPa. All pattern are in the low pressure $P4_132$ structure. Methanol-ethanol was used as the pressure transmitting medium. The peaks vary in intensity between pattern due to the large crystallite size in the polycrystalline sample and the small beam diameter of 7μm and causes the 110 and 111 peaks to be absent from the first two pressure patterns.

plotted to 25% the (221) peak intensity to enlarge the smaller peaks. The R1 and R2 lines in the ruby fluorescence spectra and the sharp well defined peaks of all the

diffraction patterns show that the methanol-ethanol pressure transmitting medium remains hydrostatic even up to the very high pressure of 30 GPa. There are significant differences in some peak intensities between patterns which may be accounted for by the small beam diameter of 7μm and the larger crystallite size in the Mo_3Al_2C sample which would lead to an uneven distribution of crystallite orientation. All patterns appear to show the same cubic $P4_132$ structure remains stable up to 13.2 GPa. The lattice parameters obtained from the refinements of the data are lower than those obtained from the first experiment. During this experiment the sample was positioned in the incorrect position with respect to the silicon standard. The sample-to-detector distance used for integrating the data was modified, as for the Mo_3Sb_7 experiment, so that the patterns agree with the other data. The lattice parameters obtained from Le Bail refinements of all the patterns using the zero pressure structure indicate that the sample undergoes a structural transition near 13 GPa. Refinements of the 2.09 and 13.2 GPa patterns are shown in figures 5.9 and 5.10 respectively. The poor refinement of the $P = 15.8$ GPa data, figure 5.11, along with an increase in the lattice parameters above this pressure indicates that a structural transition occurs between 13.2 and 15.8 GPa.

Data from the sample 3, loaded with the helium pressure medium, is shown in figure 5.12, in which all data have been normalised to the (221) peak. The much stronger intensity of the (221) and (310) peaks indicate a very strong preferential orientation in these directions. Figures 5.13 and 5.14 show refinements of the low pressure, $P = 4.14$ GPa, and high pressure, $P = 14.63$ GPa. The ambient pressure structure remains stable to 14.6 GPa. The sharpness of the ruby fluorescence peaks indicates that the helium pressure transmitting medium produces very hydrostatic conditions.

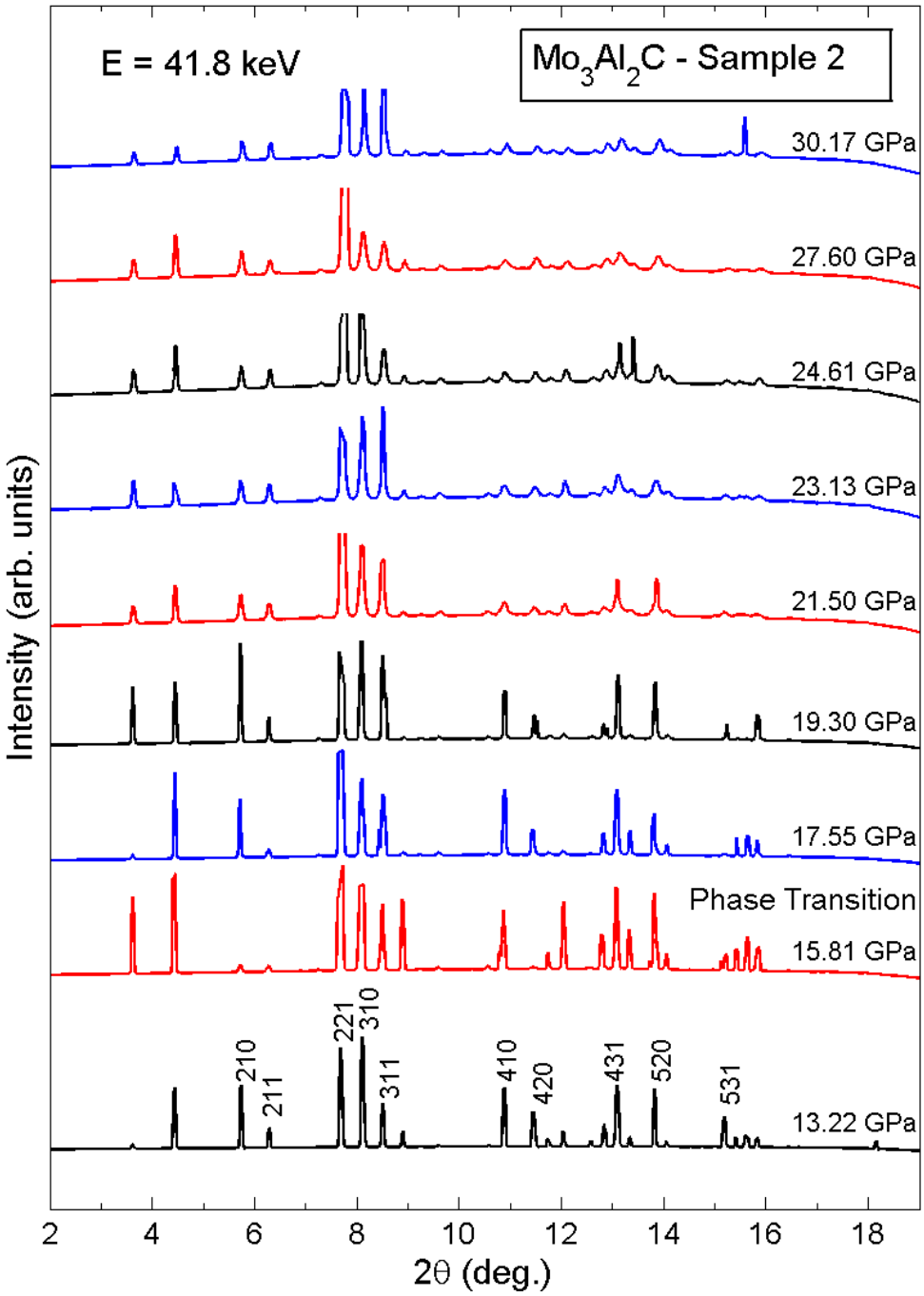

Figure 5.8: X-ray powder diffraction patterns, 41.8 keV, of the sample 2 of Mo_3Al_2C. Above 13 GPa the sample undergoes a structural transition into a new structure. As for the lower pressure patterns the peaks intensities vary due to crystallite size and the very small beam diameter. The patterns above the structural transition has been plotted to about 25% of the (221) peak intensity to enlarge the smaller peaks.

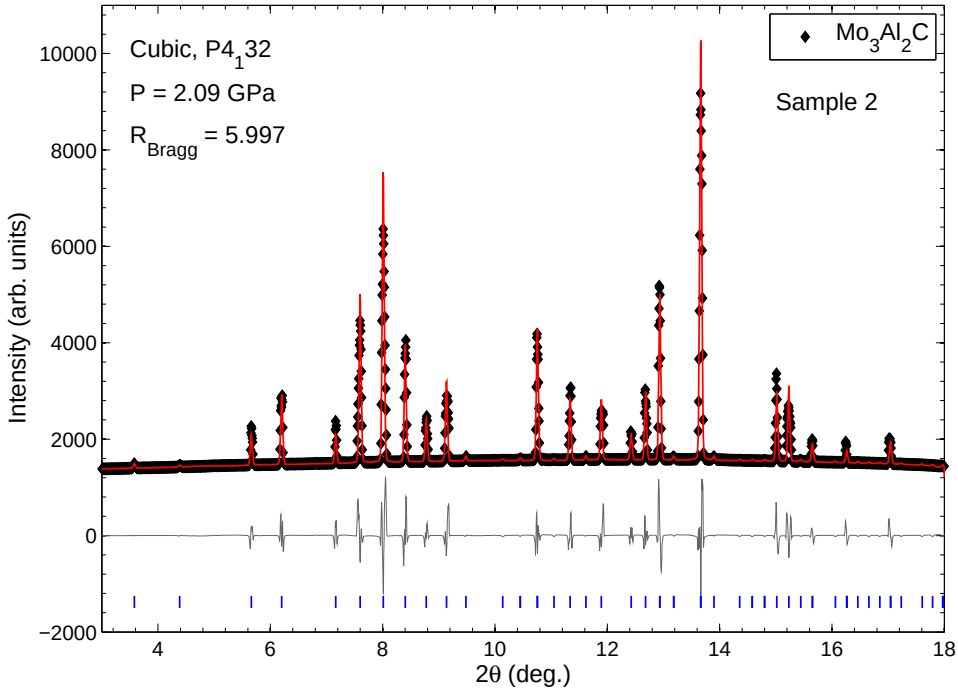

Figure 5.9: Le Bail refinement of the 41.8 keV x-ray powder diffraction pattern of Mo_3Al_2C at a pressure of 2.09 GPa. Methanol-ethanol was used as the pressure transmitting medium. The small peaks not included in the refinement most likely arise from impurities in the sample.

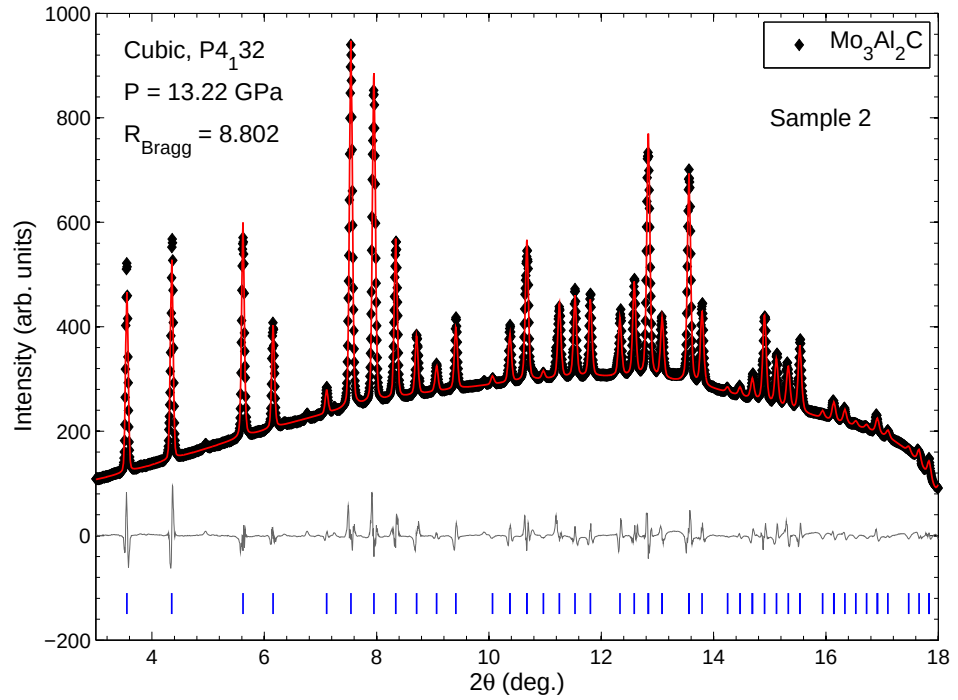

Figure 5.10: Le Bail refinement of the 41.8 keV x-ray powder diffraction pattern of Mo_3Al_2C at a pressure of 13.2 GPa just before the sample undergoes the structural transition. Methanol-ethanol was used as the pressure transmitting medium.

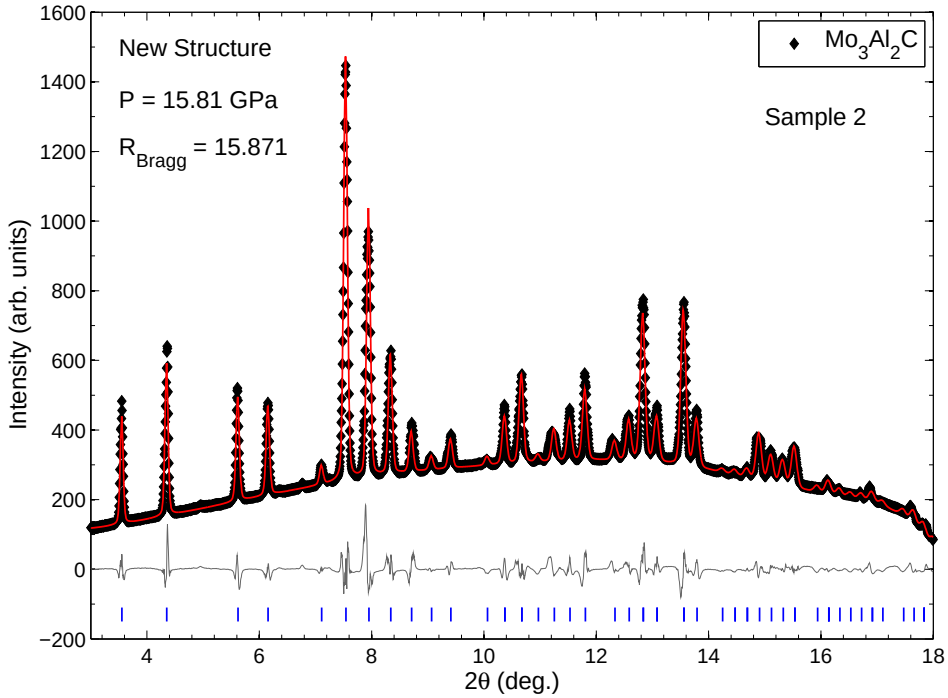

Figure 5.11: Le Bail refinement of the 41.8 keV x-ray powder diffraction pattern of Mo_3Al_2C at a pressure of 15.8 GPa. The higher value for R_{Bragg} indicates a poor fit to the data indicating that the sample has undergone a structure transition, reflected by the increase in lattice parameters above this pressure. Methanol-ethanol was used as the pressure transmitting medium.

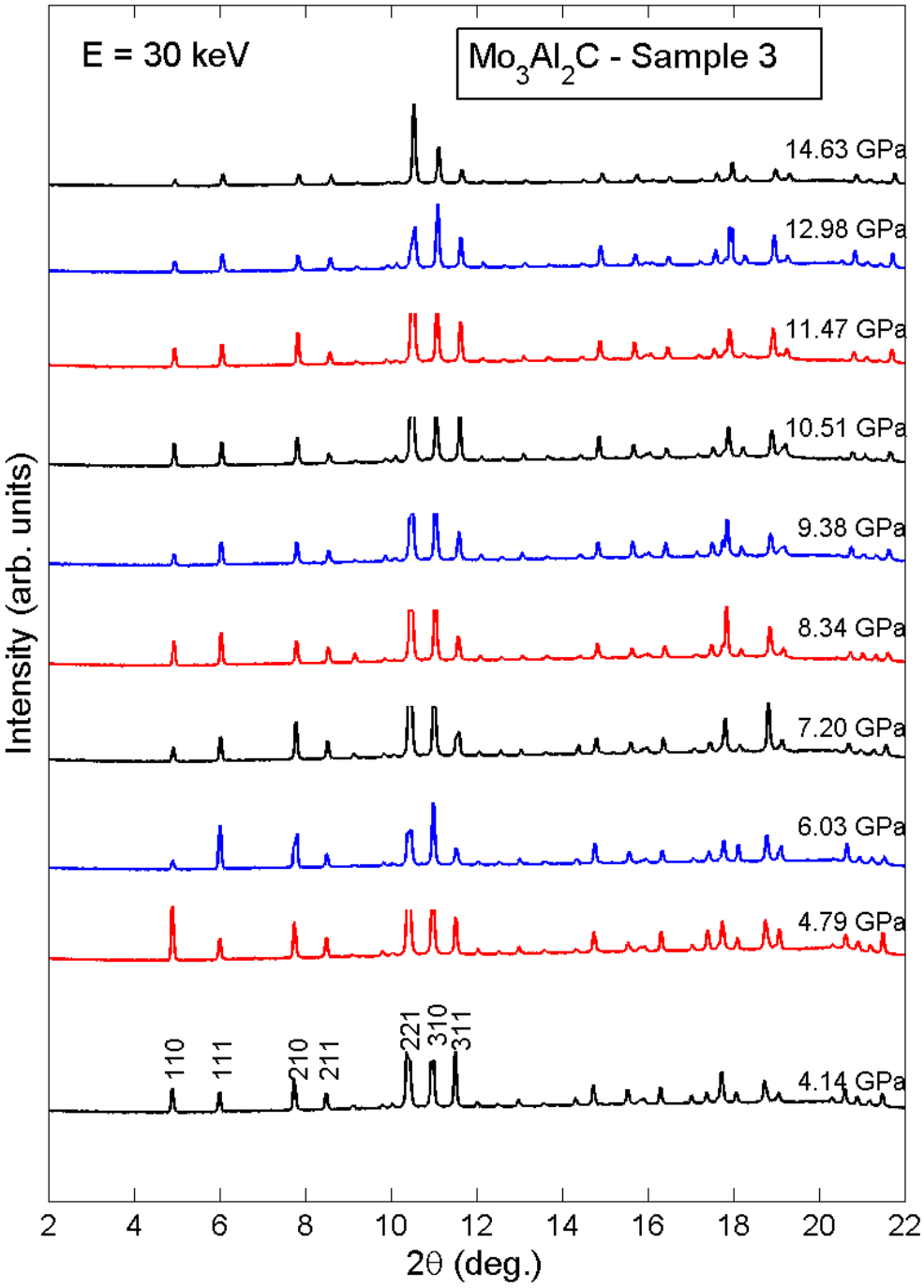

Figure 5.12: X-ray diffraction patterns of Mo_3Al_2C with increasing pressure. Only a small amount of broadening is seen even at high pressure due the helium pressure transmitting medium. Peaks are very weak due to a low beam intensity and very small sample size.

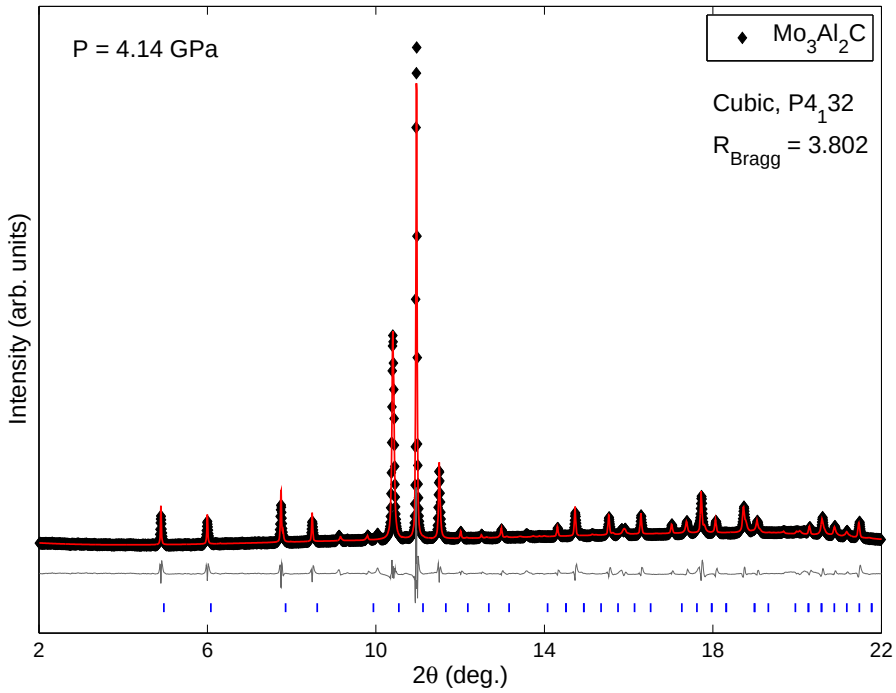

Figure 5.13: Le Bail refinement of low pressure, $P = 4.14$ GPa, Mo_3Al_2C data using 30 keV x-rays, yielding lattice parameters of $a = 6.781$Å and $V = 311.80$Å^3.

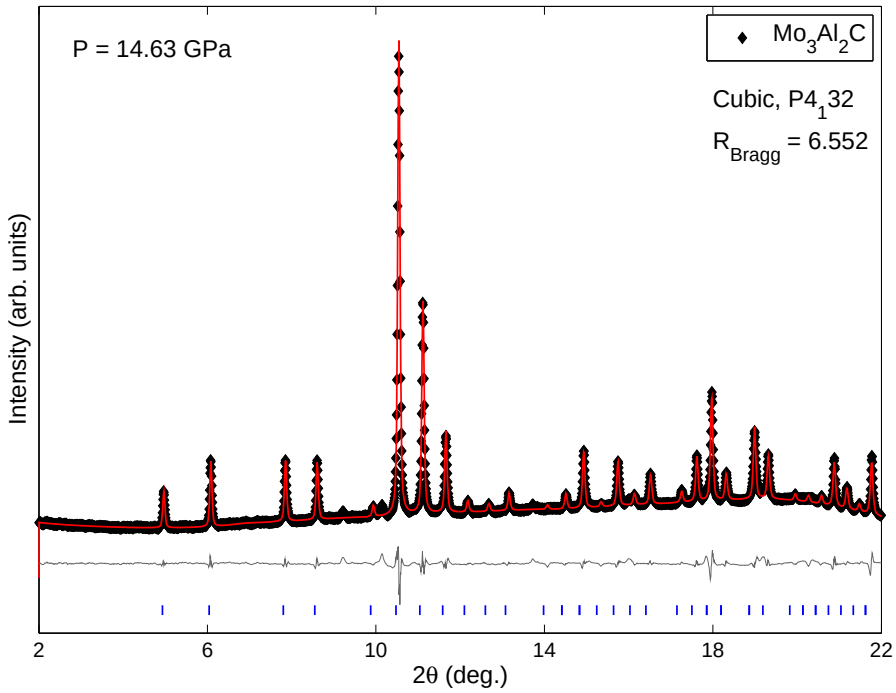

Figure 5.14: Le Bail refinement of Mo_3Al_2C collected at 14.63 GPa using 30 keV x-rays. The small amount of peak broadening at high pressure indicates good hydrostatic pressure conditions in the cell from the use of a helium pressure transmitting medium.

5.4 Pressure Dependence of T_c in Mo_3Al_2C

Measurements of the magnetic susceptibility of Mo_3Al_2C were taken to investigate the evolution of its superconducting transition temperature. Two separate samples, both of which were taken from the same bulk material, were measured up to maximum pressure of 5.77 GPa and 6.75 GPa respectively. The filling factors of the micro-coil containing the sample and Pb manometer were about 40% and 80% respectively. The filling factors and magntiudes of the superconducting transitions in the measurements point to Mo_3Al_2C displaying bulk superconductivity. Figures 5.15 and 5.16 shows upsweeps in temperature of measurements taken of the first and second samples with increasing pressure. The superconducting transition temperature, T_c was determined as the intersect of two straight lines fitted to the transition and the data leading up to it as for Mo_3Sb_7 (Figure 4.10).

5.5 Discussion

The different sets of P-V data for the three pressure transmitting media were each fitted with a Birch-Murnaghan type equation of state to obtain values for the bulk modulus, its pressure derivative and the zero pressure unit cell volume, which are summarised in table 5.3. An equation of state was also fitted to the three sets of data combined together. All values obtained for the bulk moduli and their pressure derivatives roughly agree with each other within the errors. At lower pressure up to about 15 GPa the sample remains stable in the zero pressure structural phase. Above 15 GPa the deviation of the P-V data from the fitted equation of state indicated a structural phase transition. So far no solution has been found for the high pressure structural phase of Mo_3Al_2C. The pressure transmitting medium influences the pressure of the structural transition.

The superconducting phase diagram produced from the high pressure magnetic susceptibility measurements of sample 1 of Mo_3Al_2C, figure 5.18, shows a sudden decrease

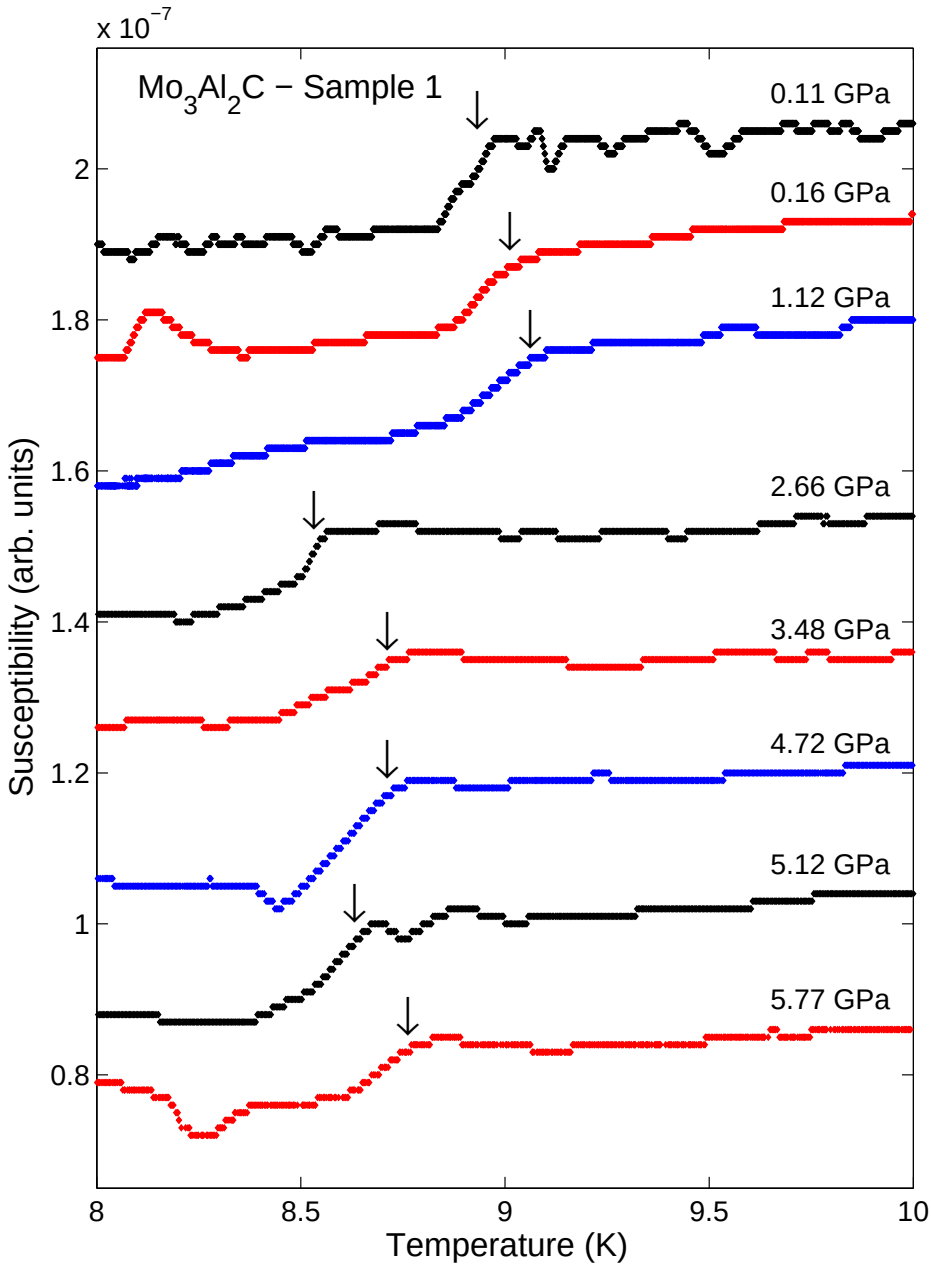

Figure 5.15: High pressure magnetic susceptibility measurements of sample 1 of Mo_3Al_2C showing the superconducting transition as a small drop in the signal. The resolution of the measurements is quite low due to too large voltage range setting of the input of the lock-in amplifier.

in T_c to about 8.4K around 2 GPa, possible due to a change in the Fermi surface, as no structural change has been observed in this pressure range measured here. Above 2 GPa T_c increases slightly ($dT_c/dp = 0.02$ GPaK^{-1}). Sample 2 showed a slightly different behaviour in that only a slight decrease was observed in T_c above 6 GPa. The behaviour of the superconductivity appears to show a very small negative slope with increasing

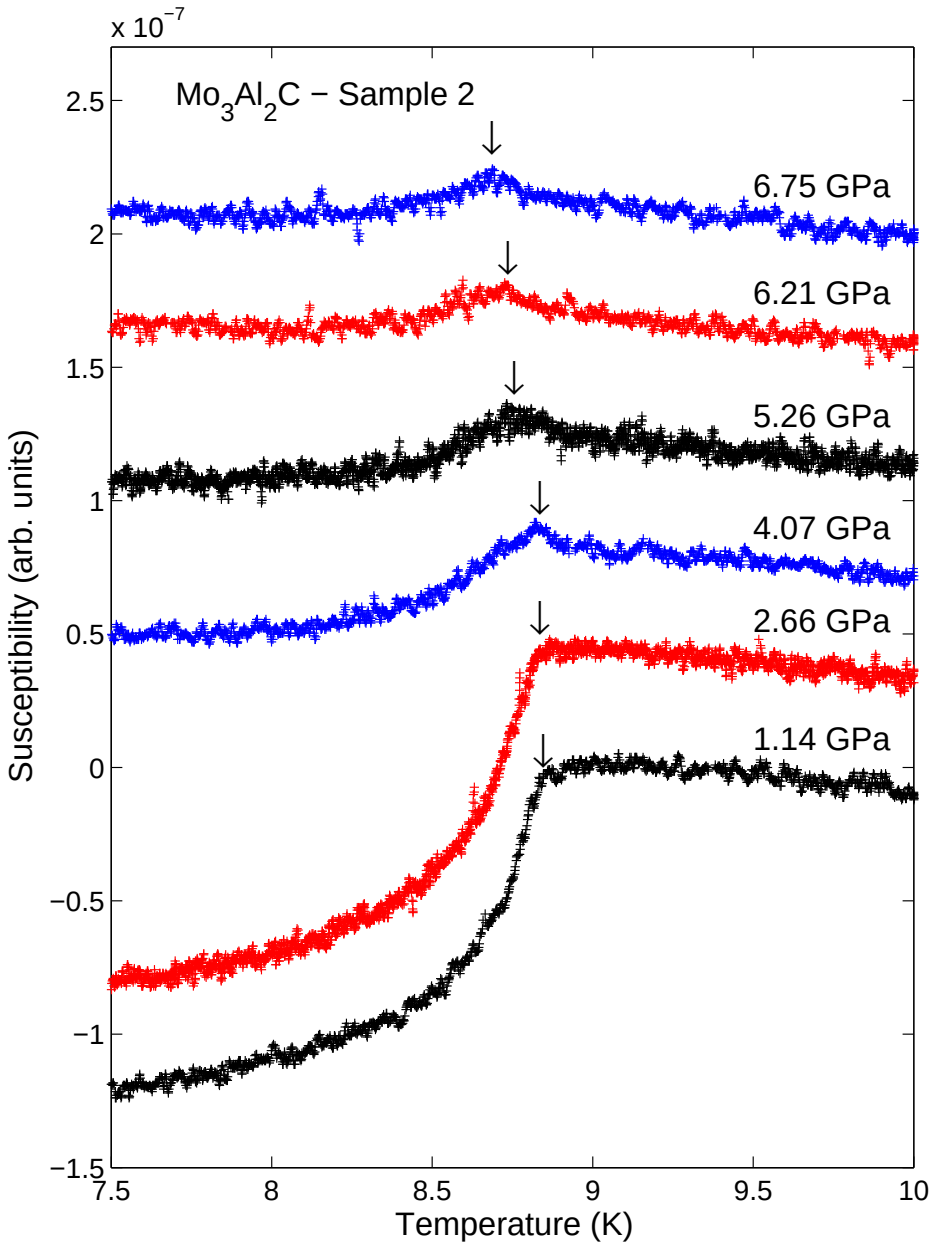

Figure 5.16: High pressure magnetic susceptibility measurements of a second sample of Mo_3Al_2C up to 6.75 GPa showing the superconducting transition temperature. The second sample showed not significant change in T_c until about 6.2 GPa, where a slight decrease was observed. The size of the transition decreases substantially from 4.07 GPa, likely due to a short developing in the micro-coil ciruit in the cell on increasing pressurisation.

pressure. The resistivity measurements performed by Bauer [11] produce slightly higher values for T_c than those obtained from the magnetic susceptibility measurements here. Overall there appears to be a small pressure dependence of T_c and the behaviour is sample dependent. The superconductivity is expected to survive up to the structural transition near 15 GPa.

	Mo_3Al_2C			
P-Medium	Silicon Oil	Methanol-Ethanol	Helium	All Data
V_0 (Å^3)	323.9 ± 0.1	323.7 ± 0.5	324.2 ± 0.3	324.3 ± 0.5
K_0 (GPa)	208.3 ± 8.2	192.4 ± 26.5	221.5 ± 14.7	192.2 ± 23.6
K_0'	6.7 ± 1.8	9.9 ± 4.4	4.1 ± 2.0	10.03 ± 3.6

Table 5.3: Zero pressure volume, V_0, bulk modulus, K_0, and pressure derivative for Mo_3Al_2C in three different pressure transmitting media obtained from the Birch-Murnaghan equation of state fit to the P-V data.

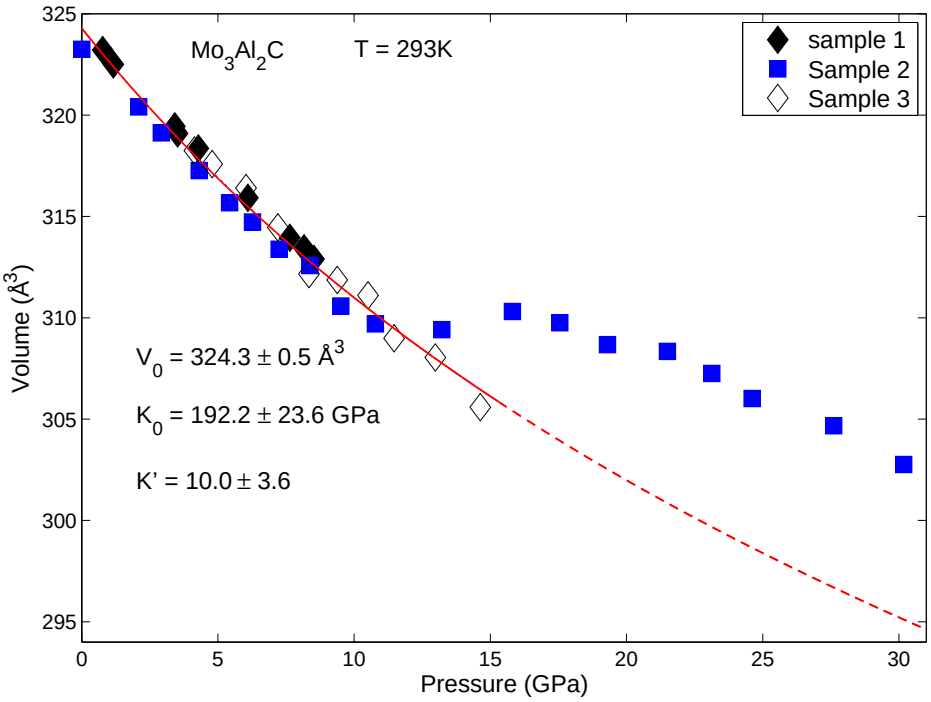

Figure 5.17: Pressure-Volume phase diagram of Mo_3Al_2C. Data collected in a silicon oil pressure medium and helium pressure medium are shown as black solid and open diamonds respectively. Data collected using the methanol-ethanol pressure transmitting medium are shown as solid blue square The P-V data for each pressure transmitting medium has been fitted with a Birch-Murnaghan type equation of state, shown as the red lines.

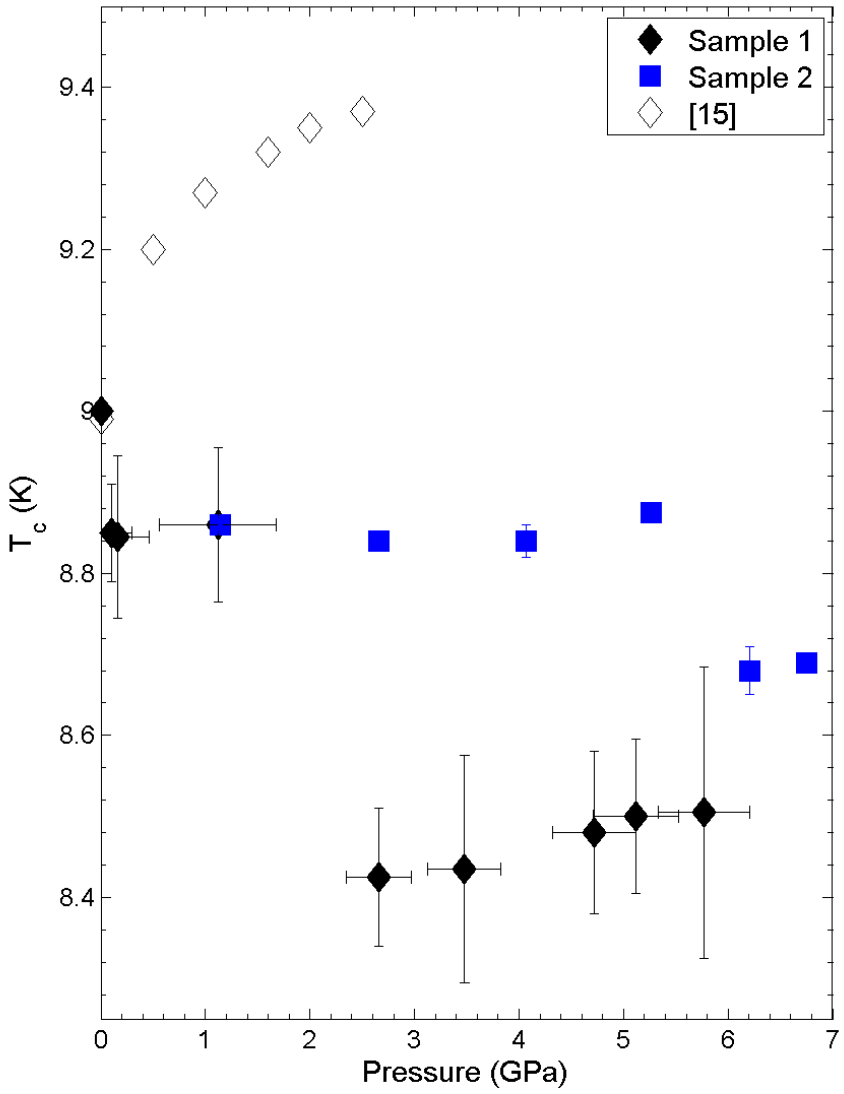

Figure 5.18: P-T phase diagram of Mo_3Al_2C showing the influence of pressure on T_c. Sample 1 (solid black diamonds) shows a slight suppression of T_c to around 8.4K is seen around 2 GPa before an increase at a very small rate of about 0.025K/GPa. Sample 2 (blue squares) shows a slight decrease in T_c above 6 GPa. The difference in the pressure dependence of the two samples could be explained pressure anisotropy. Previous resistivity measurements performed by Bauer *et. al.*, shown as open black diamonds, show an increase in T_c in Mo_3Al_2C disagree with the data collected here.

Chapter 6

Structural Phase Diagram of $K_{0.8}Fe_{2-y}Se_2$

The superconductivity in the iron selenide superconductor $K_xFe_{2-y}Se_2$ is known to be suppressed under applied pressure. In addition on further increase in pressure a second superconducting phase is observed with a higher T_c than that of the first. On application of pressure $K_xFe_{2-y}Se_2$ also undergoes a structural transition at room temperature at a critical pressure close to the suppression of the first superconducting phase. The pressure of the structural transition at low temperatures will determine whether it is responsible for the suppression of the first superconducting phase or influences the second phase.

6.1 Introduction

Among the iron-based superconductors the FeSe system gains a lot of attention due to its simple structure and interesting electronic and physical properties. Although bulk FeSe already possesses a relatively high superconducting transition temperature of $\sim$ 8K [58], T_c can be dramatically increased with high pressure [59]. In addition intercalation of FeSe led to the discovery of $A_xFe_{2-y}Se_2$ (A=K,Cs, Tl) systems with high T_c's near those of FeSe under pressure [60, 61, 62]. The superconductor $K_xFe_{2-y}Se_2$ exhibits

superconductivity with correct tuning of x and y with a T_c as high as ~ 32.8K [63].

$K_{0.8}Fe_{2-y}Se_2$ ($y = 0, 0.4$) crystallises in the tetragonal $ThCr_2Si_2$ type structure (space group: I4/mmm) above 550K and zero pressure. $K_{0.737}Fe_{1.631}Se_2$ has lattice parameters $a = 8.729$Å $c = 14.120$Å, and unit cell volume $V = 1075.88$Å^3. The x-ray powder diffraction measurements of the $y = 1.78$ also revealed the existence of a Fe-vacancies superstructure which lowers the crystal symmetry to I4/m between T_S (just above T_N) and the lowest temperatures. A schematic of the unit cell with vacancies is shown in figure 6.1 As well as this they are found to have a much higher T_c than their isostructural KFe_2As_2. Properties of these materials have been found to depend on the Fe-valence which can be precisely controlled by varying x and y. Recently Y. J. Yan *et. al.* [63] studied many single crystal samples to build up the structural, electronic and magnetic phase diagram of $K_xFe_{2-y}Se_2$ as a function of Fe-valence, V_{Fe}, shown in figure 6.2.

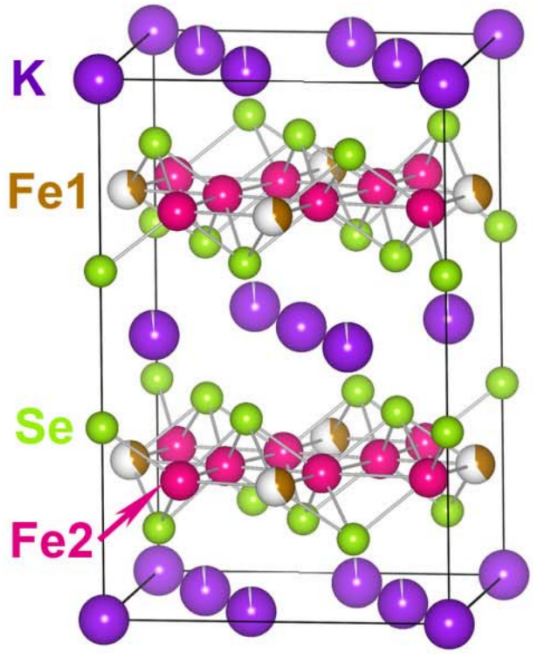

Figure 6.1: Schematic of the unit cell of $K_xFe_{2-y}Se_2$ in the *I4/m* crystal structure [64].

Below T_N the Fe-valence phase diagram of $K_2Fe_{2-y}Se_2$ is split into the three distinct regions. For $V_{Fe} \geq 2.00$ and $V_{Fe} < 1.935$ an insulating state with long ranged antifer-

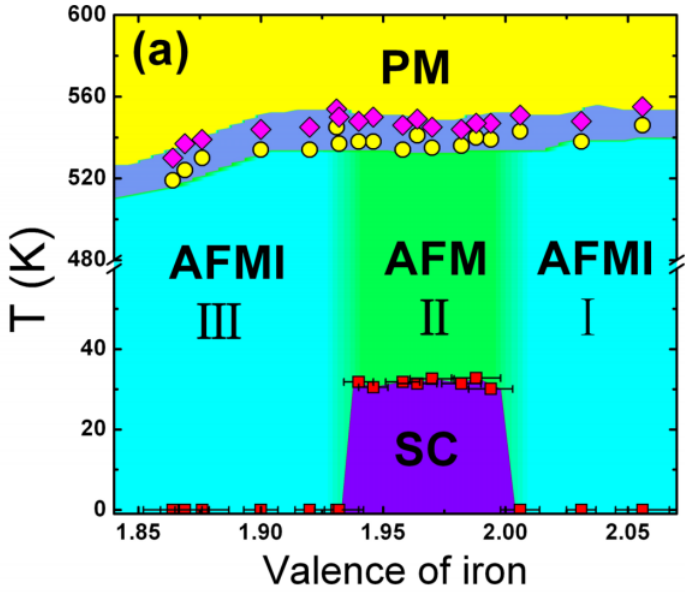

Figure 6.2: Electronic and magnetic phase diagram of $K_xFe_{2-y}Se_2$ as a function of iron valence, with the Néel temperature indicated by yellow circles, the temperature of the structural phase transition by purple diamonds and the superconducting transition temperature by red squares [63]. Samples in region II undergo a insulator to metaillic transition going to low temperatures.

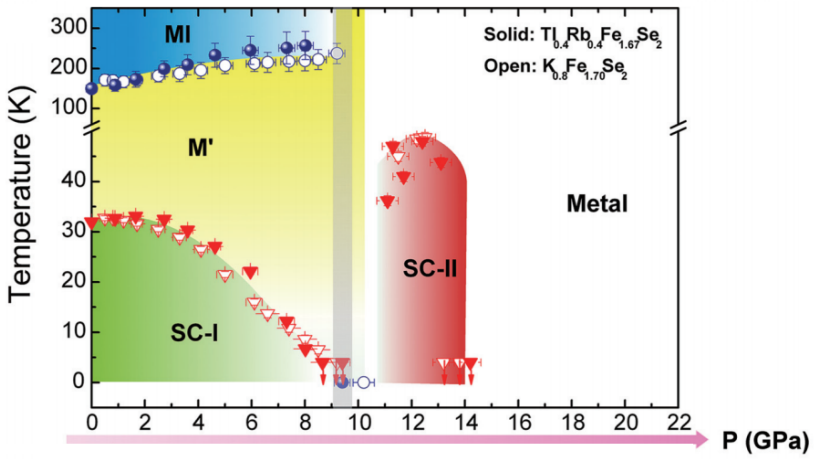

Figure 6.3: Pressure-temperature phase diagram of superconducting $Tl_{0.4}Rb_{0.4}Fe_{1.67}Se_2$ and $K_{0.8}Fe_{1.70}Se_2$. The insulating to metallic transition of $K_{0.8}Fe_{1.7}Se_2$ is shown by the open circles [65].

romagnetic order is observed. For $1.935 < V_{Fe} < 2.00$ an long range antiferromagentic order is observed along with the existence of superconductivity below a temperature $T_c \sim 30$K. In this region the sample undergoes an insulating to metallic transition as they go to low temperatures, as can be seen from resistivity measurements performed by P. Gao *et al.* [65]. The superconductivity is a minority phase which coexists with

the majority insulating phase [66].

Room temperature x-ray powder diffraction measurements, figure 6.4, of $K_{0.8}Fe_ySe_2$ ($y = 1.7, 1.78$) at high pressure [12] reveal that the tetragonal I4/m structural phase with Fe-vacancy order exists up to 9.2 GPa. On further increase of the pressure to 10.3 GPa the (110) peak is fully suppressed indicating a structural transition into a I4/mmm structure.

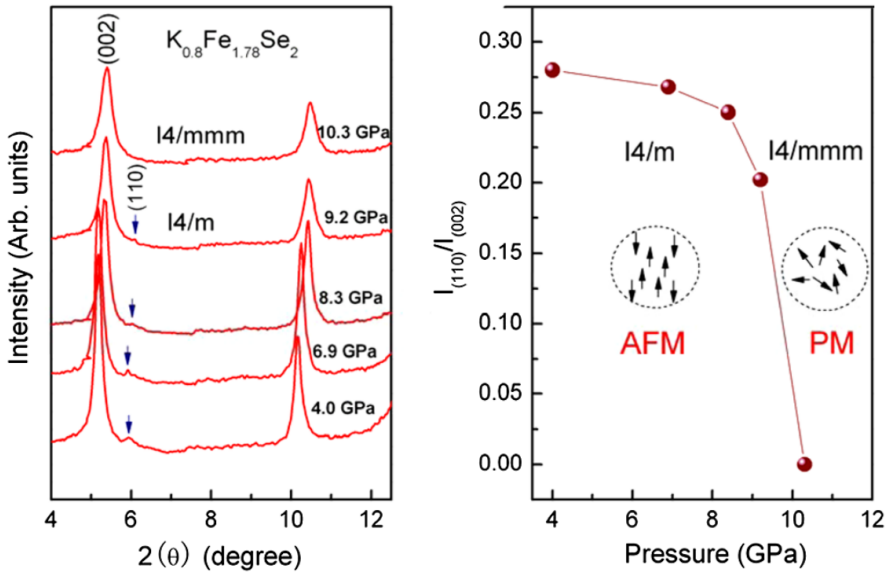

Figure 6.4: The left plot shows x-ray powder diffraction patterns of $K_{0.8}Fe_{1.78}Se_2$ using an energy of 18 keV showing suppression of the superstructure by 10.3 GPa [67]. The suppression of the Fe-vacancy order is reflected by the decreasing value of the ratio of the (110) and (002) peak intensities.

Resistivity and magnetic susceptibility measurements have been performed at zero pressure over all three V_{Fe} regions [63]. Samples in region I were measured up to 600K and all exhibit a sharp jump in the resistivity around 525 to 550K due to the structural transition and the onset of antiferromagnetic order at T_N before showing insulating behaviour down to low temperatures increasing by about eight orders of magnitude. No superconductivity is seen in these samples. All samples from region III showed similar behaviour to those from region I. Samples with compositions from region II show the same jump in resistivity at T_S and T_N as those from regions I and III, however

they exhibit an insulating to metallic transition when going to low temperatures and eventually undergo a superconducting transition around 30K.

High pressure resistivity measurements [12] showed that T_c gradually decreased with increasing pressure. T_c is found to be suppressed to $T = 0$K at the critical pressures 9.2 and 9.7 GPa for $K_{0.8}Fe_{1.7}Se_2$ and $K_{0.8}Fe_{1.78}Se_2$ respectively around the same pressure where the structural transition occurs at room temperature and therefore the Fe-vacancy has been proposed to play a key role in the superconducting phase diagram [68]. Resistivity measurements performed to higher pressures [67], figure 6.5, reveal the appearance of a second superconducting phase with a much higher T_c. The superconducting phase diagram of both $K_{0.8}Fe_{1.7}Se_2$ and $K_{0.8}Fe_{1.78}Se_2$, shown earlier in figure 6.18, show the second superconducting phase emerges at about 11.5 GPa before disappearing again by 13.2 GPa. A highest value for T_c of about 48K is seen in the sample at 12.5GPa.

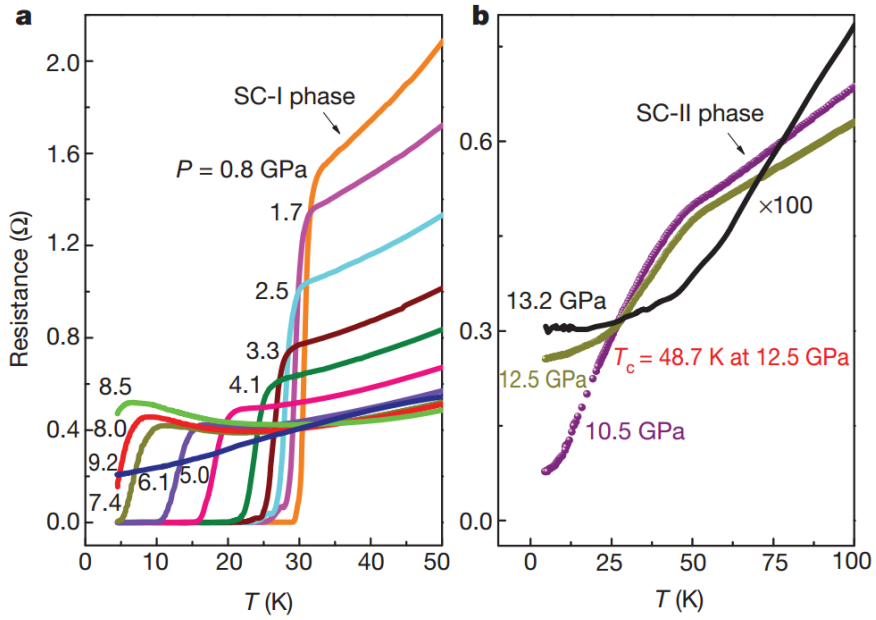

Figure 6.5: Temperature dependence of the resistivity of $K_{0.8}Fe_{1.7}Se_2$ with increasing pressure [12]. (a) The suppression of T_c for the first superconducting phase of $K_{0.8}Fe_{1.7}Se_2$ showing it's complete disappearance by 9.2 GPa. (b) A second superconducting phase is revealed above 10.5 GPa, reaching a maximum of 48.7K at 12.5 GPa, before it disappears again at 13.2 GPa. The black line is multiplied by 100.

6.2 Experimental Details

Two single crystal samples were used for measurements; a superconducting and an insulating sample. The superconducting sample has a nominal composition of $K_{0.733}Fe_{1.668}Se_2$ and will be referred to as $K_{0.8}Fe_2Se_2$ throughout this thesis. The insulating sample has a nominal composition of $K_{0.792}Fe_{1.599}Se_2$ and will be refered $K_{0.8}Fe_{1.6}Se_2$. Table 6.1 summarises these details.

Sample	Nominal Composition	Name in thesis	V_{Fe}
Superconducting	$K_{0.773}Fe_{1.668}Se_2$	$K_{0.8}Fe_{1.7}Se_2$	1.958
Insulating	$K_{0.792}Fe_{1.559}Se_2$	$K_{0.8}Fe_{1.6}Se_2$	2.006

Table 6.1: Information on the two different samples measured in this thesis.

Both grown by the group of X. H. Chen. High pressure x-ray powder diffraction was performed on the insulating $K_{0.8}Fe_{1.6}Se_2$ at room temperature. A good quality powder was produced by grinding single crystals of $K_{0.8}Fe_{1.6}Se_2$ in a nitrogen atmosphere to avoid degradation of sample quality before being pressed between two glass slides. A small $\sim 50\mu$m piece of sample was loaded into a Holzapfel-Syassen diamond anvil cell along with a small ruby chip for pressure determination. Other experimental details are summarised in table 6.2. Diffraction patterns were obtained up to a maximum pressure of 13.8 GPa. Le Bail refinements were used to obtained lattice parameters for each pressure point.

	Beam Energy	Beam Diameter	Pressure Medium
Room Temperature	40 keV	30μm	Helium
Low Temperature	30 keV	70μm	none

Table 6.2: Experimental parameters for room temperature and low temperature x-ray powder diffraction measurements of $K_{0.8}Fe_{1.6}Se_2$ and $K_{0.8}Fe_2Se_2$.

Low temperature x-ray powder diffraction was performed on the superconducting $K_{0.8}Fe_2Se_2$ and insulating $K_0.8Fe_{1.6}Se_2$ samples. Single crystal samples crushed into a high-purity powder were loaded into Holzapfel-Syassen diamond anvil cells to obtain

low temperature powder diffraction patterns using the pulse tube cryostat described in section 3.3.1. A small piece of sample was loaded into the hole of a rhenium gasket. Other experimental details are summarised in table 6.2. Several attempts at loading with either a helium or NaCl pressure transmitting medium were unsuccessful as a sample signal could not be seen above the cryostat background. Finally no pressure medium was used and the cell packed with sample to maximise sample signal, along with a thin copper disc as an internal x-ray calibrant. Le Bail refinements were used to obtained lattice parameters from the integrated diffraction patterns. An exposure time of 300 seconds was used for each pattern so that temperature of the sample did not change much during the measurement. It is estimated that the temperature would have changed no more than about 2K during each exposure.

6.3 High Pressure X-ray Powder Diffraction at room temperature in $K_{0.8}Fe_{2-y}Se_2$ (y = 0, 0.4)

All patterns of $K_{0.8}Fe_{1.6}Se_2$ collected at room temperature can be seen in figure 6.6 and have all been normalised to the (123) peak. The ruby fluorescence lines and powder diffraction peaks remain well defined up to the highest pressure indicating a hydrostatic pressure. The suppression of the (110) peak indicates that the sample undergoes a structural transition between 10.99 and 12.65 GPa. Le Bail refinements were carried out on all the room temperature powder diffraction patterns using the zero pressure and room temperature $I4/m$ structure to obtain lattice parameters with increasing pressure. A Le Bail refinement of $K_{0.8}Fe_{1.6}Se_2$ at 1.04 GPa in the low pressure structure is shown in figure 6.7. The good fit of the refinement to the data along with the low R_{wp} value indicate that the assumed structure is correct. A Le Bail refinement of the powder diffraction pattern of $K_{0.8}Fe_{1.6}Se_2$ at a pressure of 12.65 GPa confirms the high pressure $I4/mmm$ structure. The refinement fits the data well with a low R_{wp} value. A structural transition into a collapsed tetragonal structural phase was not observed in $K_{0.8}Fe_{1.6}Se_2$

up to the maximum pressure of 13.8 GPa in contrast to the isostructural iron-pnictide KF_2As_2.

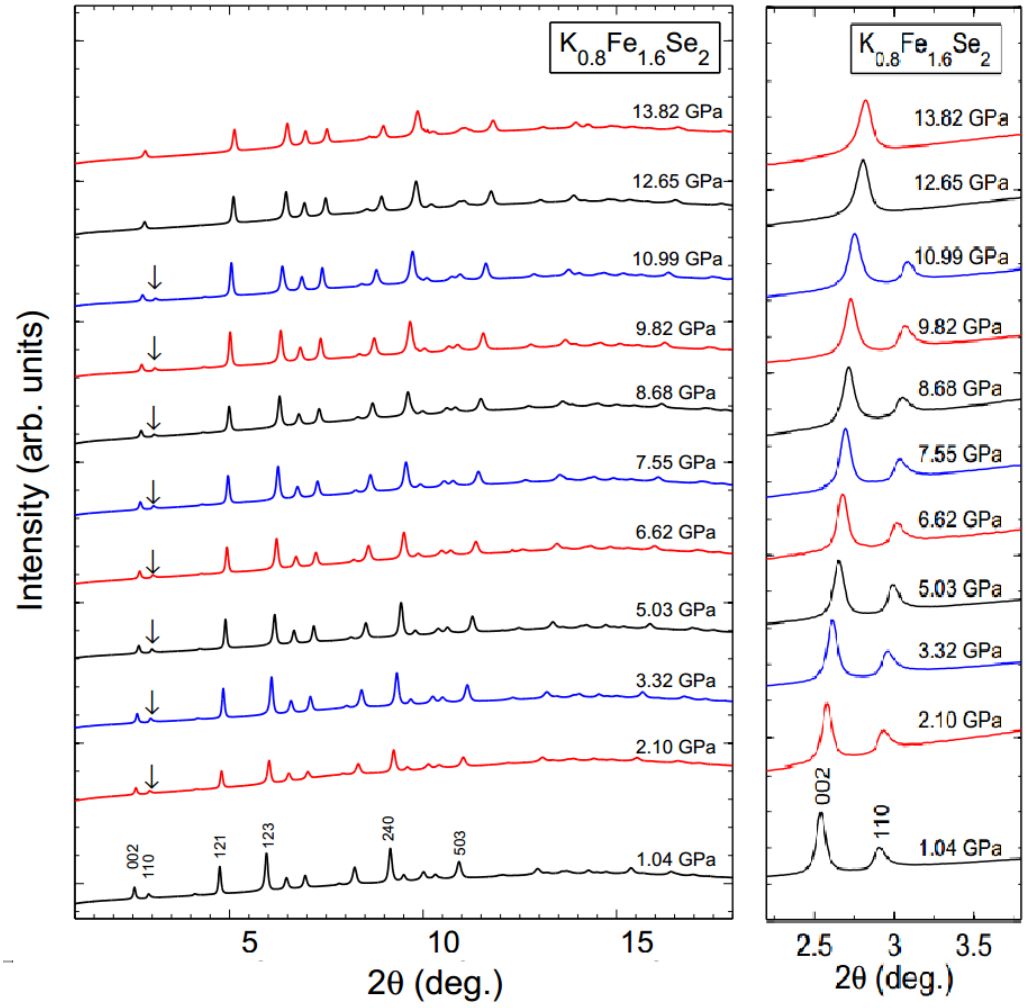

Figure 6.6: *Left*: Room temperature x-ray powder diffraction patterns of $K_{0.8}Fe_{1.6}Se_2$ with increasing pressure using a beam energy of 40 keV. Helium was used as a pressure transmitting medium. The presence of the (110) peak is marked by black arrows. The disappearance of the (110) peak indicates the structural phase transition from I4/m to I4/mmm. *Right*: Zoom in on the (002) and (110).

In order to prepare the low temperatures and be able to scan the pressure-temperature phase space efficiently afterwards the location of the structural transition in the differernt samples was determined first. One room temperature diffraction pattern of the insulating $K_{0.8}Fe_{1.6}Se_2$ was also taken in the cryostat prior to a cool down. Room temperature x-ray powder diffraction patterns of two different samples of the supercon-

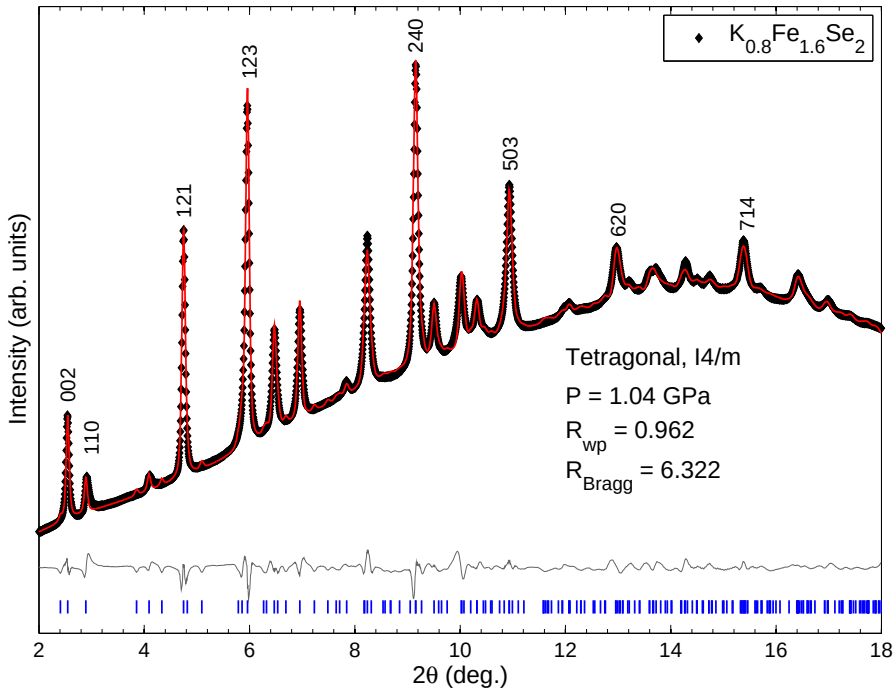

Figure 6.7: Refinements of the 40 keV powder diffraction pattern of $K_{0.8}Fe_{1.6}Se_2$ at pressure a of 1.04 GPa using the I4/m structure. Lattice parameters of $a = 8.672$ and $c = 13.949$ Å and a unit cell volume $V_0 = 1048.959$ Å^3 are obtained from the refinement.

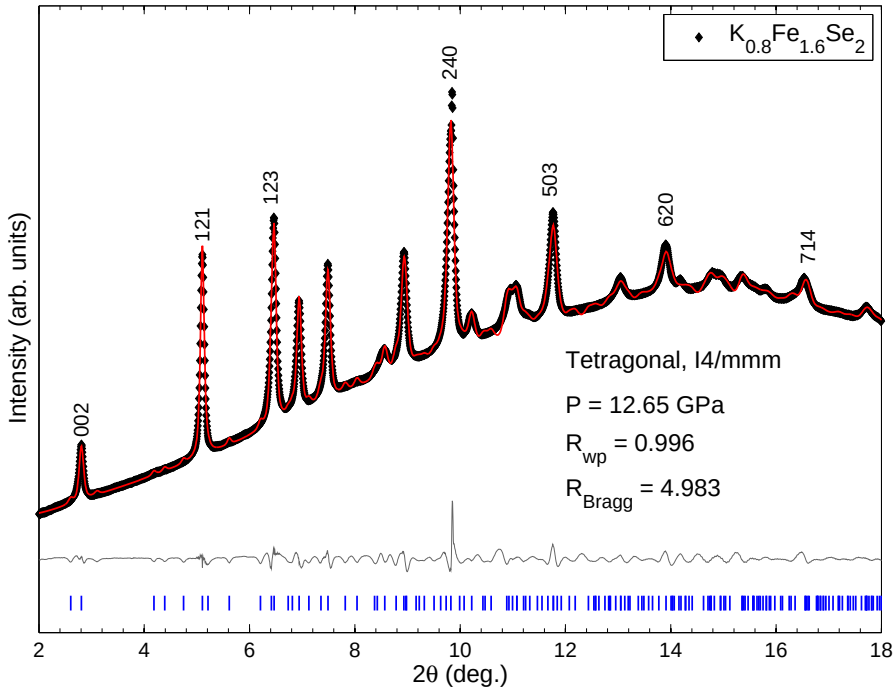

Figure 6.8: Refinement of the powder diffraction pattern, 40 keV, of $K_{0.8}Fe_{1.6}Se_2$ at a pressure of 12.65 GPa using the I4/mmm structure. The high pressure structure is indicated by the lack of the [110] peak seen in the low pressure structure pattern. The refinement yields a lattice parameter $a = 8.089$ and $c = 12.644$ Å and a unit cell volume $V_0 = 828.166$ Å^3.

ducting $K_{0.8}Fe_2Se_2$ were obtained with the sample loaded into the cryostat.. Diffraction patterns of the two superconducting samples were obtained to maximum pressures of about 13.5 and 10.2 GPa. Parts of the patterns showing the (002) and (110) peaks with increasing pressure are shown in figures 6.9a and 6.9b. For the first sample the suppression of the (110) peak was observed between 12.47 and 12.55 GPa indicating a structural transition. A high enough pressure was not reached for sample 2 to see the structural transition. There are high levels of peak broadening in both cells even from the lowest pressures due to the use of the sample as the pressure medium. The ratio of the intensities of the intesities of the (110) and (002) peak with increasing pressure, figure 6.10, shows a very sharp drop indicating a very sudden disappearance of the (110) peak at 12.5 GPa. The structural transition in the superconducting sample occurs in the same pressure region as that for the insulating sample.

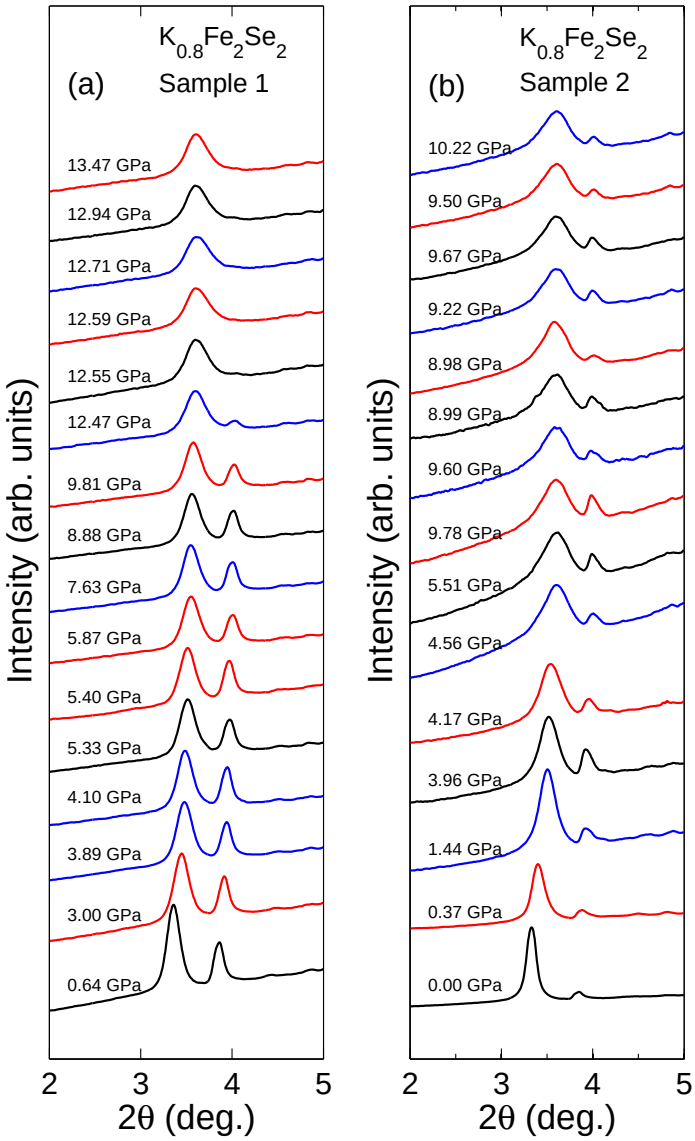

Figure 6.9: Integrated intensities at low diffraction angles of two $K_{0.8}Fe_2Se_2$ samples at room temperature and various pressures. The (002) and (110) smoothly shift to higher 2θ angles. In (a) the disappearance of the (110) peak indicates a structural phase transition between 12.47 and 12.55 GPa.

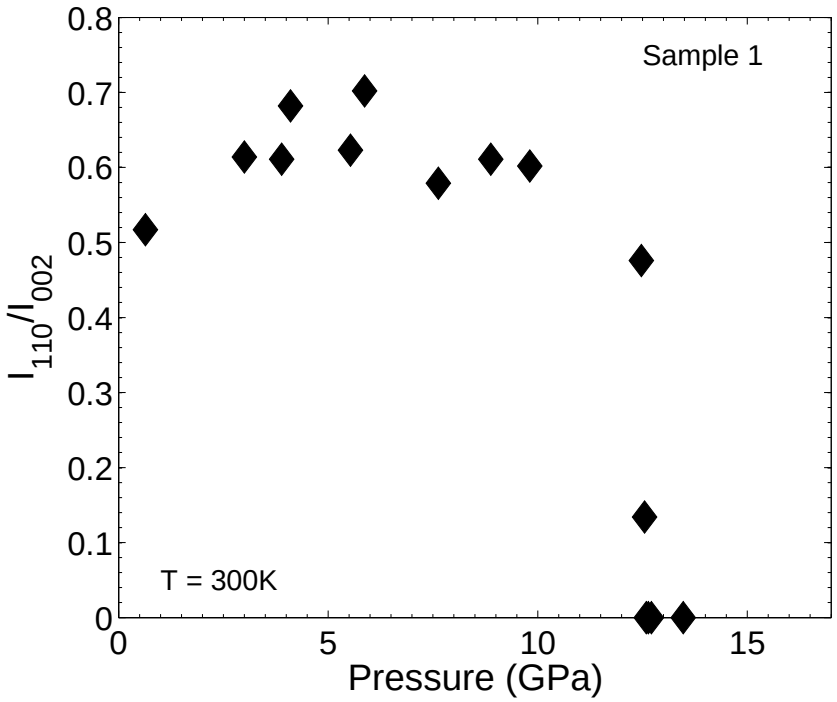

Figure 6.10: Intensity ratio of the (110) and (002) peaks of $K_{0.8}Fe_2Se_2$. The rapid decrease at 12.5 GPa indicates the structural transition into the high pressure I4/mmm phase.

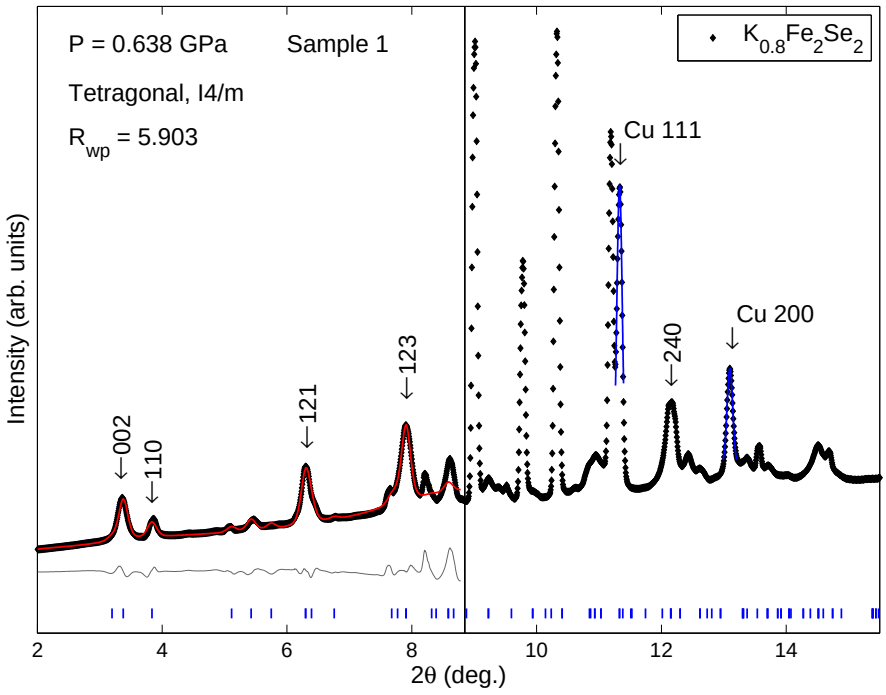

Figure 6.11: Le Bail refinement of $K_{0.8}Fe_2Se_2$ sample 1 at a pressure of 0.64 GPa. The part of the diffraction pattern to the right of the black line has been entirely excluded from the refinement. The Cu calibrant peaks are shown in blue.

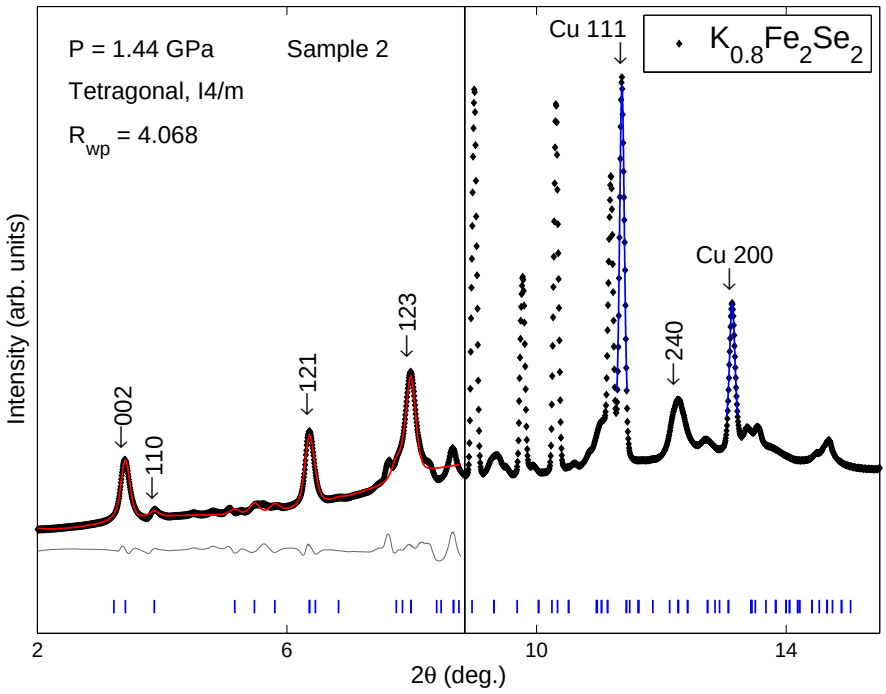

Figure 6.12: Le Bail refinement of $K_{0.8}Fe_2Se_2$ sample 2 at $P = 1.44$ GPa. Peaks from the Cu pressure calibrant are shown in blue. Again the refinement excludes the cryostat background and Cu calibrant.

6.4 X-ray Powder Diffraction of $K_{0.8}Fe_{2-y}Se_2$ (y = 0, 0.4) as a Function of Pressure and Temperature

X-ray powder diffraction patterns of $K_{0.8}Fe_{2-y}Se_2$ (y = 0, 0.4) were obtained for various different temperatures and pressures. Measurements were taken during one cool down for a first cell loading of a superconducting $K_{0.8}Fe_2Se_2$ sample, referred to as *SC Sample 1*. Two cool downs were carried out for two different starting pressures for a second loading of another superconducting $K_{0.8}Fe_2Se_2$ sample, referred to as *SC Sample 2*. Low temperature measurements of an insulating $K_{0.8}Fe_{1.6}Se_2$ sample, referred to *Insulating Sample*, were obtaining during one cool down. Table 6.3 summarises the starting temperatures and pressures for each sample. For all patterns only data up to a 2θ angle of 8.8° was used for the Le Bail refinement as was in figures 6.11 and 6.12.

X-ray powder diffraction patterns of an insulating $K_{0.8}Fe_{1.6}Se_2$ sample were obtained at

Sample	P_{RT}	T_{min}
$K_{0.8}Fe_{1.6}Se_2$ -Insulating Sample, cooldown 1	0.3 GPa	15K
$K_{0.8}Fe_2Se_2$ - SC Sample 1, cooldown 1	12.0 GPa	10K
$K_{0.8}Fe_2Se_2$ - SC Sample 2, cooldown 1	5.7 GPa	10K
$K_{0.8}Fe_2Se_2$ - SC Sample 2, cooldown 2	11.3 GPa	10K

Table 6.3: Room temperature starting pressures, P_{RT} and minimum temperatures, T_{min} for various cool downs of three different samples.

various temperatures down to a minimum temperature of 15K. The cool down started at a room temperature pressure of about 0.3 GPa. Low 2θ angle data of these patterns showing the (002) and (110) peaks with increasing temperature is shown in figure 6.13a. The increase in pressure in the cell to 1.9 GPa at 15K is due to the thermal contraction of the diamond anvil cell during the cool down. No diffraction from the copper pressure calibrant was observed in the 160K pattern and therefore the pressure for this temperature is not known. The intensity of the (110) compared to the (002) peak for this sample was very low for the initial measurement. The (110) peak remains present in all patterns down to the lowest temperature of the cool down.

Diffraction patterns of sample 1, the first superconducting $K_{0.8}Fe_2Se_2$ sample, were obtained to a lowest temperature of 10K and are shown in figure 6.13b. The cool down started at a room temperature pressure of 12.0 GPa, just before the full suppression of the (110) peak as seen in figure 6.9. Small remains of the low pressure (110) peak intensity are still present in the patterns for all temperatures during this cooldown. Again the pressure increases as the temperature decreases due to the thermal contraction of the cell. At the lowest temperature during this run the pressure in the cell had increased to 13.9 GPa. The large amount of peak broadening seen in the (002) peak indicate poor hydrostatic conditions in the pressure cell due to the use of the sample as pressure transmitting medium.

Patterns of sample 2, the second superconducting $K_{0.8}Fe_2Se_2$ sample, were obtained during two separate low temperature runs. Powder diffraction patterns obtained during

the first cool, starting with a room temperature pressure of 5.7 GPa are shown in figure 6.14a. The intensity of the (110) peak is much higher than that in the measurements of sample 1, probably due to a preferential orientation of the crystallites in the powder. The (110) peak is clearly still present in the patterns at all temperatures, even for the highest pressure of 13.3 GPa at 10K. The intensity of the (110) peak appears to decrease slightly as the sample goes to lower temperatures. The peaks are slightly broader at the highest pressure at lower temperature as the hydrostaticity in the cell decreases. Powder diffraction patterns obtained during the second temperature run, starting with a room temperature pressure of 11.3 GPa are shown in figure 6.14b. The 280K pattern at 11.3 GPa shows a very small amount of intensity remaining for the (110) peak. At lower temperatures where the pressure has increased to above 16 GPa the (110) peak has been fully suppressed. During this temperature run patterns could not be obtained for temperatures between 280 and 210K due to a loss of x-rays from the synchrotron.

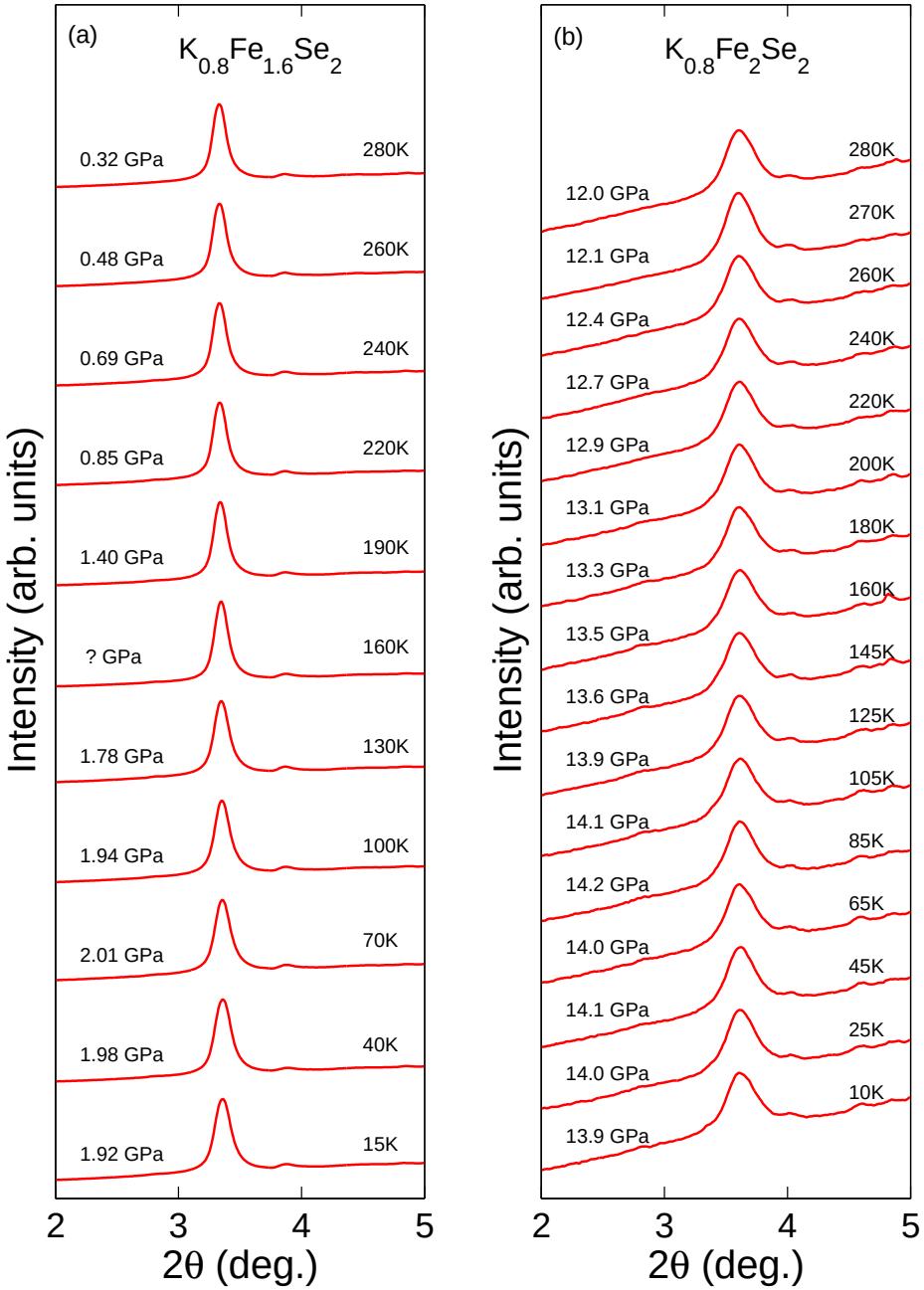

Figure 6.13: (a) Low angle x-ray powder diffraction data for $K_{0.8}Fe_{1.6}Se_2$ with decreasing temperature for a room temperature pressure of about 0.3 GPa. The small (110) peak to the right of the main [002] peak shows that the Fe-vacancy superstructure is present in the sample down to 15K at low pressures. (b) Cool down of the first $K_{0.8}Fe_2Se_2$ sample for a room temperature pressure of around 12 GPa. The (110) peak is still present for all temperatures indicating that the sample is still in I4/m structure.

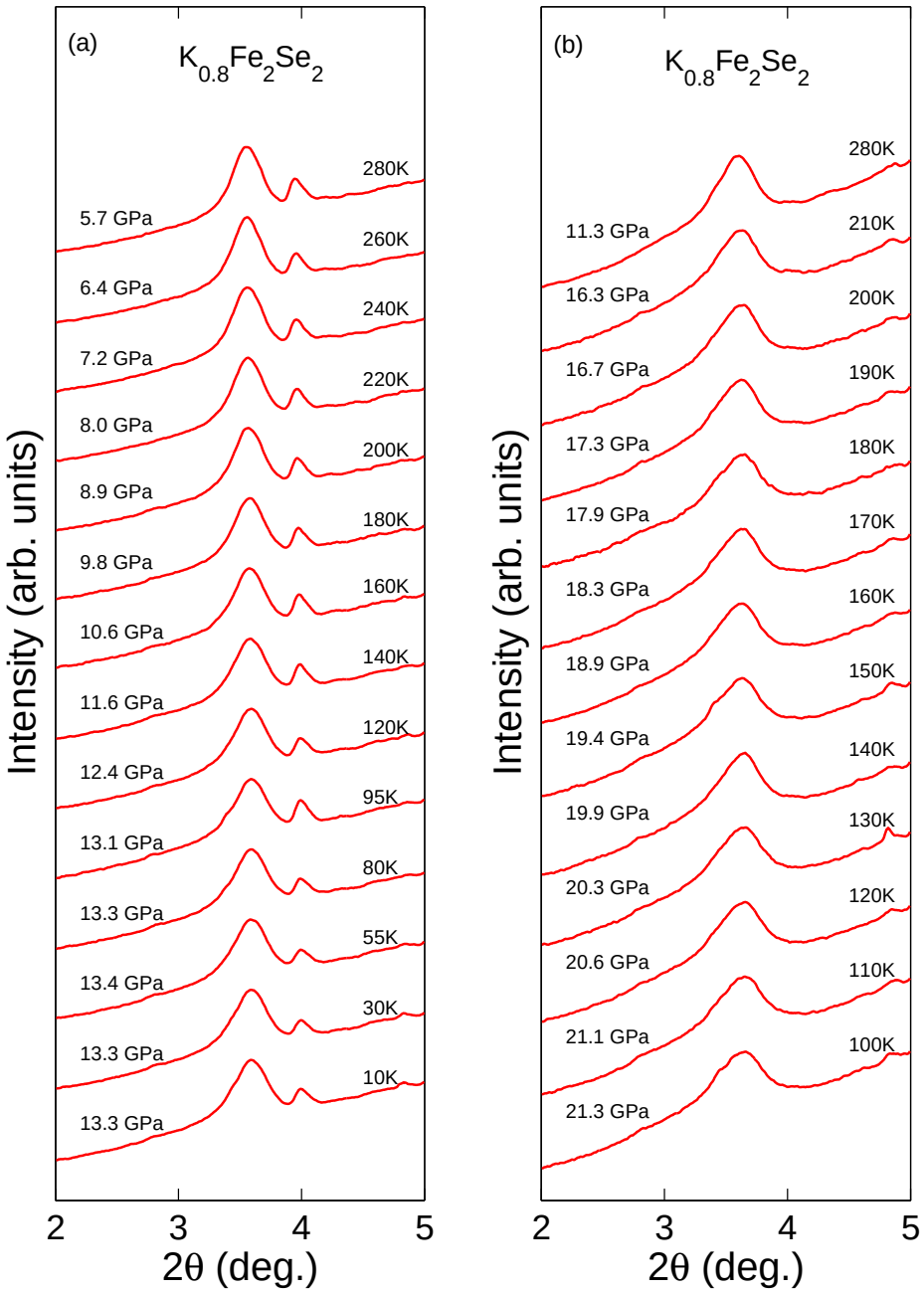

Figure 6.14: (a) X-ray powder diffraction data for the first cool down of sample 2 of $K_{0.8}Fe_2Se_2$ with decreasing temperature for a room temperature pressure of 5.7 GPa. The Fe-vacancy structure is present in the sample at all temperatures. The intensity of the peak starts to decrease slightly above 13.3 GPa at 80K. (b) Second cool down of sample 2 starting with a room temperature pressure of 11.3 GPa. The (110) peak has been suppressed indicating the lack of an Fe-vacancy order down to low temperature.

6.5 Discussion

Lattice parameters obtained from the Le Bail refinements of the insulating $K_{0.8}Fe_{2-y}Se_2$ data have been plotted against pressure in figure 6.15. The *P-V* data has been fitted with a 3rd order Birch-Murnaghan type equation of state, equation 2.6, and parameters obtained from the fit are summarised in table 6.4. The deviation of the data from the fitted equation of state above indicate the structural phase transition occurs at a pressure between 11 and 12.6 GPa at room temperature. This critical pressure is around 2-3 GPa higher than that previously measured for superconducting $K_{0.8}Fe_{1.78}Se_2$ [67]. The structural transition appears to have much more of an effect on the c direction of the unit cell as can be seen by a much higher deviation of c above 12 GPa from the equation of state as can be seen in the upper inset of figure 6.15.

	$K_{0.8}Fe_{1.6}Se_2$	$K_{0.8}Fe_2Se_2$
V_0 (Å^3)	1078.1 ± 2.1	1077.8 ± 4.6
K_0 (GPa)	31.5 ± 1.6	28.2 ± 2.9
K_0'	3.8 ± 0.4	6.6 ± 1.8

Table 6.4: Room temperature values for zero pressure volume (V_0), bulk modulus (K_0) and pressure derivatives obtained from Birch-Murnaghan equation of state fits to the *P-V* data for $K_{0.8}Fe_{1.6}Se_2$ and $K_{0.8}Fe_2Se_2$ sample.

Plots of the ratio of the intensities of the (110) and (002) peaks and the differences between their 2θ positions of the sample 1, superconducting $K_{0.8}Fe_2Se_2$, with increasing pressure can be seen in figures 6.10a and 6.10b. The sharp drop in both plots around 12.5 GPa indicate a strong first order structural phase transition occurs. Again as for the insulating $K_{0.8}Fe_{1.6}Se_2$ sample the pressure for the structural transition is higher than previous measurements [67] at room temperature. Lattice parameters obtained from the Le Bail refinements for samples 1 and 2, both superconducting $K_{0.8}Fe_2Se_2$, at room temperature have been plotted against pressure in figures 6.16 and 6.17 respectively. Birch-Murnaghan equation of states have been fitted to both sets of *P-V* data. Values for parameters obtained from the equation of state fit can be found in table 6.4. Due

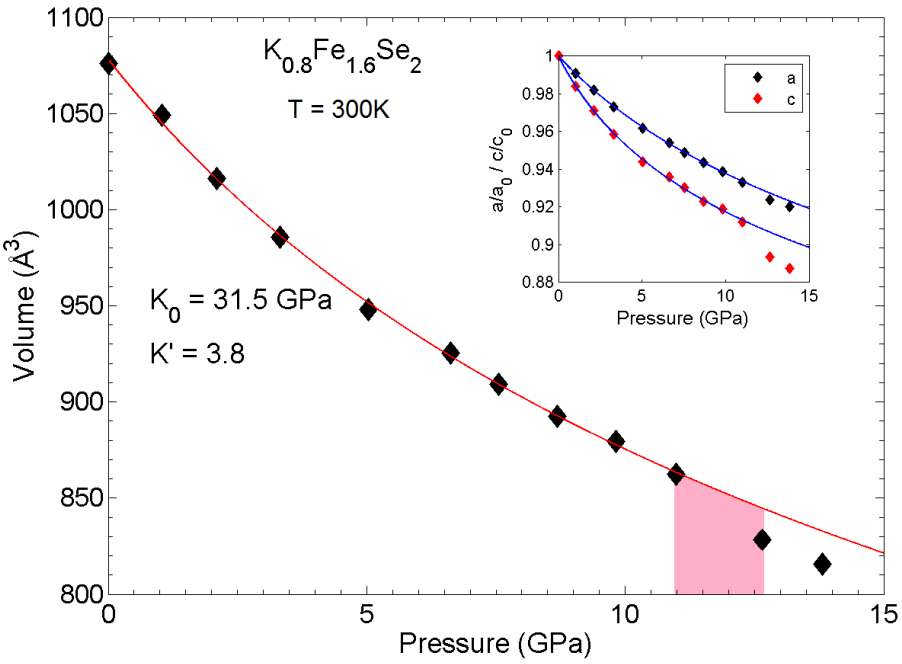

Figure 6.15: Pressure vs. unit cell volume for $K_{0.8}Fe_{1.6}Se_2$ obtained from refinements using the low pressure $I4/m$ structure. The red line indicated a Birch-Murnaghan type equation of state fit to the P-V data, yielding $V_0 = 1078.08 \pm 2.13$Å $K_0 = 31.47 \pm 1.55$ GPa and $K_0' = 3.80 \pm 0.38$. The deviation of the data from the equation of state indicates a structure phase transition occurs in the red shaded area between 11 and 12.6 GPa. *Top inset*: P vs. a and c lattice parameters also fitted with an equation of state.

to the poor quality of the data obtained for sample measured in the cryostat due the background and the use of the samples as the pressure media accurate lattice parameters could not be determined making it difficult see any deviation of the P-V data from the equation of state to give further evidence for the structural transition. Values for the bulk modulus and pressure derivatives as well as the critical pressure for the structural phase transition in the superconducting samples was found to be very similar to that for the insulating sample. This indicates that the composition and more importantly the superconductivity of the $K_xFe_{2-y}Se_2$ does not seem to affect the structural properties of this type of material at room temperature.

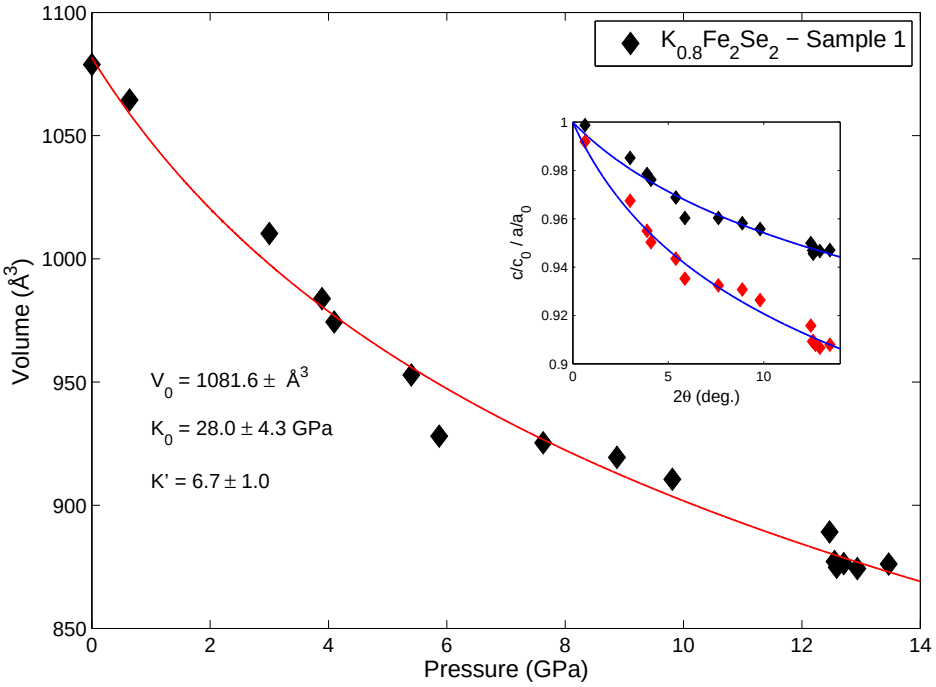

Figure 6.16: Pressure-volume data for sample 1 (superconducting $K_{0.8}Fe_2Se_2$). The red line shows Birch-Murnaghan EoS's fitted to the data. *Inset*: Pressure dependence of the a and c lattice parameters

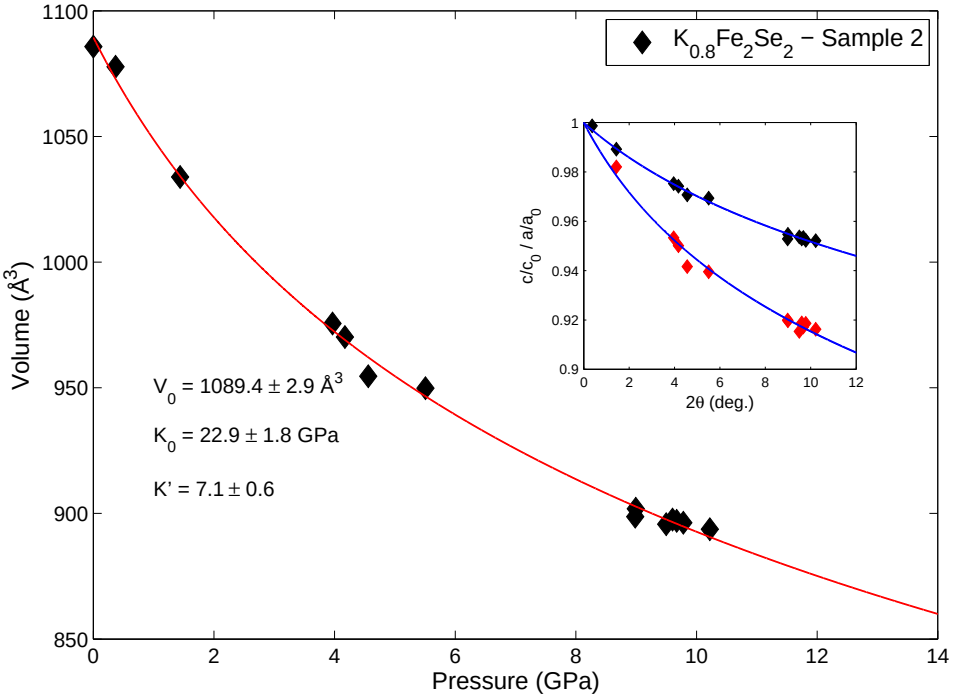

Figure 6.17: Pressure-volume data for sample 2 (superconducting $K_{0.8}Fe_2Se_2$). The red line shows Birch-Murnaghan EoS's fitted to the data. *Inset*: Pressure dependence of the a and c lattice parameters.

All the data collected at both room and low temperature has been used to build up the temperature-pressure phase diagram of $K_xFe_{2-y}Se_2$ in order to see any correlation between the structural phase transition and the location of the two superconducting regions. The phase diagram is shown in figure 6.18. The black and red markers indicate whether the sample is in the *I4/m* or *I4/mmm* structure, with samples 1, 2 and 3 shown as solid squares, diamonds and circles respectively. The phase diagram can roughly be divided into to regions, each with a different structure. The left region of the phase diagram of $K_xFe_2Se_2$ shows points where the (110) peak is still present in the diffraction patterns and the sample is in the zero pressure I4/m structure. In the right region the (110) peak has been suppressed and $K_{0.8}Fe_2Se_2$ takes the *I4/mmm* structure.

As the pressure of the structural transition for both superconducting $K_{0.8}Fe_2Se_2$ and insulating $K_{0.8}Fe_{1.6}Se_2$ is found to be 2-3 GPa higher than that previously measured [67]. It is speculated that the mismatch between the pressures of the structural transitionis due to discrepancies of the pressure measurements. Therefore, to enable a meaningful comparison the measurements here and the previous measurements [67], the pressure axis of the superconducting phase diagram (Figure 6.18 has been rescaled such that the values of the structural transition at room temperature match. The resulting corrected locations of the superconducting phases are shown in Figure 6.18. The suppression of the first superconducting phase is thought to take place at 12 GPa and the second superconducting phase between about 14 and 17 GPa. The first temperature run of Sample 2 indicates a left boundary of the phase transition at low temperature between 13.1 and 13.3 GPa. This shows that the structural transition does not appear to be responsible for the suppression of the first superconducting phase. The temperature run of Sample 1 reaches a highest pressure of about 14.2 GPa. As the sample has very nearly gone through the structural phase transition at this pressure then it appears that at low temperatures the structural phase transition occurs in a pressure range from about 13.2 to 15 GPa. This appears to show that the structural transition appears to play a

key role in the appearance of the second superconducting phase.

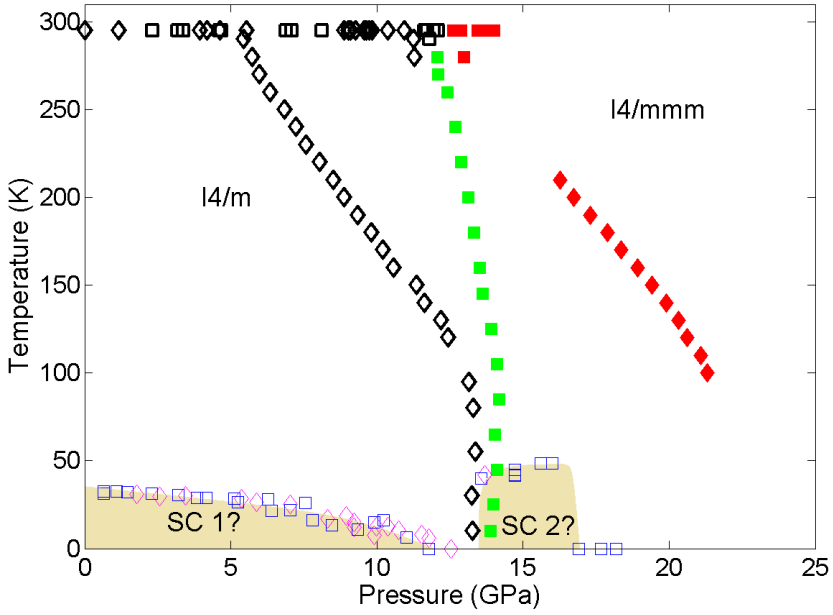

Figure 6.18: Pressure-Temperature structural phase diagram of the of the $K_{0.8}Fe_{2-y}Se_2$ (x = 0, 0.4). Black markers indicate the system in the *I4/m* structure with the Fe vacancy superstructure present and red markers indicate a *I4/mmm* structure. Data taken from samples 1 and 2 are shown as squares and diamonds respectively. The green squares indicate the boundary between the two structural phases. The open blue squares and purple diamonds show the superconducting regions of $K_{0.8}Fe_{1.7}Se_2$ and $K_{0.8}Fe_{1.78}Se_2$ from previous measurements [67], which have been rescaled along the pressure axis such that the suppression of the Fe-vacancy order in this work and previous work [67] occurs at the same pressure at room temperature. The first superconducting phase disappears within the I4/m phase. The second superconducting phase appears to emerge at the same pressure as the structural phase transition.

6.6 Conclusion

Room and low temperature x-ray powder diffraction has been used to determine the pressure-temperature phase diagram of the $K_{0.8}Fe_{2-y}Se_2$ (x = 0, 0.4) system. Measurements at room temperature show the same room temperature critical pressure for the structural transition for both the insulating and the superconducting samples indicating that the precise composition is not important for the location of the transition. This can be explained be the presence of a coxistent $\sqrt{2} \times \sqrt{2}$ superconducting phase with

the majority $\sqrt{5} \times \sqrt{5}$ antiferromagnetic phase [69]. The pressure-temperature structural phase diagram shows that the structural transition at low temperature probably lies at a pressure between 13.2 and 15 GPa. Therefore the first superconducting phase is suppresed independently of the structural transition. The emergence of the second superconducting phase appears to be strongly linked to the structural transition.

Chapter 7

Conclusion

This thesis has invloved two main areas, the first of which was the development of techniques in order to measure both structural and superconducting properties at high pressure and low temperature. The second part was to use these techniques to build up an understanding of the relationship between the structural, magnetic and electronic properties of several systems reported to exhibit unconventional superconductivity. Two families of unconventional superconductor have been focused on both based on transition metals: the Mo-based and Fe-based superconductors.

The first Mo-based superconductor investigated was Mo_3Sb_7 due to it's interesting properites where superconductivity could possibly be found to compete or coexist with an antiferromagnetic ordering. High pressure x-ray powder diffraction measurements confirm that no structural transition into the low temperature tetragonal phase occurs at room temperature. The evolution of T_c was determined beyond that previously reported. Successful measurments were obtained up to 6.2 GPa and found a further increase in T_c to a maximum of 2.62K. The origin of the pressure induced antiferromagnetic state has been determined to be from the tetragonal to cubic transition at low temperatures. The extension of the phase diagram allows an extrapolation of the behaviour of the superconductivity and antiferromagnetism, which suggests a magnetically mediated pairing mechansim.

The second Mo-based superconductor studied was Mo_3Al_2C due to its non-centrosymmetric structure. Several high pressure x-ray powder diffraction experiments were carried out using three different pressure transmitting media; silicon oil, methanol-ethanol and helium. The measurements showed no significant differences in the bulk modulii and pressure derivitives between different pressure media. The P-V data for Mo_3Al_2C give evidence for a structural transition near 15 GPa. No solution to the high pressure phase of Mo_3Al_2C has been found. The evolution of T_c in Mo_3Al_2C was determined and showed a small pressure dependence. Solving the high pressure structure of this material would confirm whether or not the noncentrosymmetric structure remains. If a centrosymmetry switches on during the phase transition it would be interesting to study the effects of this on the superconductivity.

The third and final system measured in this thesis was the iron-chalcogenide $K_xFe_{2-y}Se_2$. X-ray powder diffraction at low temperatures has been used in order to build a complete low temperature-high pressure structural phase diagram with two superconducting domes to identify any correlation between structural transitions and the interesting superconducting properties. Room temperature measurements of both superconducting and insulating samples show the structural transition occurs at the same critical pressure. The critical pressure for the structural transition at low temperature lies in a pressure range between 13.2 and 15 GPa indicating that the structral transition plays a key role in the emergence of the second high pressure superconducting region in $K_{0.8}Fe_2Se_2$ while the pressure induced suppression of the first superconducting phase is unrelated to the structursl transition.

Although the measurements carried out in this thesis have provided important information regarding the structural and superconducting properties, and relationship between them, of the systems studied, there is still room for improvement in the techniques

developed here. The most inconvenient feature in the low temperature x-ray powder diffraction has been the background diffraction from the cryostat components. A future alteration to the cryostat used for these measurements that could be hugely beneficial would be to replace the beryllium windows with optical windows which would eliminate the background, and allow for easier pressure determination through ruby fluorescence. The high pressure magnetic susceptibility technique could be further enhanced to improved the signal-to-noise ratio. This can be achieved by increasing the number of turns in the detection coils the pressure cell sample space, although this would require smaller diameter wire, and therefore increasing the chance of the cell breaking. An improved signal-to-noise ratio may allow magnetic transitions other then the superconducting transition to be observed in the measurements which would be of great use in, for example, the Mo_3Sb_7 measurements in this thesis and many other future measurements.

Bibliography

[1] H. K. Onnes. The Resistance of Pure Mercury at Helium Temperature. *Commun. Phys. Lab. Univ. Leiden*, 12:120.

[2] J. Bardeen, L. N. Cooper, and J. R. Schrieffer. Microscopic Theory of Superconductivity. *Phys. Rev.*, 106:162–164, 1957.

[3] Ronald J. Cohn. Physics today, October 1973.

[4] J.G. Bednorz and K.A. Muller. Possible high T_c superconductivity in the BaLaCuO system. *Zeitschrift fur Physik B Condensed Matter*, 64(2):189–193, 1986.

[5] M. K. Wu, J. R. Ashburn, C. J. Torng, P. H. Hor, R. L. Meng, L. Gao, Z. J. Huang, Y. Q. Wang, and C. W. Chu. Superconductivity at 93K in a new mixed-phase Y-Ba-Cu-O compound system at ambient pressure. *Phys. Rev. Lett.*, 58:908–910, 1987.

[6] Yoichi Kamihara, Hidenori Hiramatsu, Masahiro Hirano, Ryuto Kawamura, Hiroshi Yanagi, Toshio Kamiya, and Hideo Hosono. Iron-based layered superconductor: LaOFeP. *Journal of the American Chemical Society*, 128(31):10012–10013, 2006.

[7] Yoichi Kamihara, Takumi Watanabe, Masahiro Hirano, and Hideo Hosono. Iron-based layered superconductor $La[O_{1-x}F_x]FeAs$ (x = 0.050.12) with T_c = 26K. *Journal of the American Chemical Society*, 130(11):3296–3297, 2008.

[8] D. N. Basov and A. V. Chubukov. Manifesto for a higher T_c. *Nature Physics*, 7:272–276, 2011.

[9] G. J. Sizoo and H. K. Onnes. *Commun. Phys. Lab. Univ. Leiden*, No. 180b, 1925.

[10] B.M. Andersson, B. Sundqvist, J. Niska, B. Loberg, and K. Easterling. Electrical transport properties of dense bulk $YBa_2Cu_4O_8$ produced by hot isostatic pressing. *Physica C: Superconductivity*, 170(56):521 – 531, 1990.

[11] E. Bauer, G. Rogl, Xing-Qiu Chen, R. T. Khan, H. Michor, G. Hilscher, E. Royanian, K. Kumagai, D. Z. Li, Y. Y. Li, R. Podloucky, and P. Rogl. Unconventional superconducting phase in the weakly correlated noncentrosymmetric Mo_3Al_2C compound. *Phys. Rev. B*, 82:064511, 2010.

[12] l. et. al. Sun. Re-emerging superconductivity at 48K in iron chalcogenides. *Nature*, 483:67–69, 2012.

[13] Angel R.J. High-pressure structural phase transitions. *Reviews in Mineralogy and Geophysics*, 39:85–104, 2000.

[14] F. D. Murnaghan. The compressibility of media under extreme pressures. *Proceedings of the National Academy of Sciences*, 30(9):244–247, 1944.

[15] I. Jackson and H. Niesler. *The elasticity of periclase to 3GPa and some geophysical implications. In: High-Pressure research in Geophysics.* Center for Academic Publications, Tokyo, 1982.

[16] J. Freund and R. Ingalls. Inverted isothermal equations of state and determination of B_0, B'_0 and B_0. *Journal of Physics and Chemistry of Solids*, 50(3):263 – 268, 1989.

[17] S. L. Sondhi, S. M. Girvin, J. P. Carini, and D. Shahar. Continuous quantum phase transitions. *Rev. Mod. Phys.*, 69:315–333, 1997.

[18] G.G. Lonzarich. *Electron: A Centenary Volume*. Cambridge University Press, 1997.

[19] L. H. Greene. High temperature superconductors: Playgrounds for broken symmetries. *AIP Conference Proceedings*, 795(1):70–82, 2005.

[20] Leonid Dubrovinsky *et al*. *Nature Communications*, 3:1163, 2012.

[21] M. Eremets. *High Pressure Experimental Methods*. Oxford University Press.

[22] G. J. Piermarini, S. Block, and J.D. Barnett. Hydrostatic limits in liquids and solids to 100 kbar. *Journal of Applied Physics*, 44(12), 1973.

[23] G. J. Piermarini, S. Block, J. D. Barnett, and Forman R. A. Calibration of the pressure dependence of the R1 ruby fluorescence line to 195 kbar. *Journal of Applied Physics*, 46(6):2774–2780, 1975.

[24] K. Syassen. Ruby under pressure. *High Pressure Research*, 28(2):75–126, 2008.

[25] G. J. Piermarini, S. Block, and J.D. Barnett. Hydrostatic limits in liquids and solids to 100 kbar. *Journal of Applied Physics*, 44(12):5377–5382, 1973.

[26] Piermarini G.J. Block S. Fujishiro, I. and R.G. Munro. Viscocities and glass transition pressures in the methanol-ethanol-water system. *High pressure in research and industry, Proceedings of the 8th AIRAPT Conference, Uppsala*, Vol. II:pp. 608–11, 1982.

[27] S Klotz, J-C Chervin, P Munsch, and G Le Marchand. Hydrostatic limits of 11 pressure transmitting media. *Journal of Physics D: Applied Physics*, 42(7):075413, 2009.

[28] J. Dean Barnett and Charles D. Bosco. Viscosity measurements on liquids to pressures of 60 kbar. *Journal of Applied Physics*, 40(8):3144–3150, 1969.

[29] H. K. Mao. Static compression of simple molecular systems in the megabar range. *Simple molecular systems at very high density*, pages pp.221–36, 1989. Plenum Press, New York.

[30] P.M. Bell and H.K. Mao. Degree of hydrostatiscity in He, Ne and Ar pressure transmitting media. *Carnegie Institute Washington Yearbook*, 80:404–6, 1981.

[31] K. Asaumi and A. L. Ruoff. Nature of the state of stress produced by xenon and some alkali iodides when used as pressure media. *Phys. Rev. B*, 33:5633–5636, 1986.

[32] Kenneth A. Goettel, Jon H. Eggert, Isaac F. Silvera, and William C. Moss. Optical evidence for the metallization of xenon at 132(5) Gpa. *Phys. Rev. Lett.*, 62:665–668, 1989.

[33] J.M. Besson and J.P. Pinceaux. Melting of helium at room temperature and high pressure. *Science*, 206:1073–5.

[34] P. W. Bridgman. The resistance of 72 elements, alloys and compounds to 100,000 kg/cm. *Proceedings of the American Academy of Arts and Sciences*, 81(4):pp. 165, 167–251, 1952.

[35] A.-S. Rüetschi and D. Jaccard. Adaptation of the Bridgman anvil cell to liquid pressure mediums. *Review of Scientific Instruments*, 78(12):123901, 2007.

[36] A Eiling and J S Schilling. Pressure and temperature dependence of electrical resistivity of Pb and Sn from 1-300K and 0-10 GPa - use as continuous resistive pressure monitor accurate over wide temperature range; superconductivity under pressure in Pb, Sn and In. *Journal of Physics F: Metal Physics*, 11(3):623, 1981.

[37] T.F. Smith, C.W. Chu, and M.B. Maple. Superconducting manometers for high pressure measurement at low temperature. *Cryogenics*, 9(1):53 – 56, 1969.

[38] B Bireckoven and J Wittig. A diamond anvil cell for the investigation of superconductivity under pressures of up to 50 GPa: Pb as a low temperature manometer. *Journal of Physics E: Scientific Instruments*, 21(9):841, 1988.

[39] David Erskine, Peter Y. Yu, and Gerard Martinez. Technique for high-pressure electrical conductivity measurement in diamond anvil cells at cryogenic temperatures. *Review of Scientific Instruments*, 58(3):406–411, 1987.

[40] http://www.diamond.ac.uk/home/about/how-diamond-works.html.

[41] http://www.diamond.ac.uk/beamlines/engineering-and-environment/i15.html.

[42] A. P. Hammersley, S. O. Svensson, M. Hanfland, A. N. Fitch, and D. Hausermann. Two-dimensional detector software: From real detector to idealised image or two-theta scan. *High Pressure Research*, 14(4-6):235–248, 1996.

[43] Christopher Hammond. *The Basics of Crystallography and Diffraction*. Oxford University Press, 2nd edition, 2001.

[44] Adam. L. Woodcraft. An Introduction to Cryogenics.

[45] Quantum Design. *PPMS Hardware Manual*. Quantum Design, 2000.

[46] Quantum Design. *PPMS AC Transport option manual*. Quantum Design, 2000.

[47] Quantum Design. *PPMS ACMS option manual*. Quantum Design, 2000.

[48] D. Jaccard and K. Sengupta. Multiprobe experiments under high pressure: Resistivity, magnetic susceptibility, heat capacity, and thermopower measurements around 5 GPa. *Review of Scientific Instruments*, 81(4):043908, 2010.

[49] Patricia Lebre Alireza and Stephen R. Julian. Susceptibility measurements at high pressures using a microcoil system in an anvil cell. *Review of Scientific Instruments*, 74(11):4728–4731, 2003.

[50] C. W. Harrison. *High Pressure Study of Magnetic Quantum Phase Transitions in Transition Metal Materials*. PhD thesis, Royal Holloway and Beford New College, University of London, 2012.

[51] V. H. Tran and Z. Bukowski. Synthesis and characterisation of the superconductor Mo_3Sb_3. *Acta. Phys. Pol. A*, 114:67, 2008.

[52] Yano S. Muranaka T. Okabe, H. and J. Akimtsu. Magnetic and structural transitions in Mo_3Sb_7. *Journal of Physics: Conference Series*, 150:052196, 2009.

[53] J.-Q. Yan, M. A. McGuire, A. F. May, H. Cao, A. D. Christianson, D. G. Mandrus, and B. C. Sales. Flux growth and physical properties of Mo_3Sb_7 single crystals. *Phys. Rev. B*, 87:104515, 2013.

[54] V H Tran, R T Khan, P Winiewski, and E Bauer. Pressure studies on the superconductor Mo_3Sb_7. *Journal of Physics: Conference Series*, 273(1):012088, 2011.

[55] C. Candolfi, B. Lenoir, A. Dauscher, C. Bellouard, J. Hejtmánek, E. Šantavá, and J. Tobola. Spin fluctuations and superconductivity in Mo_3Sb_7. *Phys. Rev. Lett.*, 99:037006, 2007.

[56] Tetsuya Takeuchi, Masato Shiimoto, Hisanori Kohara, Takashi Yasuda, Shin Hashimoto, Rikio Settai, and Yoshichika nuki. Magnetism and superconductivity in $CePt_3Si$ under pressure. *Journal of the Physical Society of Japan*, 75(Suppl):170–173, 2006.

[57] A. B. Karki, Y. M. Xiong, I. Vekhter, D. Browne, P. W. Adams, D. P. Young, K. R. Thomas, Julia Y. Chan, H. Kim, and R. Prozorov. Structural and physical properties of the noncentrosymmetric superconductor Mo_3Al_2C. *Phys. Rev. B*, 82:064512, 2010.

[58] Fong-Chi Hsu, Jiu-Yong Luo, Kuo-Wei Yeh, Ta-Kun Chen, Tzu-Wen Huang, Phillip M. Wu, Yong-Chi Lee, Yi-Lin Huang, Yan-Yi Chu, Der-Chung Yan, and

Maw-Kuen Wu. Superconductivity in the PbO-type structure α-FeSe. *Proceedings of the National Academy of Sciences*, 105(38):14262–14264, 2008.

[59] S et al. Medvedev. *Nat. Mater*, 8:630.

[60] Jiangang Guo, Shifeng Jin, Gang Wang, Shunchong Wang, Kaixing Zhu, Tingting Zhou, Meng He, and Xiaolong Chen. Superconductivity in the iron selenide $K_xFe_2Se_2$ $0 \leq x \leq 1.0$. *Phys. Rev. B*, 82:180520, 2010.

[61] Hang-Dong Wang, Chi-Heng Dong, Zu-Juan Li, Qian-Hui Mao, Sha-Sha Zhu, Chun-Mu Feng, H. Q. Yuan, and Ming-Hu Fang. Superconductivity at 32K and anisotropy in $Tl_{0.58}Rb_{0.42}Fe_{1.72}Se_2$ crystals. *EPL (Europhysics Letters)*, 93(4):47004, 2011.

[62] T. P. Ying *et al. Sci. Rep.*, 2:426, 2012.

[63] Yan Y.J. *et al.* Electronic and magnetic phase diagram in $K_xFe_{(2-y)}Se_2$ superconductors. *Sci. Rep.*, 2:212, 2012.

[64] D. Louca *et al.* The hybrid lattice of $K_xFe_{2-y}Se_2$: where superconductivity and magnetism coexist. *Sci. Rep.*, 3:2047, 2013.

[65] Peiwen Gao, Rong Yu, Liling Sun, Hangdong Wang, Zhen Wang, Qi Wu, Minghu Fang, Genfu Chen, Jing Guo, Chao Zhang, Dachun Gu, Huanfang Tian, Jianqi Li, Jing Liu, Yanchun Li, Xiaodong Li, Sheng Jiang, Ke Yang, Aiguo Li, Qimiao Si, and Zhongxian Zhao. Role of the 245 phase in alkaline iron selenide superconductors revealed by high-pressure studies. *Phys. Rev. B*, 89:094514, 2014.

[66] Wei Li, Hao Ding, Zhi Li, Peng Deng, Kai Chang, Ke He, Shuaihua Ji, Lili Wang, Xucun Ma, Jiang-Ping Hu, Xi Chen, and Qi-Kun Xue. KFe_2Se_2 is the parent compound of K-doped iron selenide superconductors. *Phys. Rev. Lett.*, 109:057003, 2012.

[67] Jing Guo, Xiao-Jia Chen, Jianhui Dai, Chao Zhang, Jiangang Guo, Xiaolong Chen, Qi Wu, Dachun Gu, Peiwen Gao, Lihong Yang, Ke Yang, Xi Dai, Ho-kwang Mao, Liling Sun, and Zhongxian Zhao. Pressure-driven quantum criticality in iron-selenide superconductors. *Phys. Rev. Lett.*, 108:197001, 2012.

[68] Z. Wang, Y. J. Song, H. L. Shi, Z. W. Wang, Z. Chen, H. F. Tian, G. F. Chen, J. G. Guo, H. X. Yang, and J. Q. Li. Microstructure and ordering of iron vacancies in the superconductor system $K_yFe_xSe_2$ as seen via transmission electron microscopy. *Phys. Rev. B*, 83:140505, 2011.

[69] D. G. Porter, E. Cemal, D. J. Voneshen, K. Refson, M. J. Gutmann, A. Bombardi, A. T. Boothroyd, A. Krzton-Maziopa, E. Pomjakushina, K. Conder, and J. P. Goff. Two-dimensional cs-vacancy superstructure in iron-based superconductor $Cs_{0.8}Fe_{1.6}Se_2$. *Phys. Rev. B*, 91:144114, 2015.